5-2018

Quasi-continuum Non-local Plate and Shell Models of Carbon-Based 2D Nanomaterials

Jixuan Gong
Clemson University, jixuang@clemson.edu

QUASI-CONTINUUM NON-LOCAL PLATE AND SHELL MODELS OF CARBON-BASED 2D NANOMATERIALS

A Dissertation
Presented to
the Graduate School of
Clemson University

In Partial Fulfillment
of the Requirements for the Degree
Doctor of Philosophy
Mechanical Engineering

---

by
Jixuan Gong
May 2018

Accepted by:
Dr. Gang Li, Committee Chair
Dr. Lonny Thompson
Dr. Huijuan Zhao
Dr. Paul Joseph

Abstract

Non-local plate and shell models have attracted much interest in the area of graphene and carbon nanotube simulations. This work explores further into this area and aims to provide more accurate and reliable non-local modeling methods to graphene and carbon nanotubes.

At first, a semi-analytical model for determining the equilibrium configuration of single wall carbon nanotubes is presented. By taking advantage of the symmetry characteristics, a carbon nanotube structure is represented by five independent variables. A line search optimization procedure is employed to determine the equilibrium values of these variables by minimizing the potential energy. With the equilibrium configuration obtained, the semi-analytical model enables a straightforward calculation of the radial breathing mode frequency of carbon nanotubes. The radius and radial breathing mode frequency results obtained from the semi-analytical approach are compared with those from molecular dynamics and ab initio calculations. The results demonstrate that the semi-analytical approach offers an efficient and accurate way to determine those properties.

Next, we investigate several issues in the local and non-local plate models of single layer graphene sheets. The issues include the ambiguity of the plate thickness in the moment-curvature relation, the definition of clamped boundary condition at graphene edges, and the value of the non-local parameter. For error analysis, the results obtained from a REBO potential based atomic lattice mechanics model are used as reference results. Er-

rors of the plate models are analyzed and remedies are proposed within the framework of the non-local plate model. Numerical results of static and modal analysis of graphene are presented to demonstrate the effectiveness of the remedies.

In the last part of this work, a non-local finite element shell model is established for single-walled carbon nanotubes. Based on the accurately relaxed radius, bond lengths and angles obtained from the semi-analytical model, it is possible to calculate more accurate elastic constants directly from the interatomic potentials. Then through the combination of the classical first order shell theory, the non-local elasticity, and the potential-based elastic properties, a more accurate shell representation of single wall carbon nanotubes is established. The improvement in accuracy is demonstrated by comparing the spectral frequency analysis and dispersion relation results with those obtained from lattice mechanics and molecular dynamics simulations, respectively.

Dedication

This dissertation is dedicated to

my beloved son and wife,

my parents,

and other families and friends who have kindly supported me during these years.

Acknowledgments

I want to say special thanks to my advisor, Dr. Gang Li. He is a very responsible, professional and warmhearted professor. He has spent a lot of time on guiding my research and revising my papers, and he was very supportive when I met frustrations. Dr. Li also offered me financial support during my study. I'm glad that I have been working on my PhD under his supervision. I also want to thank my co-advisor, Dr. Lonny Thompson who offered me this interesting research topic, and he provided me with many important suggestions on FEA and the non-local elasticity. Besides, I want to thank my TA supervisor, Dr. Todd Schweisinger, who has helped me a lot during my TA working. And I want to thank my committee members as well, who offered me a lot of valuable advises during my proposal defense.

In the end, I want to thank my parents and my family for their love and support. Without them I cannot have overcome all these challenges during my 6 years of study.

Table of Contents

List of Tables

List of Figures

Chapter 1

Introduction

Graphene, carbon nanotubes (CNTs) and fullerene are a group of carbon allotropes with two dimensional honeycomb-like structures as shown in Fig. (1.1). Graphene is a single-layer of graphite in which carbon atoms are sp^2 hybridized. Similarly, CNTs are also made of one or several layers of sp^2 carbon atoms, but in seamless cylindrical shapes [16] which is often seen as results of graphene rolling. However, CNTs are manufactured much earlier than graphene. In 1991, Iijima successfully synthesized carbon nanotubes using arc-discharge evaporation method [34]. On the other hand, it was believed that mono-layer atom membranes are thermally unstable and may not be produced as stand-alone structures. Until 2004, Novoselov exfoliated mono-layer graphene from graphite for the first time [52] and discovered its unusual ballistic in-plane electronic transport. Both graphene and carbon nanotubes exhibit extraordinary thermal, electrical and mechanical properties and they have been the focus of research interest for more than two decades.

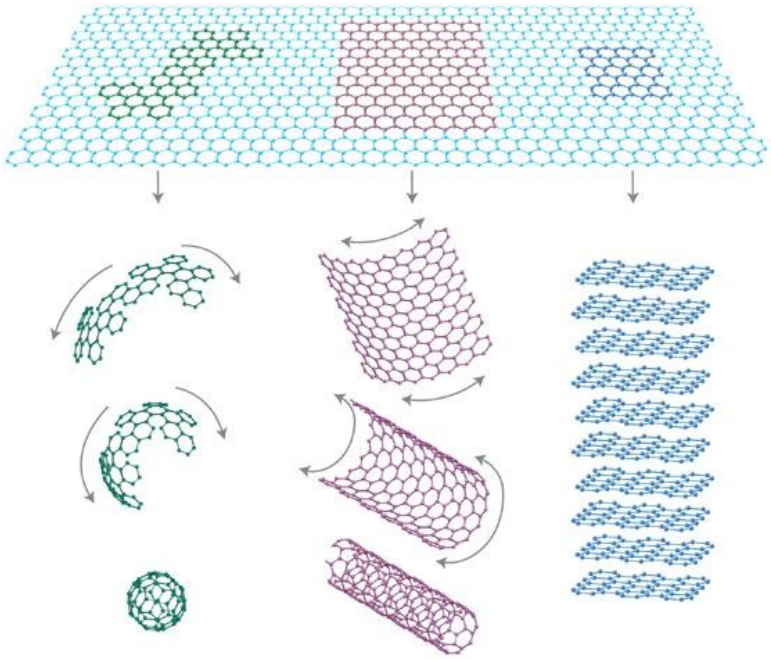

Figure 1.1: Illustration of graphene-like materials [26].

1.1 Experiments of mechanics of graphene and carbon nanotubes

In many applications of graphene-like materials, it is important to know their corresponding mechanical behaviors. The most straightforward method is through experiments. Many experiments have been done on graphene [24, 65, 81] and CNTs [80, 21, 60]. Experiments at nano-scale require special equipments, such as atomic force microscope (AFM) and transmission electron microscopy (TEM). AFM has very high resolution and can use its probe to apply measurable forces to samples. For example, Wong [91] and Yu [97, 96] tested the behaviors of single and multi-wall carbon nanotubes under compression or axial tensile loading through an AFM, as shown in Fig. (1.2). Also using AFM, Frank [23] measured the bending rigidity of several (less than 5) layers of graphene in 2007. No more than a year later, Lee and his colleagues measured the bending properties of suspended

mono-layer graphene membranes, which is shown in Fig. (1.3) [40].

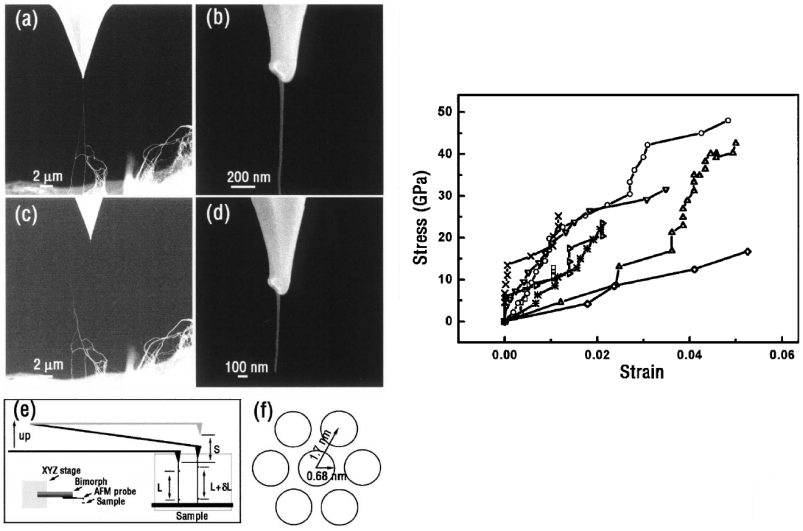

Figure 1.2: Tensile test of single wall carbon nanotubes with AFM [96]

Another tool that is widely used is TEM. In TEM, an electron beam passes through a given sample after accelerated with an electric field. A recording media is placed after the sample material which will show the electron density distribution. The structure of the material can be obtained from this distribution. In 1996 Treacy et. al measured the Young's moduli of multi-walled CNTs with different sizes [80]. He used TEM to observe free-stand CNTs shown in Fig. (1.4). From the image he found that the free tips of these tubes were blur due to thermal vibrations. He calculated the averaged vibration energy from the temperature of the system, and obtained Young's moduli of CNTs with it. It was the first time that the Young's moduli of CNTs were found to be in the order of 1 TPa. More recently, Huang and his team also observed graphene grains especially the grain boundaries using TEM [30]. Their observation is shown in Fig. (1.5).

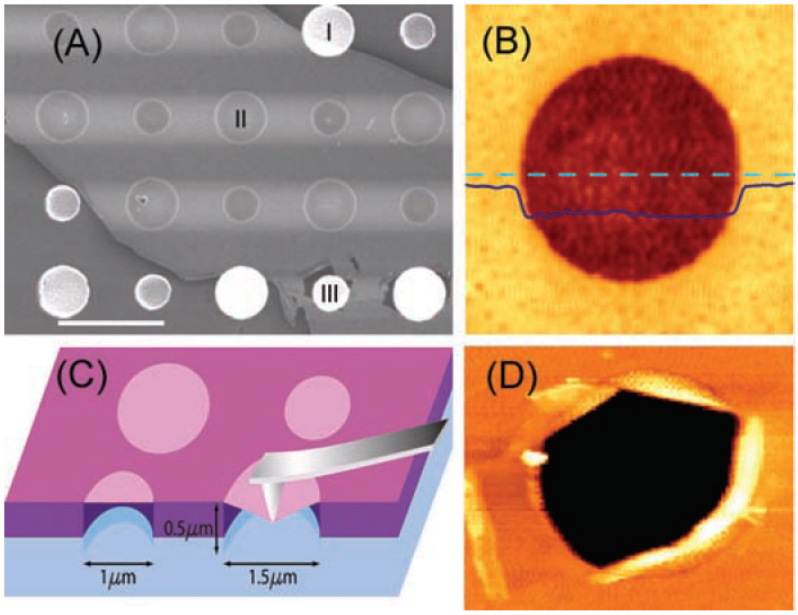

Figure 1.3: Images of suspended graphene memberanes. (A) Scanning electron micrograph of large graphene flake spanning an array of circular holes 1 μm and 1.5 μm in diameter. Area I shows a hole partially covered by graphene, area II is fully covered, and area III is fractured from indentation. (B) Nonscontact mode AFM image of membrane, 1.5 μm in diameter. The solid blue line is a height profile along the dashed line. The step height at the edge of the membrane is about 2.5 nm. (C) Schematic of nano-indentation on suspended graphene membrane. (D) Image of a fractured membrane [40].

1.2 Atomic level simulations on graphene and carbon nanotubes

While being direct and intuitive, performing experimental measurements on nanomaterials is typically difficult and expensive, especially when extra constraints and conditions, such as specific initial strain/stress, irregular shapes, defects and chiralities, are required. As an alternative approach, numerical simulations are much more cost effective and insightful. To obtain reliable results efficiently, it is crucial to develop proper computational models. Based on spacial scale, computational models can be broadly categorized into first principle calculations, atomistic/molecular simulations and continuum simulations. More

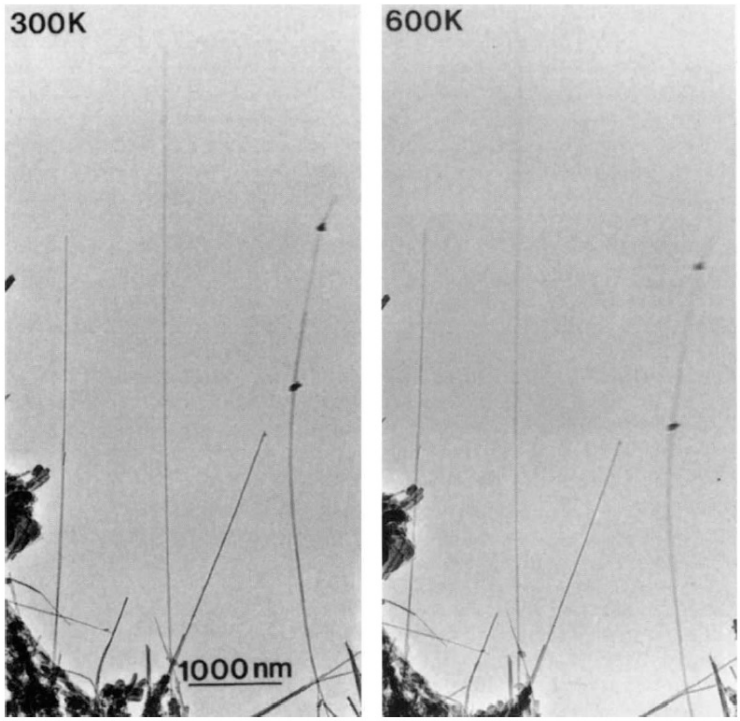

Figure 1.4: TEM image of free stand CNTs[80]

recently, to achieve the goal of accurately capturing the atomistic physics and yet retaining the efficiency of continuum models, multiscale modeling and simulation techniques which connect and integrate the atomistic and continuum theories have attracted considerable research interest [77].

First principle (also known as ab initio) calculations evaluate forces and energies by considering electronic structures with Schrödinger's equation. An outstanding example is the density function theory (DFT). DFT is an important tool for simulating graphene and CNT growth [55], as it is accurate. For an instance, using DFT, Gao and his colleagues investigated the chemical vapor deposition synthetics of graphene on metal substrates [25]. In mechanical area, the ab initio approach has been used to compute graphene and CNT's elastic properties such as Young's modulus and strength [20, 50, 54]. In 2000, Van Lier et al calculated the Young's moduli and the Poisson's ratio of graphene and CNTs with

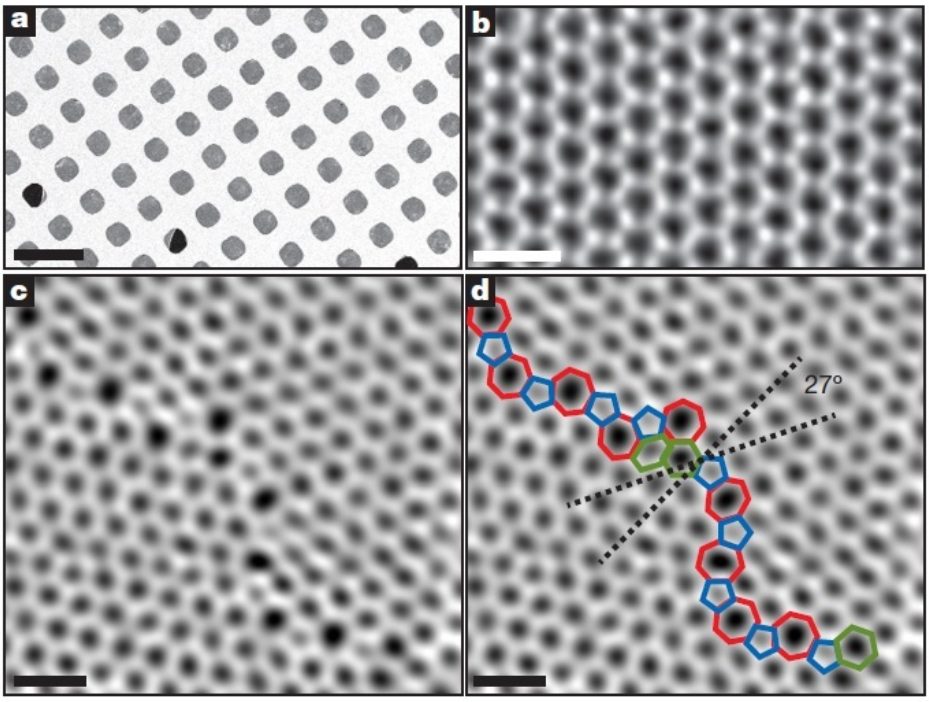

Figure 1.5: Atomic-resolution ADF-STEM images of graphene crystals [30]

different chiralities [83]. In his work, graphene and CNTs were simulated at Hartree-Fock 6-31G level of energy through multiplicative integral approach (MIA). Graphene and CNTs were subjected to single axis stretching, and the Young's moduli and Poisson's ratios are obtained from the ratio of force/relative elongation and the relative radii change/relative elongation. His work confirmed that the Young's moduli of CNTs and graphene are around 1 TPa.

A simpler computational model in atomistic/molecular level is molecular dynamics (MD) [75, 9, 84, 36, 57, 42]. MD simulations use potential functions instead of solving Schrödinger's equation to approximate the interactions among atoms. The movement of atoms is predicted by simply applying the Newtom's Second Law $F = ma$. There are many popular potentials developed for solid materials, including Morse [51], Tersoff [78], 1st and 2nd generation Brenner (REBO) [10, 12], etc. Using MD simulations, Belyschko [9] has

calculated the fracture of CNTs using the modified Morse potential. During his simulation different CNTs were stretched until cracked. The stress-strain relations were recorded, and the crack evolution was also reported. And similar to it, a stretching test on graphene was also performed in MD by Jiang et al [36]. They used 2nd generation Brenner potential, and calculated the Young's modulus of graphene. Li investigated the deformation and thermal properties of hydrogen-doped graphene[41, 42]. Very recently, through MD simulations, Li et al discovered heat flux induced coherent vibration of h-shaped graphene structure [44].

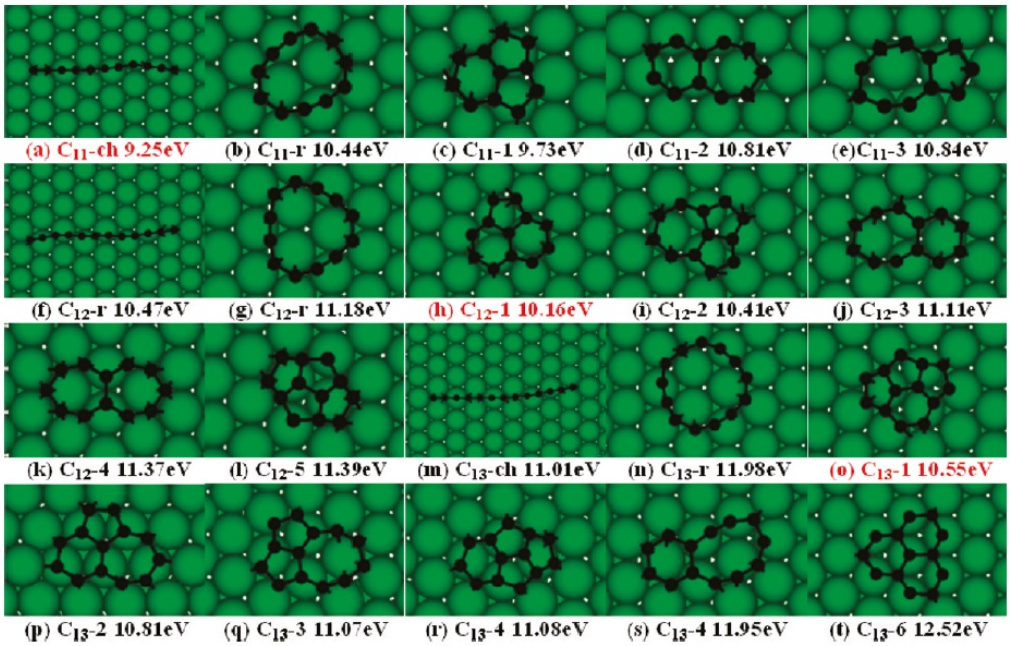

Figure 1.6: Illustration on the formulation progress and structures of several low energy isomers on a Ni substrate [25]

1.3 Continuum modeling of graphene-like materials

On a higher level abstraction, continuum models treat graphene-like materials as a continuum. Different types of continuum models have been proposed in the literature. Some researchers considered graphene-like materials as structural trusses or frames [53,

Type	N	E	F	R	Y	ν
Closed(9,0) D_3	78	−2953.496	8.772	3.61	1.14	-0.026
	150	−5680.295	8.682	3.56	1.14	0.115
Closed(9,0) D_3h	78	−2953.479	9.063	3.61	1.18	-0.032
	150	−5680.311	8.678	3.56	1.14	0.113
Closed(8,2)	80	−3029.238	7.380	3.69	0.94	0.047
	152	−5755.925	8.008	3.65	1.03	0.099
Closed(5,5)	80	−3029.237	5.397	3.53	0.72	0.049
	150	−5680.288	7.750	3.44	1.06	0.125
Graphene(5,5)	134	−4031.136	8.047	n/a	1.11	n/a

Figure 1.7: Simulation results on CNTs and graphene [83]. The Young's moduli (Y) and Poisson's ratio (ν) are given by the last tow columns

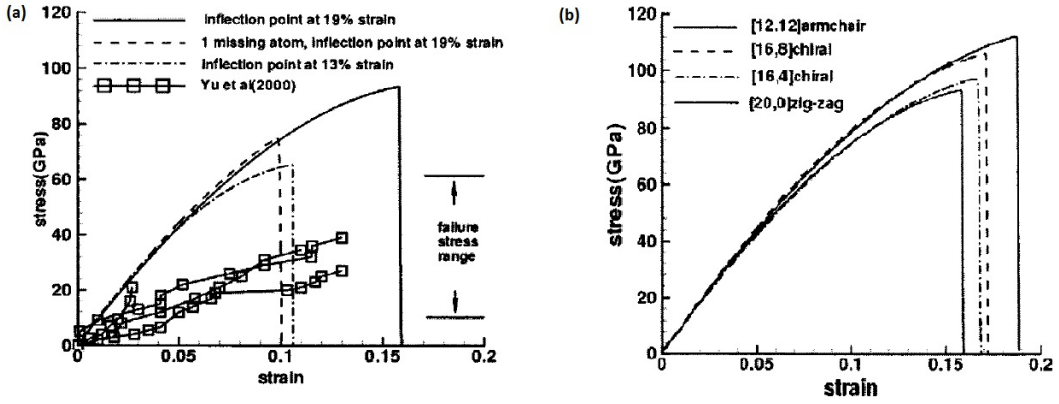

Figure 1.8: Stress-strain curves of CNT failure. (a) are from zigzag tube results compared with experiments. (b) shows results from CNTs with different chiralities [9]

71, 48, 73], in which the honey-comb atomic structure is modeled as rods or beams and each atom is considered as a joint. While the classical beam theories can be conveniently used to model the interaction between the carbon atoms, the complexity of the system is still at the same level with MD as the movement of every atom is calculated. Another continuum level approach is to model the 2-D materials as thin plates or shells. Since each plate or shell element can represent a large number of atoms, the detailed atomic structures are homogenized into the material and structural properties of the plate and shell elements.

This approach is computationally much more efficient than other methods.

1.3.1 The thickness of single-layer carbon atom lattice

Although shell and plate models are advantageous in terms of efficiency, there are two major issues. First, the classical plate and shell models use plate thickness to define the cross-sectional properties. Nevertheless, the thickness is not well defined for graphene and single-walled carbon nanotube (SWCNT) as there is only a single layer of carbon atoms. In many studies, the thickness of a single carbon atom layer was simply set as the spacing between two layers of graphene in graphite, approximately 0.34 nm. But soon it is found that this thickness cannot accomodate both in-plane stiffness and out-of-plane bending stiffness. To avoid this problem, there are many studies using a fitted number determined by matching the plate behavior with experimental data or previously verified results. The fitted thickness is usually much smaller than 0.34 nm. For this reason, a wide range of thickness values of graphene were reported in the literature [31].

To address this issue, the cross-sectional structural properties of graphene were directly calculated by using atomistic description of the interaction of the atoms. This way, explicit value of the thickness of graphene is not required. For example, Huang [31] and Wu [92] have implemented atomic potential-based analytical expressions of stiffness matrices for both flat and curved mono-layer graphene-like materials.

1.3.1.1 Geometry-dependent stiffness and the non-local elasticity

The second issue lies in the accuracy of the plate/shell theory based models when describing the single layer atomic lattice. The error mainly comes from two aspects: constitutive relations and geometries. It has been reported that graphene has unusual moment-curvature relations compared to traditional shell models [31]. Moreover, the constitutive

relations are typically structure dependent [82, 43, 14, 87, 86, 31]. It is also known that, as the shell models ignore the detailed atomic structures of graphene, shell models are inaccurate when the characteristic size of deformation is comparable to the spacing between carbon atoms. Examples of such cases are vibration of graphene lattice with small wave length, or considering deformations near the boundary. Peng [58] and Wu [92] have discussed about the relation between the order of error and the size of deformation patterns.

To consider the effect of discrete atomic structures, several authors have extended plate and shell models of graphene and CNT by including the non-local elasticity. In 1983, Eringen [18] derived a simplified non-local elasticity theory of lattice wave problems. In this theory the stress is not only related with the strain, but also with a scaled Laplacian of strain with a scaling coefficient $e_0 a$. Recently the non-local model has been revisited and applied to 2D nano-materials, such as graphene and CNTs. Lu [47] and Pradhan [64] implemented non-local plate models for nano-plates. Wang [89] derived a non-local shell model for CNTs in cylindrical coordinates, and Hu [29] further compared that with MD simulation results. After that, Ansari [3] applied non-local Mindlin plate model on single-layer graphene sheets (SLGS). Arash [5] developed a non-local finite element model for SLGS based on Kirchhoff plate theory. Mohammadi [49] derived analytical solutions for circular SLGS. Each of these studies shows improvement of the performance by using non-local shell models for graphene and CNTs.

For the interatomic potential-based shell modeling, as mentioned above, there are significant errors when the characteristic length of deformation is comparable to atomic spacing [58, 92]. On the contrary, the non-local elasticity aims to address the issue of lattice spacing. However, to the best knowledge of the author, so far all non-local shell models of graphene and CNTs are still using traditional constitutive relations. Furthermore, there is no general consensus on how to determine the scale coefficient $e_0 a$ in the non-local model. From the original theory, Eringen [18] defined a as the characteristic length of

the lattice, and deduced $e_0 \approx 0.39$. But most of the recent non-local shell based models employed quite different values [2, 17, 90]. Meanwhile, several further observations can be made from the results shown in the literature: (1) for a given problem different $e_0 a$s give different results [49]; (2) the best fitting values of $e_0 a$ are different for graphene and CNTs with different sizes, chiralities, boundary conditions or shapes [3, 29, 6, 74], as shown in Figs. 4 and 5; and (3) even for the same graphene sheet or CNT, different $e_0 a$s should be used for different vibrational modes [29, 6, 45].

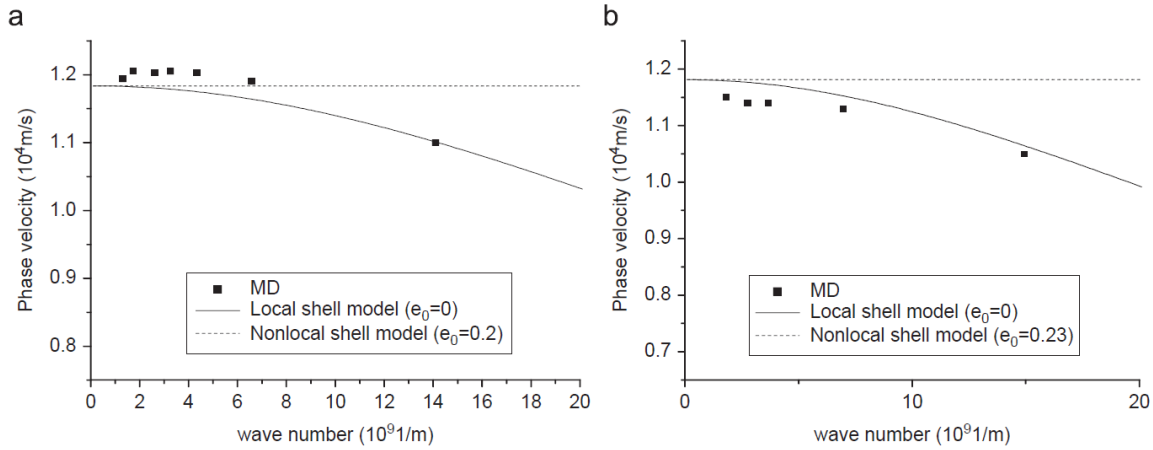

Figure 1.9: Dispersion relation of torsional wave in (a) (10,10) and (b) (15,15) SWCNT [29]

Molecular dynamics (THz)	Nonlocal continuum model (THz) ($\mu = 1.41$)	Side Length of Square SLGS (nm)
0.0587725	0.0584221	10
0.0273881	0.0282888	15
0.0157524	0.0164593	20
0.0099840	0.0107085	25
0.0070655	0.0075049	30
0.0052982	0.0055447	35
0.0040985	0.0042608	40
0.0032609	0.0033751	45
0.0026194	0.0027388	50

Figure 1.10: Fundamental frequencies of squared single layer graphene sheet with different edge length. Here $\mu = e_0 a$ [3].

1.4 Dissertation outline

In this dissertation, we aim to solve these problem by developing an interatomic potential based non-local plate and shell models for graphene and CNT, respectively. The proposed plate and shell models adopt the quasicontinuum multiscale modeling strategy that solves the continuum equations with constitutive laws or material properties extracted from the underlying atomistic description [77, 98]. We also investigated the performance of the plate and shell models under different applications. This is achieved by following steps:

1. In Chapter 2, we begin with a literature review on the current status of plate and shell modeling of graphene and CNT. That includes a brief introduction to the classical plate and shell model, a review on researches about the constitutive relations of graphene and CNT, and a review on the development of non-local elasticity and its application on graphen and CNT. Finally, several research questions are listed, which will be answered at the end of this dissertation.

2. In Chapter 3, a semi-analytical model for obtaining the equilibrium geometry of SWCNT is developed. This model employs two bond lengths along with three bond angles as independent variables, which enables analytical differentiation of interatomic potential functions. Then the equilibrium geometry of CNTs is obtained by using an energy minimization procedure, which is performed by conjugate gradient optimization method. This model can also be applied to calculate RBM frequencies for various CNTs.

3. In Chapter 4, a finite element formulation of potential-oriented non-local Kirchoff plate model of SLGS is derived. For error estimation, an atomic lattice model of SLGS based on the 2nd generation REBO potential is also implemented and used

as reference for all calculations and results. We also propose a simple correction of the boundary location and show that the error is largely reduced in all cases. Next, we investigate the choice of e_0a values in the modal analysis of SLGS. The modal frequency spectrum of the first 50 modes are calculated using the local and non-local plate model with a set of different e_0as. The effect of non-local parameter is studied and the effectiveness of the non-local model is discussed.

4. In Chapter 5, a finite element formulation of potential-oriented non-local shell model of SWCNT is developed. With accurate geometry of SWCNT obtained from the method stated in Chapter 2, the in-plane stiffness matrix and the bending stiffness matrix of SWCNTs are analytically calculated. Similar to Chapter 4, the natural frequencies of different SWCNTs are calculated, and corresponding atomic lattice models are used as reference. Effects of boundary corrections and non-local coefficients are evaluated. Finally, the non-local shell model is used to simulate the wave propagation in SWCNTs and results are compared with molecular dynamic simulations.

Chapter 2

Background and Literature Review

This chapter provides a brief review and essential background knowledge about non-local plate and shell models for graphene and CNTs. Section 2.1 introduces the lattice geometry of graphene and CNT. Section 2.2 presents two basic plate and shell theories that will be used in following chapters. Section 2.3 briefly reviews traditional local plate and shell representation of graphene and CNTs. Section 2.4 reviews the development of non-local elasticity and its applications on graphene and CNTs.

2.1 Geometry of graphene and carbon nanotubes

Single-layer graphene sheets and single-walled carbon nanotubes have very typical 2D geometries. In pristine SLGS and SWCNT there is only one atom layer in one dimension. And in the other two dimensions the carbon atoms form a honey-comb like lattice in a flat plane (graphene) or a cylindrical surface (CNT). This lattice can be seen as a repetitive pattern of a two-carbon-atom unit cell. It is intuitive that a CNT can be treated as a rolled piece of graphene. (See Fig. (1.1)) For pristine graphene there is only one type of lattice. However, there can be infinite types of CNT lattice, because there are infinite rolling

methods, which also endow CNTs with different properties, including elastic constants.

Contrary to the earlier belief that the elastic constants are insensitive to CNT's radius and chirality, more recent results have shown otherwise [66]. Ab intio calculations indicated that the CNT elastic properties are changing with different chiralities [70]. Results from separate studies showed that the Young's modulus varies with CNT's radius, especially when it is small [43, 82, 14]. Wang [87] showed that the bending modulus of CNTs depends on their radius and chirality. Huang et al [31] further demonstrated theoretically the variation of elastic constants with radius and chirality. Therefore, obtaining accurate tube radius, especially for small CNTs, is critical in the continuum models predicting the mechanical behavior of CNTs.

The dynamic behavior of CNTs is also geometry dependent. A special vibrational mode of CNTs, called the radial breathing mode (RBM), has attracted much attention in recent years as it can serve as the "fingerprint" of CNTs [27]. In Raman spectroscopy of CNTs, there are four Raman bands that are strongly resonance enhanced. One of them is the RBM in which all carbon atoms are vibrating along the radial direction [37]. It has been shown that the RBM frequency is highly dependent on the tube radius [69], leading to the idea that it can be used to identify the radius and chirality of a given CNT sample. However, a CNT's radius varies with its chirality and CNTs with different chiralities may have similar radii. The effectiveness of the RBM frequency based CNT identification relies on an accurate model describing the relations of the radius, chirality and RBM frequency of CNTs.

Many models have been developed to obtain the equilibrium structure of CNTs. A popular approach is the simple rolling approach. There are two rolling methods in the simple rolling approach, namely cylinder model and skeleton model (or ball-and-stick model) [38]. The cylinder model rolls a graphene sheet into a CNT like a piece of paper. This method assumes that the carbon atoms and bonds are all on the cylindrical surface

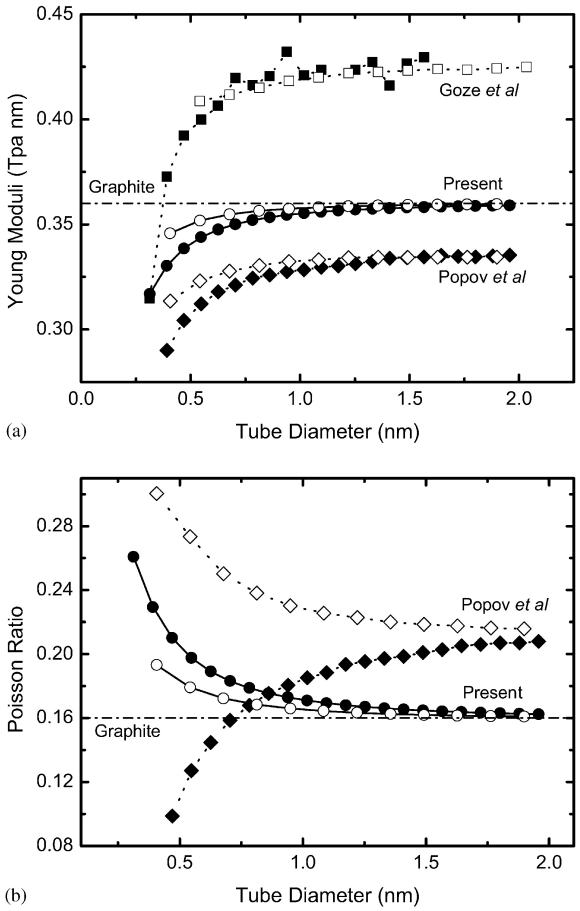

Figure 2.1: Geometry dependent Young's modulus and Poisson's ratio of carbon notubes [14]

after rolling, which implies curved bonds in the CNT. To eliminate this artificial effect, the skeleton model assumes that the bonds remain straight with fixed length during the rolling process. However, in actual cases, due to the symmetry breaking in the rolling process, both the angle and length of the bonds are adjusted to reach the minimum potential energy of CNT. Therefore, the assumptions in the simple rolling models are not accurate [70, 38], especially for CNTs with small radius. The interactions between atoms must be accounted for in the determination of a CNT's equilibrium structure. In this regard, molecular dynamics or first principle simulations have been employed to relax the structure of CNT. The balanced atomic structure can be obtained by minimizing the potential energy of the

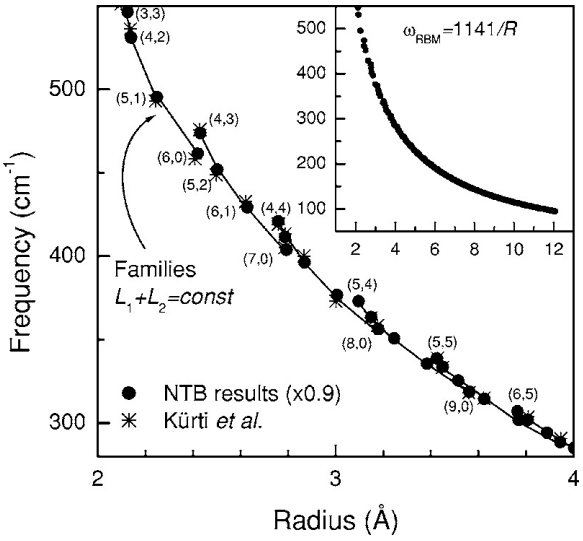

Figure 2.2: RBM frequencies of carnbon nanotubes with different radius and chiralities [62]. Results marked by stars are from Kürti's first principle simulations [38]

whole atom system. While these atomistic methods are more accurate than the simple rolling approach, their computational cost is typically very high. To efficiently and accurately obtain the equilibrium geometry of CNTs, Jiang et al [35] developed a lattice mechanics model with 5 independent lengths representing the geometry of a CNT. However, since the potential energy cannot be explicitly expressed in terms of these 5 length variables, their method still largely relies on a numerical solution of the nonlinear system. For the RBM frequency analysis, several models have been proposed to calculate the relation between the RBM frequency and the tube radius [27]. Most of the resent results are based on the tight-binding approximation [61, 62], zone folding force constant model [68, 100], ab initio calculations [37, 38, 39], and molecular structural mechanics models (i.e. stick-spiral models) [93, 13, 15] which consider the energies from bond stretching, bond twisting and bond angle variation separately.

2.2 Classical plate and shell theories

In continuum mechanics, a body can be simplified with a degenerated model, if there is one or more dimensions along which this body has significantly smaller scale than along other dimensions. For instance, a body can be modeled as a beam if its geometry is more like a segment or curve. Similarly, flat surfaces can be approximated by plate models, and curved surfaces can be approximated by shell models.

In general, a graphene sheet at equilibrium state can be treated as thin plates, in which bending is considered to be the only out-of-plane deformation. In the classical pure-bending plate theory it is assumed that [67]:

1. Straight lines that are normal to the plate's neutral surface (middle surface for homogeneous materials) remain straight after deformation;

2. These straight lines also remain normal to the neutral surface after deformation;

3. These straight lines also remain its original length after deformation.

This is called the Kirchhoff-Love assumption. The deformation field expressed in Cartesian coordinates can be expressed as: [67]

$$\begin{aligned} u(x_1, x_2, x_3, t) &= u_0(x_1, x_2, t) - x_3 \frac{\partial w_0}{\partial x} \\ v(x_1, x_2, x_3, t) &= v_0(x_1, x_2, t) - x_3 \frac{\partial w_0}{\partial y} \\ w(x_1, x_2, x_3, t) &= w_0(x_1, x_2, t) \end{aligned} \tag{2.1}$$

where u,v,w represents the displacements of point (x_1, x_2, x_3) in x_1, x_2 and x_3 directions. u_0,v_0,w_0 and the corresponding values at the neutral surface.

The equations of motion of a flat plate can be written as:

$$\begin{aligned}
&\frac{\partial N_{11}}{\partial x_1} + \frac{\partial N_{12}}{\partial x_2} - I_0 \frac{\partial^2 u}{\partial t^2} = 0 \\
&\frac{\partial N_{12}}{\partial x_1} + \frac{\partial N_{22}}{\partial x_2} - I_0 \frac{\partial^2 v}{\partial t^2} = 0 \\
&\frac{\partial^2 M_{11}}{\partial {x_1}^2} + \frac{\partial^2 M_{22}}{\partial {x_2}^2} - 2\frac{\partial^2 M_{12}}{\partial x_1 \partial x_2} = -q + \rho h \frac{\partial^2 w}{\partial t^2}
\end{aligned} \tag{2.2}$$

where the resultant forces N and moments M can be obtained by:

$$\begin{bmatrix} N_{11} \\ N_{22} \\ N_{12} \\ M_{11} \\ M_{22} \\ M_{12} \end{bmatrix} = \begin{bmatrix} \int_{-h/2}^{h/2} \sigma_{11} dx_3 \\ \int_{-h/2}^{h/2} \sigma_{22} dx_3 \\ \int_{-h/2}^{h/2} \sigma_{12} dx_3 \\ \int_{-h/2}^{h/2} \sigma_{11} x_3 dx_3 \\ \int_{-h/2}^{h/2} \sigma_{22} x_3 dx_3 \\ \int_{-h/2}^{h/2} \sigma_{12} x_3 dx_3 \end{bmatrix} = \begin{bmatrix} \mathbf{A}_{3\times 3} & \\ & \mathbf{D}_{3\times 3} \end{bmatrix} \begin{bmatrix} \epsilon_{11} \\ \epsilon_{22} \\ \gamma_{12} \\ \kappa_{11} \\ \kappa_{22} \\ \kappa_{12} \end{bmatrix} \tag{2.3}$$

$$\begin{bmatrix} \epsilon_{11} \\ \epsilon_{22} \\ \gamma_{12} \end{bmatrix} = \begin{bmatrix} \frac{\partial}{\partial x_1} & \\ & \frac{\partial}{\partial x_2} \\ \frac{\partial}{\partial x_2} & \frac{\partial}{\partial x_1} \end{bmatrix} \begin{bmatrix} u \\ \\ v \end{bmatrix}, \quad \begin{bmatrix} \kappa_{11} \\ \kappa_{22} \\ \kappa_{12} \end{bmatrix} = \begin{bmatrix} \frac{\partial}{\partial x_1} & \\ & \frac{\partial^2 w}{\partial {x_2}^2} \\ \frac{\partial^2 w}{\partial {x_2}^2} & \frac{\partial^2 w}{\partial x_1 \partial x_2} \end{bmatrix}$$

Matrix $\mathbf{A}$ and $\mathbf{D}$ are the in-plane stiffness matrix and bending stiffness matrix, respectively.

For traditional isotropic homogeneous materials, they can be expressed as:

$$\mathbf{A} = \begin{bmatrix} A & \nu A & \\ \nu A & A & \\ & & \dfrac{1-\nu}{2}A \end{bmatrix} \qquad \mathbf{D} = \begin{bmatrix} D & \nu D & \\ \nu D & D & \\ & & \dfrac{1-\nu}{2}D \end{bmatrix} \tag{2.4}$$

where

$$A = \frac{Et}{1-\nu^2}\,, \qquad D = \frac{Et^3}{12(1-\nu^2)} \tag{2.5}$$

For CNTs, we need to extend Eq. (2.2) into curved surfaces. In Cartesian coordinate system, the general form of doubly-curved shell model's equations of motion can be written as [67]:

$$\begin{aligned}
&\frac{\partial N_{11}}{\partial x_1} + \frac{\partial (N_{12} + C_0 M_{12})}{\partial x_2} + \frac{Q_1}{R_1} - I_0 \frac{\partial^2 u}{\partial t^2} - I_1 \frac{\partial^2 \theta_x}{\partial t^2} = 0 \\
&\frac{\partial (N_{12} - C_0 M_{12})}{\partial x_1} + \frac{\partial N_{22}}{\partial x_2} + \frac{Q_2}{R_2} - I_0 \frac{\partial^2 v}{\partial t^2} - I_1 \frac{\partial^2 \theta_y}{\partial t^2} = 0 \\
&\frac{\partial Q_1}{\partial x_1} + \frac{\partial Q_2}{\partial x_2} - \left(\frac{N_{11}}{R_1} + \frac{N_{22}}{R_2} \right) - q - I_0 \frac{\partial^2 w}{\partial t^2} = 0 \\
&\frac{\partial M_{11}}{\partial x_1} + \frac{\partial M_{12}}{\partial x_2} - Q_1 - I_1 \frac{\partial^2 u}{\partial t^2} - I_2 \frac{\partial^2 \theta_x}{\partial t^2} = 0 \\
&\frac{\partial M_{12}}{\partial x_1} + \frac{\partial M_{22}}{\partial x_2} - Q_2 - I_1 \frac{\partial^2 v}{\partial t^2} - I_2 \frac{\partial^2 \theta_y}{\partial t^2} = 0
\end{aligned} \tag{2.6}$$

As shown in Fig. (2.3), $N_{\alpha\beta}$ and $M_{\alpha\beta}$, $\alpha, \beta = 1$ or 2 are resultant forces and moments; Q_α represents the out-of-plane resultant shear forces; R_α are curvatures of the shell; q is the external pressure applied on the surface; and I_0, I_1 and I_2 are the first, second and third area moments of inertia, respectively. And the parameter C_0 is defined as:

$$C_0 = \frac{1}{R_1} - \frac{1}{R_2} \tag{2.7}$$

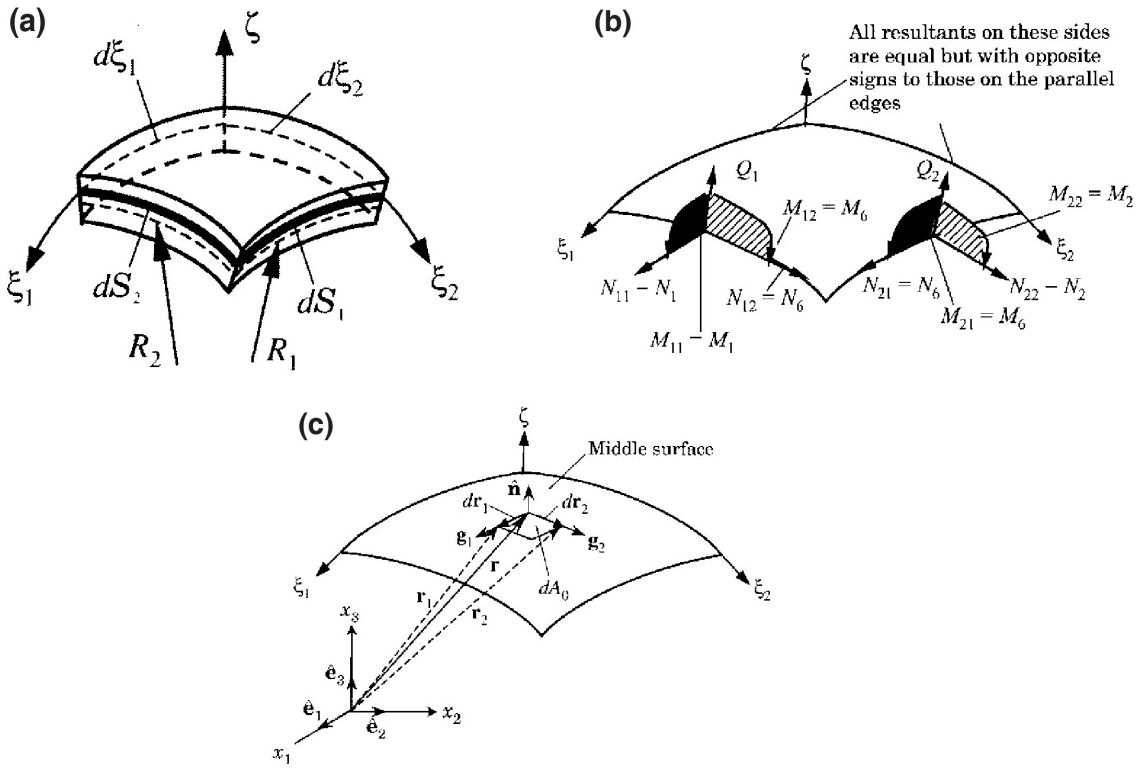

Figure 2.3: Demonstration of (a) the shell geometry, (b) resultant forces and (c) coordinate systems [67].

Normally CNTs should also be treated as thin structures. However, pure-bending models require C_1 continuity in weak form, which can cause problems in finite element shell simulations. To avoid this issue, the first-order shear deformation model is employed. In this model, the second item of Kirchhoff's hypothesis is removed. With other items still valid, the new expression of the deformation field in Cartesian coordinates are as follows:

$$\begin{aligned} u(x_1, x_2, z, t) &= u_0(x_1, x_2, t) - x_3\theta_1 \\ v(x_1, x_2, z, t) &= v_0(x_1, x_2, t) - x_3\theta_2 \\ w(x_1, x_2, z, t) &= w_0(x_1, x_2, t) \end{aligned} \tag{2.8}$$

Here θ_1, θ_2 are two new rotational degrees of freedom. Therefore, the corresponding constitutive relations and strain-displacement relations are

$$\begin{bmatrix} N_{11} \\ N_{22} \\ N_{12} \\ Q_1 \\ Q_2 \\ M_{11} \\ M_{22} \\ M_{12} \end{bmatrix} = \begin{bmatrix} \mathbf{A}_{3\times3} & & \\ & \mathbf{C}_{2\times2} & \\ & & \mathbf{D}_{3\times3} \end{bmatrix} \begin{bmatrix} \epsilon_{11} \\ \epsilon_{22} \\ \gamma_{12} \\ \gamma_{13} \\ \gamma_{23} \\ \kappa_{11} \\ \kappa_{22} \\ \kappa_{12} \end{bmatrix} \tag{2.9}$$

$$\begin{bmatrix} \epsilon_{11} \\ \epsilon_{22} \\ \gamma_{12} \end{bmatrix} = \begin{bmatrix} \frac{\partial}{\partial x_1} & \\ & \frac{\partial}{\partial x_2} \\ \frac{\partial}{\partial x_2} & \frac{\partial}{\partial x_1} \end{bmatrix} \begin{bmatrix} u \\ v \end{bmatrix}, \quad \begin{bmatrix} \gamma_{13} \\ \gamma_{23} \end{bmatrix} = \begin{bmatrix} \frac{\partial}{\partial x_1} & -1 & \\ \frac{\partial}{\partial x_2} & & -1 \end{bmatrix} \begin{bmatrix} w \\ \theta_1 \\ \theta_2 \end{bmatrix}, \quad \begin{bmatrix} \kappa_{11} \\ \kappa_{22} \\ \kappa_{12} \end{bmatrix} = \begin{bmatrix} \frac{\partial}{\partial x_1} & \\ & \frac{\partial}{\partial x_2} \\ \frac{\partial}{\partial x_2} & \frac{\partial}{\partial x_1} \end{bmatrix} \begin{bmatrix} \theta_1 \\ \theta_2 \end{bmatrix}$$

where $\mathbf{C}$ is the out-of-plane shear stiffness matrix. For isotropic homogeneous materials, $\mathbf{C}$ is normally set to be:

$$\mathbf{C} = \begin{bmatrix} kG & \\ & kG \end{bmatrix} \tag{2.10}$$

$G = \dfrac{Et}{1+\nu}$ is the in-plane shear modulus and k is called the shear correction factor. In general, k is set to be $\frac{5}{6}$.

2.3 Constitutive relations of graphene and carbon nanotubes

While the classical plate models use wall thickness to define the cross-sectional properties (matrices $\mathbf{A}$ and $\mathbf{D}$), the thickness is not well defined for a single layer of carbon atoms. As mentioned in the previous chapter, many studies have measured the Young's modulus and Poisson's ratio of graphene and CNTs through stretching test. However, the thickness of graphene and CNTs was simply set as the spacing between two layers of carbon atoms in graphite, approximately 0.34 nm. As a result, the Young's modulus of graphene and CNTs is determined to be around 1 TPa. Together with Eq. (2.4) and Eq. (2.10), the stiffness matrices should be easily obtained. But this thickness was challenged by Yakobson. In 1995, he calculated D and A with MD simulations. The CNT was treated as a cylindrical deformed shell of graphene, and its strain energy is approximated by the variation of CNT's potential energy with respect to graphene. He found out that the D = 0.85 eV and A = 360 J/m. From the relation between A and D given in Eq. (2.4) and (2.10), it leads to the Young's modulus E = 5.5 TPa and the thickness h = 0.066 nm, which is only about 1/5 of 0.34 nm [94]. This disagreement on the wall thickness is called "Yakobson Paradox". Fig. (2.4) shows different thickness values that have been used in literature. Pantano [56] also addressed this issue in his paper, and he tested the buckling of CNTs in shell model with different wall thickness which is shown in Fig. (2.5).

To avoid this problem, some researchers have tried to directly calculate the cross-sectional structural properties of graphene using atomistic description of the atoms. In 2006 Huang [31] derived potential-oriented expressions for stiffness matrices. He showed that $\mathbf{A}$ and $\mathbf{D}$ matrices obtained from Eq. (2.4) cannot represent the constitutive relations of graphene and SWCNT. He also explained why there are disagreements on the number of wall thickness. The way to obtain the wall thickness which is based on the traditional rela-

Authors	Method	Wall thickness (nm)	Young's modulus (TPa)
Lu[a]	Molecular dynamics	0.34	0.974
Hernández *et al.*[b]	Tight binding molecular dynamics	0.34	1.24
Odegard *et al.*[c]	Equivalent-continuum modeling	0.69	
Li and Chou[d]	Structural mechanics: stiffness matrix method	0.34	1.01
Jin and Yuan[e]	Molecular dynamics	0.34	1.238
Tserpes and Papanikos[f]	Structural mechanics: FE method	0.147	
Yakobson *et al.*[g]	Molecular dynamics	0.066	5.5
Zhou *et al.*[h]	Tight-binding model	0.074	5.1
Kudin *et al.*[i]	*Ab inito* computations	0.089	3.859
Tu and Ou-yang[j]	Local density approximation model	0.075	4.7
Vodenitcharova and Zhang[k]	Ring theory continuum mechanics	0.0617	4.88
Panatano *et al.*[l]	Continuum shell modeling	0.075	4.84
Goupalov[m]	Continuum model for long-wavelength phonons	0.087	
Wang *et al.*[n]	Ab *initio* calculation	0.0665	5.07

Figure 2.4: Different wall thickness used and the corresponding Young's modulus in literature[31]

tions among stiffness properties for homogeneous materials, just like what Yakobson did, can result in different thicknesses under different loading cases, as shown in Fig. (2.6). So thickness-free expressions of $\mathbf{A}$ and $\mathbf{D}$ are better descriptions of the mechanical properties of graphene and CNTs.

Similar to Huang's effort, Arroyo [7] and Wu [92] also derived potential-based stiffness matrices for CNTs. Using exponential Cauchy-Born rule, Arroyo deduced expressions of in-plane stiffness matrix and bending stiffness matrix as functions of the differentiation of inter-atomic potential energy. Further more, Wu developed a finite deformation shell theory in which he expressed the inter-atomic potential energy as a function of the Green's strain and curvature. This makes it possible that the stiffness matrices of CNT can be directly obtained from the differentiation of inter-atomic potential energy.

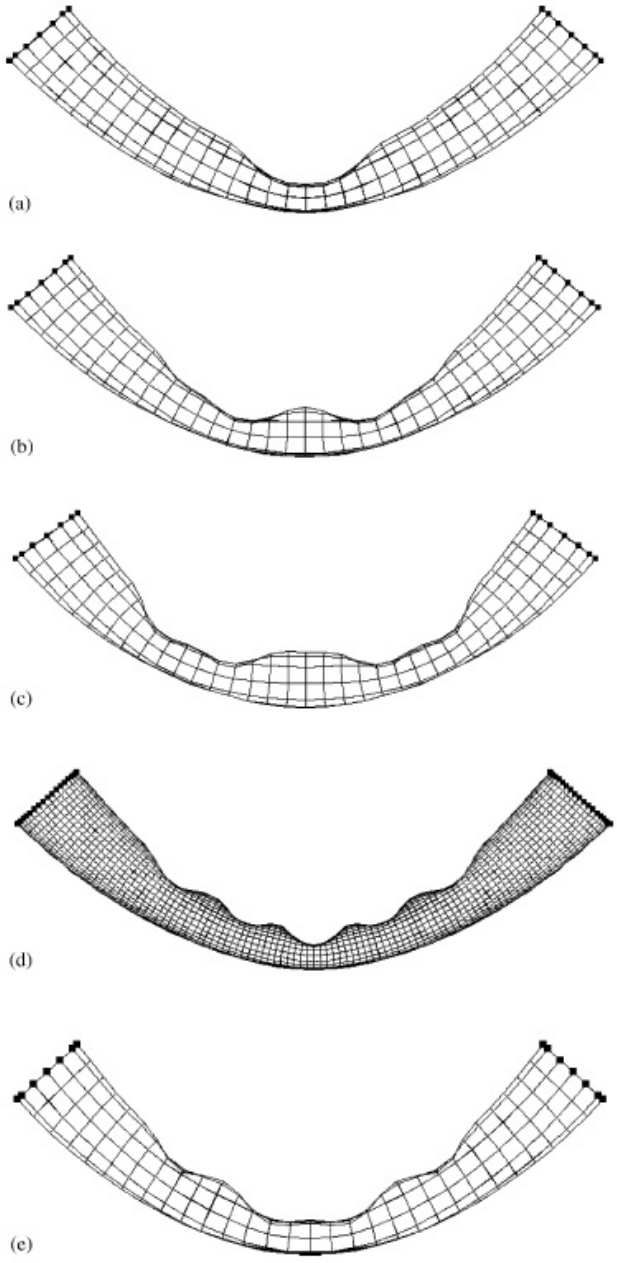

Figure 2.5: Buckling of 8 nm (13,0) carbon nanotube using shell model with different configuration and wall thickness.[56]

	Thickness	Young's modulus	Poisson's ratio
Uniaxial tension	0.0618 nm	3.81 TPa	0.412
Uniaxial stretching	0.0734 nm	3.21 TPa	0.412
Equibiaxial stretching	0.0874 nm	2.69 TPa	0.412

Figure 2.6: Wall thickness under different test methods[31]

2.4 Non-local elasticity and its applications on graphene and carbon nanotubes

In the classical theory of elasticity, the stress at a given point is only affected by the strain at the same point. But when the scale of interest goes down to atomic level, the range of atomic cohesive forces cannot be ignored. To take this effect into consideration, Eringen derived a theory that is called the non-local elasticity [19]. In this theory, the stress at a given point is not only determined by the strain at the same point, but also affected by the strain field around this point [19]. Mathematically, the stress tensor is expressed as an integration of a function of the strain field: [19]

$$\boldsymbol{\sigma}(\mathbf{x}) = \int_{\Omega} \alpha(|\mathbf{x}' - \mathbf{x}|, \tau)\mathbf{C} : \boldsymbol{\epsilon}(\mathbf{x}')d\Omega(\mathbf{x}') \tag{2.11}$$

where $\mathbf{x}$, $\mathbf{x}'$ are position vectors, $\boldsymbol{\sigma}$ and $\boldsymbol{\epsilon}$ are stress and strain tensors, and $\mathbf{C}$ is the 4th-rank stiffness tensor defined in traditional theory of elasticity. The weight function $\alpha(|\mathbf{x}' - \mathbf{x}|, \tau)$ is called the non-local modulus. The parameter τ in the non-local modulus is given by $\tau = e_0 a/l$ where a and l are the internal and external characteristic lengths of the lattice, and e_0 is a scaling factor. The combined term $e_0 a$ is also called the non-local parameter. When $\alpha(|\mathbf{x}' - \mathbf{x}|, \tau)$ is chosen to be the Green's function of a linear differential

operator $\mathscr{L}$, it has been shown that Eq. (2.11) can be rewritten as

$$\mathscr{L}\boldsymbol{\sigma} = \mathbf{C} : \boldsymbol{\epsilon} \tag{2.12}$$

For example, if α has the form

$$\alpha(|\mathbf{x}|, \tau) = (2\pi l^2 \tau^2)^{-1} K_0(\mathbf{x} \cdot \mathbf{x}/l\tau) \tag{2.13}$$

where K_0 is the modified Bessel function of second kind with $\nu = 0$. Then we have $\mathscr{L} = 1 - \tau^2 l^2 \nabla^2 = 1 - (e_0 a)^2 \nabla^2$ where ∇^2 is the Laplacian operator. Substituting $\mathscr{L}$ in Eq. (2.12), we have [18]

$$\left(1 - (e_0 a)^2 \nabla^2\right) \boldsymbol{\sigma} = \mathbf{C} : \boldsymbol{\epsilon} \tag{2.14}$$

Recently the non-local theory is revisited for continuum simulations of graphene and CNTs. Lu has derived a non-local plate theory based on Eq. (2.14) [47]. In this model, the resultant forces and moments are given by:

$$\begin{aligned} \left(1 - (e_0 a)^2 \nabla^2\right) N_{\alpha\beta} &= N^L_{\alpha\beta} \\ \left(1 - (e_0 a)^2 \nabla^2\right) M_{\alpha\beta} &= M^L_{\alpha\beta} \end{aligned} \qquad \alpha,\ \beta = 1, 2 \tag{2.15}$$

Where $N^L_{\alpha\beta}$ and $M^L_{\alpha\beta}$ are local resultant forces and moments defined in Eq. (2.4). The

non-local equations of motion can be expressed as: [47]

$$\begin{aligned}
&\frac{\partial \mathscr{L} N_{11}}{\partial x_1} + \frac{\partial \mathscr{L} N_{12}}{\partial x_2} - I_0 \mathscr{L} \frac{\partial^2 u}{\partial t^2} = 0 \\
&\frac{\partial \mathscr{L} N_{12}}{\partial x_1} + \frac{\partial \mathscr{L} N_{22}}{\partial x_2} - I_0 \mathscr{L} \frac{\partial^2 v}{\partial t^2} = 0 \\
&\frac{\partial \mathscr{L} Q_1}{\partial x_1} + \frac{\partial \mathscr{L} Q_2}{\partial x_2} - \mathscr{L} q - I_0 \mathscr{L} \frac{\partial^2 w}{\partial t^2} = 0 \\
&\frac{\partial \mathscr{L} M_{11}}{\partial x_1} + \frac{\partial \mathscr{L} M_{12}}{\partial x_2} + \mathscr{L} Q_1 = 0 \\
&\frac{\partial \mathscr{L} M_{12}}{\partial x_1} + \frac{\partial \mathscr{L} M_{22}}{\partial x_2} + \mathscr{L} Q_2 = 0
\end{aligned} \tag{2.16}$$

Lu also further derived the non-local governing equations in terms of displacements for both classical Kirchhoff plate and the first-order shear deformation plate (Mindlin plate).

In 2010 Ansari [3] employed this non-local plate theory to vibrational simulations of single-layered graphene sheets. In his paper, the governing equation of non-local Mindlin plate model was solved by generalized differential quadrature (GDQ) method. The fundamental natural frequency of graphene with different boundary conditions was calculated and compared with MD results. With properly chosen non-local parameters, results from the non-local plate model were shown to be very close to MD simulations. Arash also published his work in 2012 using non-local Kirchhoff plate model of graphene [5]. He established a non-local finite element plate model and investigated the transverse wave propagation problems of a graphene nano-ribbon. Results shown in Fig. (2.7) also indicated that the non-local model is much more accurate than the local one. This improvement is more obvious when the wave number becomes larger.

For CNTs, there are two different types of non-local models that have been proposed [88]. The first type is the non-local beam model which is suitable for long narrow tubes. In 2005 L Wang [84] published his study on the wave propagation in a SWCNT with non-local beam models. He developed non-local Euler and Timoshenko beam mo-

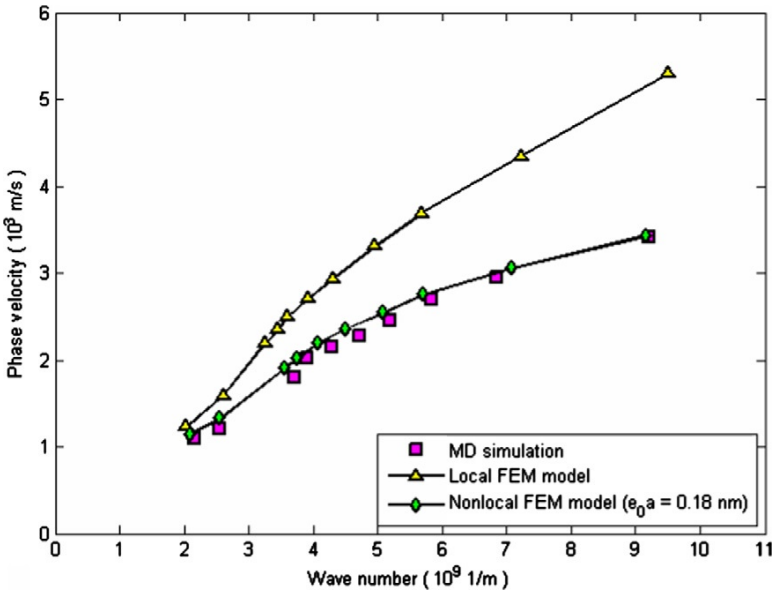

Figure 2.7: Wave proagation of a graphene nano-ribbon [5]

dels for CNT and derived corresponding analytical solutions for flexural wave propagation problems. Shown in Fig. (2.8), results from non-local models on (5,5) and (10,10) CNTs showed great improvement against local results. The dispersion curve obtained from the non-local model fits much better to MD simulation results than the local ones. In 2007 Lu further applied the non-local beam models on multi-walled carbon nanotubes [46]. The second approach is the non-local shell model. In 2004 Zhang and his colleague implemented a non-local shell model for multi-walled CNT and discussed the effect of the non-local parameter [99]. Later Wang [89] has derived the wave propagation solution of this non-local shell model for CNT. This model is applied by Hu [29] to single- and double-walled carbon nanotubes. He derived analytical solutions for torsional wave propagations in CNTs and he compared his results with MD simulations. Similar to the non-local plate models of graphene and non-local beam models of CNT, his work indicated that the non-local shell model matches better to the atomic results than its local counterpart. Some of his results are shown in Fig. (2.9).

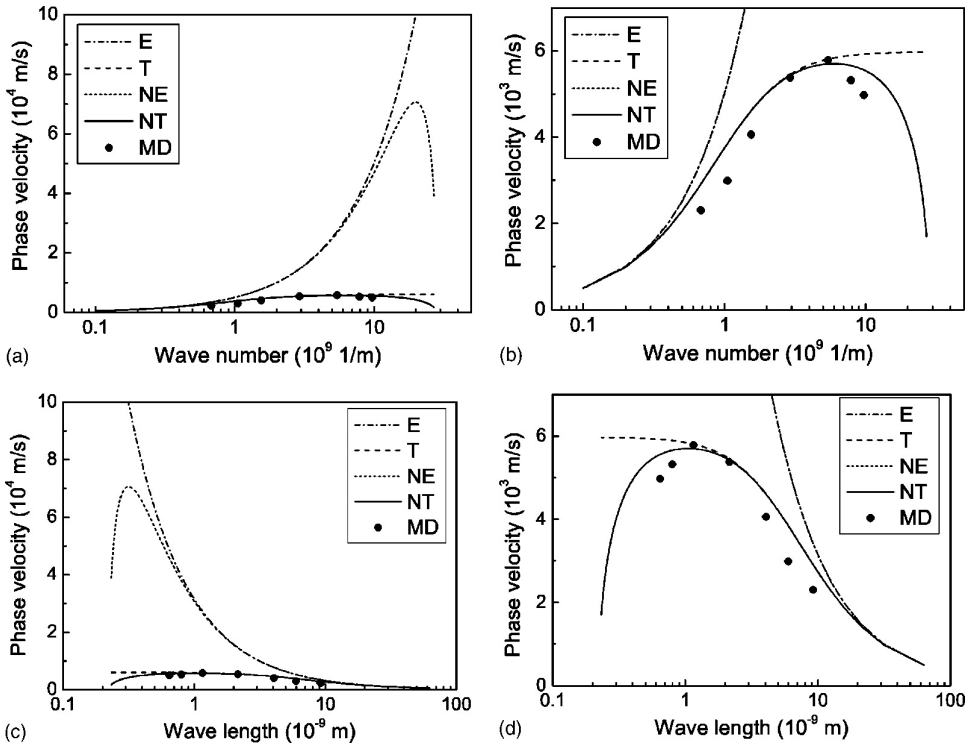

Figure 2.8: The dispersion relation of armchair (5,5) carbon nanotube[84]

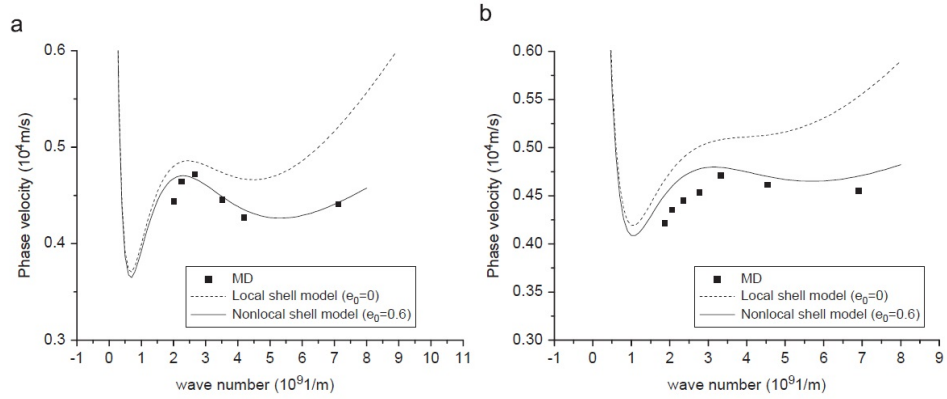

Figure 2.9: The dispersion relation of transverse waves in (15,15) armchair and (20,0) zigzag carbon nanotubes[29]

In the non-local theory, the non-local parameter $e_0 a$ defined in Eq. (2.11) has vital importance since it represents the magnitude of the non-local effect. When $e_0 a = 0$ the non-local elasticity regresses to the traditional local theory. However, so far there is no

convincible method that can determine this parameter for graphene and CNTs. In Wang's beam model [84] he used 0.0355 nm, which is $1/\sqrt{12}$ of the longitudinal distance between two adjacent atom rings in CNT. This formula is theoritically derived by Askes and his colleagues [8]. But this number is not supported by other researches. Currently the most popular practice is by fitting the non-local results with atomic level simulations. Ansari [3] used 1.41 nm and 1.43 nm for simply supported squared graphene sheet, and 0.87 nm and 0.71 nm for clamped squared graphene sheet. Arash [4] tried to evaluate the e_0a for the non-local shell model of SWCNT, and he obtained that it is around 1.6 nm to 2.0 nm based on the chosen wall thickness and boundary conditions. In Hu's wave propagation investigation with non-local shell model [29], he fixed $a = 0.142nm$, which is the balanced carbon bond length of graphite. And e_0 was selected from 0.2 to 0.6, based on the type of the wave. That is equivalent to e_0a from 0.0284 nm to 0.0852 nm. It can be seen that the maximum e_0a used in literature is nearly 50 times of the smallest one.

2.5 Research questions

From the review given above, before the work introduced in this dissertation, there are several questions remain unclear, which will be answered at the end of this dissertation:

1. Why are there so many non-local parameters used in literature? What factors can affect this number?

2. So far, most non-local parameters are obtained by fitting with atomic simulations. If these affecting factors are determined, is there a way to predict the non-local parameter without running atomic simulations?

3. It is shown that the non-local parameter can reduce the error of dynamic simulations on graphene and CNT. But where are these errors from? A lot of non-local models

employed constitutive relations of traditional continuum materials, which has already been proven to be wrong. Is it a robust way that using the non-local model to fix errors which may caused by improper constitutive relations?

This work aim to answer the above research questions by performing the following tasks:

1. Develop a method that can directly calculate the relaxed radius, bond length and angles for any CNT. This is important since the elastic properties of CNTs are highly dependent on these geometrical properties. The CNT geometry is represented by a few parameters. And using engineering optimization method, their values at equilibrium state are calculated.

2. Establish an accurate local plate model of graphene. To achieve that we apply potential-oriented elastic constants, combined with the consideration of boundary conditions. The accuracy of the local models is tested by static tests which is not affected by the non-local parameter. Then the errors from the local model can be evaluated.

3. Based on the accurate local plate model, the non-local elasticity is introduced. To determine proper values of the non-local parameter, the effect of this parameter is evaluated by comparing the natural frequencies obtained from local, non-local and atomic models. And a size and shape study is also performed. Then the above questions can be answered for the non-local plate model of graphene.

4. To further answer these questions on CNT, the non-local plate model is extended to a curved shell model. With similar tests to the plate model, we should be able to find corresponding answers to these questions for the non-local shell model of CNT.

Chapter 3

Semi-analytical approach for calculating the equilibrium structure and radial breathing mode frequency of single-walled carbon nanotubes

In this chapter, we present a semi-analytical model for obtaining the equilibrium geometry and RBM frequencies of single-wall CNTs. The model employs 2 bond lengths along with 3 bond angles as independent variables, which enables analytical differentiation of interatomic potential functions. With the analytical expressions of the derivatives, the equilibrium geometry of CNTs can be obtained by using an energy minimization procedure which is performed by using the conjugate gradient optimization method. Having obtained the equilibrium geometry of the CNTs, the RBM frequencies can be calculated analytically for a given multi-body potential, which, to the authors' best knowledge, has not been done previously in the literature. While the model is general and applicable to different multi-body potentials, its effectiveness is demonstrated by using the reactive empirical bond order

(REBO) potential [11]. Content of this chapter is already published in Acta Mechanica Sinica [28].

3.0.1 CNT Geometry and atomic bond-order potential

A sufficiently long single-wall CNT with open ends can be regarded as a pattern of repeating 2-atom unit cells except for a small region close to the ends. Moreover, in each unit cell, there is a so-called C_2-axis rotational symmetry [38], as shown in Fig. 3.1. Due to the C_2-axis rotational symmetry, a unit cell can be defined by one atom with its three nearest neighbors. It is often more convenient to represent the atom positions by using bond lengths and angles. Therefore, as shown in Fig. 3.1, given the position of any atom with the lengths (denoted as r) and angles (denoted as θ) of its three bonds, the entire structure of a CNT can be determined.

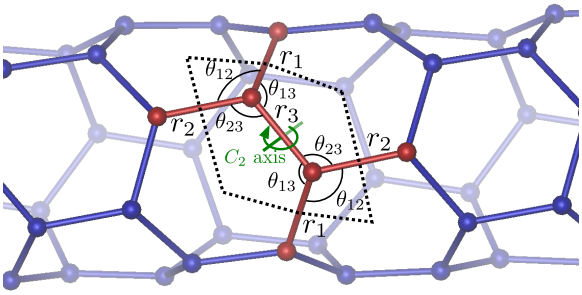

Figure 3.1: Carbon nanotube: unit cell and C_2-axis symmetry.

Interaction of the carbon atoms in a CNT can be described by bond-order potentials. For CNTs, popular multi-body potentials include the Tersoff [78], Brenner [12] and Stillinger-Weber [76] potentials, etc. In general, the total potential energy of a system of N atoms can be written as $W = \frac{1}{2}\sum_{a\neq b} V_{ab}$, $a, b = 1, 2, ..., N$, where V_{ab} is the interatomic potential between atoms a and b and is a function of bond length and bond angle. Due to the symmetry of carbon atoms in a CNT, the potential energy of a unit cell can be expressed

as $w_0 = w_0(r_1, r_2, r_3, \theta_{12}, \theta_{23}, \theta_{13})$, where r_i and θ_{ij}, $i, j = 1, 2, 3$, are the length of bond i and angle between bonds i and j, respectively, as shown in Fig. 3.1.

3.1 Geometric Mapping

Although the skeleton model does not provide an accurate prediction of CNT radius, it offers a starting point to represent different types of CNTs. The skeleton model assumes that each C-C bond behaves as a rigid rod connecting two carbon atoms on the cylindrical surface. The mapping between the a CNT and its corresponding flat graphene is illustrated in Fig. 3.2. As shown in Fig. 3.2 (a), the bold dashed line represents the chiral vector direction (i.e. the rolling direction) of the 2-D graphene. The bond angles, α_1, α_2 and α_3, are defined with respect to the chiral vector. The positions of the 3 nearest neighbors of the center atom a are defined by the horizontal and vertical distances, l and h, from the center atom. Figure 3.2 (b) shows the 3-D positions of the 4 atoms after they are rolled into a CNT. The black circle represents the cross section. The positions of the 3 neighbor atoms are also defined by the horizontal and vertical distances from the center atom. An example of a chiral (or rolling) vector (4,1) for rolling into a (4,1) CNT is shown in Fig. 3.2 (c). Since in the simple rolling step, the bond lengths r_j and the distances $h_j = r_j|\sin(\alpha_j)|$, $l_j = r_j|cos(\alpha_j)|$ remain the same, it is obvious that the 3 chord lengths in Fig. 3.2 (b) are equal to l_1, l_2 and l_3 respectively. In the simple rolling model, given the chiral vector (M,N), the radius of a carbon nanotube can be determined by:

$$R = \frac{\sqrt{3}}{2\pi} a_{c-c} \sqrt{M^2 + N^2 + MN} \tag{3.1}$$

where a_{c-c} is the C-C bond length in a 2-D graphene sheet. Due to the asymmetric inter-atomic interactions between the carbon atoms, the bond lengths and angles are no longer the

same in a CNT. For this reason, further analysis is necessary to determine the equilibrium bond lengths and angles.

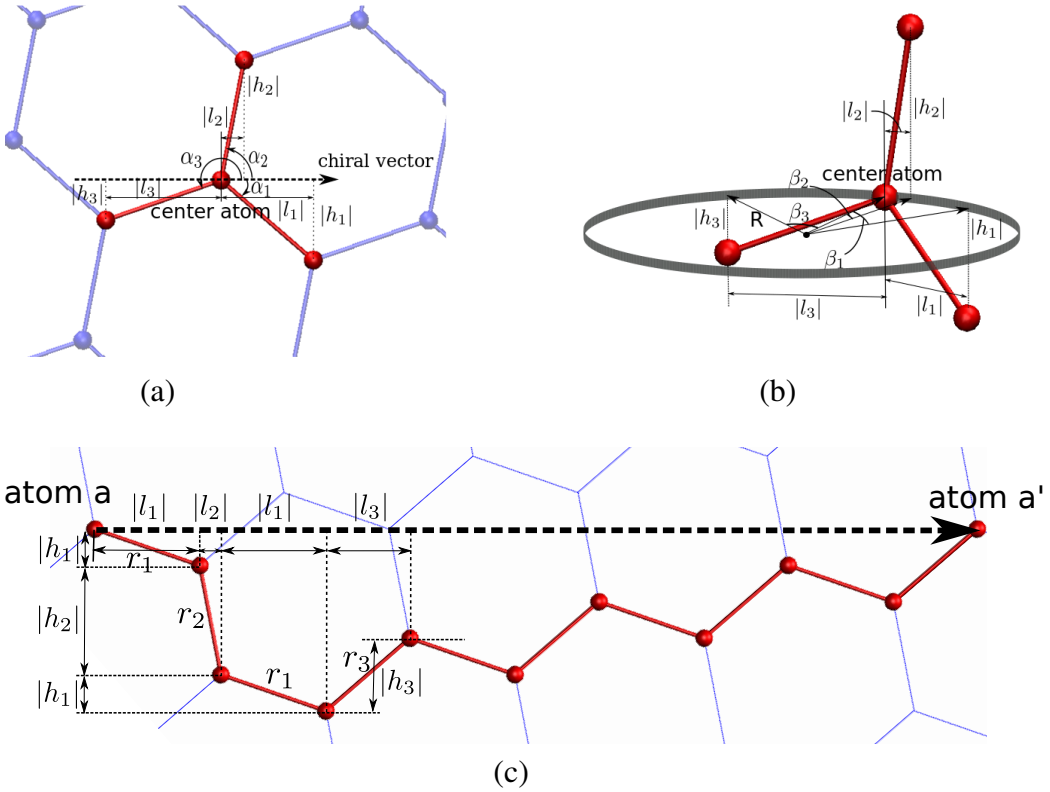

Figure 3.2: Geometric mapping of a CNT; (a) carbon atoms in 2-D graphene; (b) atoms mapped onto a CNT; (c) rolling of a (4,1) CNT.

As shown in Fig. 3.2(b), the central angles of the chords in the cross-section circle are

$$\beta_j = 2\sin^{-1}\left(\frac{l_j}{2R}\right), \qquad j = 1, 2, 3 \tag{3.2}$$

In order to form a closed cylindrical surface, atom a and atom a' in Fig. 3.2 (c) must be the same atom. It is easy to show that two geometric conditions must be satisfied: (1) the summation of the central angles of all corresponding chords (i.e. the βs) should be 2π and (2) the distance between atom a' and the chiral vector should be zero. Mathematically, the

first condition leads to

$$(M+N)\beta_1 - M\beta_2 - N\beta_3 = 2\pi \tag{3.3}$$

where M and N represent the chirality of a (M,N) CNT. The second condition can be written as

$$(M+N)h_1 - Mh_2 - Nh_3 = 0 \tag{3.4}$$

which gives

$$r_3 = \frac{1}{Nsin\alpha_3}\left[(M+N)\, r_1 \sin\alpha_1 - M r_2 \sin\alpha_2\right] \tag{3.5}$$

The angle between bonds j and k, θ_{jk}, can then be calculated by (see Appendix A for details):

$$\cos\theta_{jk} = \cos\alpha_j \cos\alpha_k T_j T_k + \frac{r_j r_k}{4R^2}\cos^2\alpha_j \cos^2\alpha_k + \sin\alpha_j \sin\alpha_k, \qquad j,k = 1,2,3 \qquad j \neq k \tag{3.6}$$

where

$$T_j = \sqrt{1 - \frac{r_j^2}{4R^2}\cos^2\alpha_j}, \qquad j = 1,2,3 \tag{3.7}$$

With the graphene-to-CNT mapping described above, the original potential energy function of a CNT unit cell, $w_0(r_1, r_2, r_3, \theta_{12}, \theta_{23}, \theta_{13})$, can be rewritten in terms of 7 variables: $w_0 = w(R, r_1, r_2, r_3, \alpha_1, \alpha_2, \alpha_3)$. Then, the bond angles, θ_{jk}, can be replaced by $R, \alpha_1, \alpha_2, \alpha_3$ following Eq. (3.6). Furthermore, R is an implicit function of $r_1, r_2, r_3, \alpha_1, \alpha_2, \alpha_3$, according

to Eq. (3.3). Equation (3.5) shows that r_3 can be expressed in terms r_1, r_2 and the angles. Therefore, the potential energy can be expressed in terms of 5 independent variables as

$$w_0 \quad = W(r_1, r_2, \alpha_1, \alpha_2, \alpha_3) = W(\mathbf{x}) \tag{3.8}$$

where the variable vector $\mathbf{x} = \{r_1, r_2, \alpha_1, \alpha_2, \alpha_3\}$.

3.2 Equilibrium structural configuration

To determine the actual radius of the CNT, it is necessary to calculate the equilibrium configuration of the carbon atoms. An energy minimization procedure using a line search method is adopted to determine the equilibrium configuration. Iteratively, a line search method determines a search direction and then perform single variable minimization to obtain the minimum position along the search direction. In this work, in light of the general form and typical behavior of C-C interatomic potentials, a first order conjugate gradient method [22] is employed to determine the search direction, and the Powell method [63] is used to carry out the single variable optimization along the search direction.

The conjugate gradient method starts with a steepest descend calculation. The initial bond lengths are set to be $r_1^0 = r_2^0 = a_{c-c}$ and the initial angles are given by

$$\begin{aligned} \alpha_1^0 &= \frac{\pi}{6} - tan^{-1}(\sqrt{3}N/(2M+N)), \\ \alpha_2^0 &= \alpha_1^0 + \frac{2\pi}{3}, \\ \alpha_3^0 &= \alpha_1^0 + \frac{4\pi}{3}. \end{aligned} \tag{3.9}$$

Therefore, the starting point of the optimization is $\mathbf{x}_0 = \{a_{c-c}, a_{c-c}, \alpha_1^0, \alpha_2^0, \alpha_3^0\}$. The

gradient of the potential energy function can be obtained using

$$\begin{aligned}
\frac{\partial W}{\partial r_j} &= \frac{\partial w}{\partial r_j} + \frac{\partial w}{\partial R}\frac{\partial R}{\partial r_j} + \frac{\partial w}{\partial r_3}\frac{\partial r_3}{\partial r_j} + \frac{\partial w}{\partial R}\frac{\partial R}{\partial r_3}\frac{\partial r_3}{\partial r_i}, && j = 1, 2, \\
\frac{\partial W}{\partial \alpha_j} &= \frac{\partial w}{\partial \alpha_j} + \frac{\partial w}{\partial R}\frac{\partial R}{\partial \alpha_j} + \frac{\partial w}{\partial r_3}\frac{\partial r_3}{\partial \alpha_j} + \frac{\partial w}{\partial R}\frac{\partial R}{\partial r_3}\frac{\partial r_3}{\partial \alpha_j}\ , && j = 1, 2, 3.
\end{aligned} \tag{3.10}$$

where

$$\begin{aligned}
\frac{\partial w}{\partial R} &= \sum_{j \neq k} \frac{\partial w_0}{\partial \cos\theta_{jk}} \frac{\partial \cos\theta_{jk}}{\partial R}, \\
\frac{\partial w}{\partial r_j} &= \frac{\partial w_0}{\partial r_j} + \frac{\partial w_0}{\partial \cos\theta_{jk}} \frac{\partial \cos\theta_{jk}}{\partial r_j}, \\
\frac{\partial w}{\partial \alpha_j} &= \frac{\partial w_0}{\partial \cos\theta_{jk}} \frac{\partial \cos\theta_{jk}}{\partial \alpha_j}.
\end{aligned} \tag{3.11}$$

The derivatives of $\cos\theta_{jk}, j, k = 1, 2, 3, j \neq k$ can be obtained from Eq. (3.6)

$$\begin{aligned}
\frac{\partial \cos\theta_{jk}}{\partial R} &= \cos\alpha_j \cos\alpha_k \left(\frac{\partial T_j}{\partial R} T_k + T_j \frac{\partial T_k}{\partial R} \right) - \frac{r_j r_k}{2R^3} \cos^2\alpha_j \cos^2\alpha_k \\
\frac{\partial \cos\theta_{jk}}{\partial r_j} &= \cos\alpha_j \cos\alpha_k \frac{\partial T_j}{\partial r_j} T_k + \frac{r_k}{4R^2} \cos^2\alpha_j \cos^2\alpha_k \\
\frac{\partial \cos\theta_{jk}}{\partial \alpha_j} &= -\sin\alpha_j \cos\alpha_k T_j T_k + \cos\alpha_j \cos\alpha_k \frac{\partial T_j}{\partial \alpha_j} T_k - \frac{r_j r_k}{2R^2} \cos\alpha_j \sin\alpha_j \cos^2\alpha_k + \cos\alpha_j \sin\alpha_k
\end{aligned} \tag{3.12}$$

The derivatives of R and r_3 can be obtained from Eq. (3.3) and (3.5) as

$$\begin{aligned}
\frac{\partial R}{\partial r_j} &= \frac{R D_j \cos\alpha_j}{r_j (D_1 + D_2 + D_3)} \\
\frac{\partial R}{\partial \alpha_j} &= \frac{-R D_j \tan\alpha_j}{D_1 + D_2 + D_3}
\end{aligned} \qquad j = 1, 2, 3 \tag{3.13}$$

$$
\begin{aligned}
\frac{\partial r_3}{\partial r_1} &= \frac{1}{N\sin\alpha_3}(M+N)\sin\alpha_1 \\
\frac{\partial r_3}{\partial r_2} &= -\frac{1}{N\sin\alpha_3}Msin\alpha_2 \\
\frac{\partial r_3}{\partial \alpha_1} &= \frac{1}{N\sin\alpha_3}(M+N)r_1\cos\alpha_1 \\
\frac{\partial r_3}{\partial \alpha_2} &= -\frac{1}{N\sin\alpha_3}Mr_2\cos\alpha_2, \\
\frac{\partial r_3}{\partial \alpha_3} &= -\frac{\cos\alpha_3}{N\sin^2\alpha_3}[(M+N)r_1\sin\alpha_1 - Mr_2\sin\alpha_2]
\end{aligned}
\tag{3.14}
$$

where

$$
D_1 = \frac{(M+N)l_1}{1-(l_1/2R)^2}, \qquad D_2 = \frac{-Ml_2}{1-(l_2/2R)^2}, \qquad D_3 = \frac{-Nl_3}{1-(l_3/2R)^2} \tag{3.15}
$$

The general procedure of the energy minimization is described as follows. For a given step k ($k = 0, 1, 2, \ldots, K-1$, where K is the number of variables), the objective is to compute a new position vector $\mathbf{x}_{k+1}$ toward the minimum point of the potential function. For $k = 0$, $\mathbf{x}_0$ is the initial position vector given by $\mathbf{x}_0 = \{a_{c-c}, a_{c-c}, \alpha_1^0, \alpha_2^0, \alpha_3^0\}$. Next, a single variable objective function $W_s(\eta) = W(\mathbf{x}_0 + \eta\mathbf{C}_0)$, where $\mathbf{C}_0 = -\nabla W(\mathbf{x}_0)$, is minimized along the $\mathbf{C}_0$ direction. Assuming η_{min} gives the minimum of $W_s(\eta)$, the position vector $\mathbf{x}$ is updated as $\mathbf{x}_1 = \mathbf{x}_0 + \eta_{min}\mathbf{C}_0$. For $k > 0$, $\mathbf{C}_k$ is obtained by using the conjugation constraint which requires the new search direction be orthogonal to the previous search directions:

$$
\mathbf{C}_k = \mathbf{g}_k + \beta_k\mathbf{C}_{k-1} \tag{3.16}
$$

where $\mathbf{C}_{k-1}$ is the search direction in the previous step, $\mathbf{g}_k$ is the negative gradient of the

potential function

$$\mathbf{g}_k = -\nabla W(\mathbf{x}_k) \tag{3.17}$$

and

$$\beta_k = \frac{\|\mathbf{g}_k\|^2}{\|\mathbf{g}_{k-1}\|^2} = \frac{\|\nabla W(\mathbf{x}_k)\|^2}{\|\nabla W(\mathbf{x}_{k-1})\|^2} \tag{3.18}$$

Once the search direction is computed, the next position vector is determined by minimizing the potential energy function along the search direction, i.e.,

$$W_s(\eta) = W(\mathbf{x}_k + \eta \mathbf{C}_k) \tag{3.19}$$

Noted that $k < K$ since there can only be as many as K vectors in an orthogonal set in a K-dimension space. If the algorithm does not converge within K steps, the procedure is started over again by taking $\mathbf{x}_K$ as the new $\mathbf{x}_0$. The iterations continue until the convergence criterion is met.

In this work, the Powell method [63] is employed to solve the single variable minimization problem and obtain η_{min}. The Powell method approximates the actual function by using a quadratic function. The quadratic function is determined by fitting the actual function near its minimum. As most of the interatomic potential energy functions are smooth near the equilibrium position, performance of the quadratic approximation is found to be satisfactory. To determine the quadratic function, the potential function is sampled at three different locations. The first two are given by $\eta_0^{(0)} = 0$ and $\eta_1^{(0)} = \eta_0^{(0)} + \delta\eta$. A common choice of the step size is $\delta\eta = 0.5$. The third point is obtained based on the potential

energy function values at the two ends as

$$\begin{cases} \eta_2^{(0)} = \eta_0^{(0)} + 2\delta\eta & \text{if} \quad W_s(\eta_0^{(0)}) > W_s(\eta_1^{(0)}) \\ \eta_2^{(0)} = \eta_1^{(0)}, \quad \eta_1^{(0)} = \eta_0^{(0)}, \quad \eta_0^{(0)} = \eta_0^{(0)} - \delta\eta & \text{if} \quad W_s(\eta_0^{(0)}) < W_s(\eta_1^{(0)}) \end{cases} \tag{3.20}$$

The value changes made in the second case is to retain the sequence of $\eta_0^{(0)} < \eta_1^{(0)} < \eta_2^{(0)}$. Next, set $\eta_{min}^{(0)}$ to be the $\eta_i^{(0)}$, $i = 0, 1,$ or 2, whichever gives the smallest W_s. With the three η points and their corresponding W_s values, one can construct a quadratic interpolation function. At n-th iteration, the quadratic function is given by

$$f(\eta) = a_0 + a_1(\eta - \eta_0^{(n)}) + a_2(\eta - \eta_0^{(n)})(\eta - \eta_1^{(n)}) \tag{3.21}$$

where

$$\begin{aligned} a_0 &= W_s(\eta_0^{(n)}) \\ a_1 &= \frac{W_s(\eta_1^{(n)}) - W_s(\eta_0^{(n)})}{\eta_1^{(n)} - \eta_0^{(n)}} \\ a_2 &= \left[\frac{W_s(\eta_2^{(n)}) - W_s(\eta_0^{(n)})}{\eta_2^{(n)} - \eta_0^{(n)}} - \frac{W_s(\eta_1^{(n)}) - W_s(\eta_0^{(n)})}{\eta_1^{(n)} - \eta_0^{(n)}} \right] / \left(\eta_2^{(n)} - \eta_1^{(n)} \right) \end{aligned} \tag{3.22}$$

The location of the minimum of $f(\eta)$ is obtained as

$$\eta_{new}^{(n)} = \begin{cases} \dfrac{\eta_1^{(n)} + \eta_0^{(n)}}{2} - \dfrac{a_1}{2a_2} & \text{if } a_1 \le 5a_2 \left(\eta_2^{(n)} - \eta_0^{(n)} \right) \\ \dfrac{\eta_1^{(n)} + \eta_0^{(n)}}{2} - sign(a_1 a_2) \dfrac{5 \left(\eta_2^{(n)} - \eta_0^{(n)} \right)}{2} & \text{if } a_1 > 5a_2 \left(\eta_2^{(n)} - \eta_0^{(n)} \right) \end{cases} \tag{3.23}$$

Note that the second term on the right hand side of Eq. (3.23) is used to prevent $\eta_{new}^{(n)}$ from falling too far from the current interval. Once $\eta_{new}^{(n)}$ is obtained, the convergence criteria are checked. The minimum is found if both $\left| W_s(\eta_{new}^{(n)}) - W_s(\eta_{min}^{(n)}) \right| < \epsilon_f$ and $\left| \eta_{new}^{(n)} - \eta_{min}^{(n)} \right| <$

ϵ_η, where ϵ_f and ϵ_η are the termination tolerances for W_s and η, respectively. If any of the convergence criteria is not satisfied, a new iteration starts. If $W_s(\eta_{new}^{(n)}) < W_s(\eta_{min}^{(n)})$, $\eta_{min}^{(n)}$ is updated to be $\eta_{min}^{(n)} = \eta_{new}^{(n)}$ and a new set of three $\eta^{(n+1)}$ points are determined. The new set is selected from $\eta_{new}^{(n)}$ and the old set, such that it consists of $\eta_{min}^{(n)}$ and two η values that are closest to $\eta_{min}^{(n)}$. With the new η point set, the procedure from Eq. (3.21) to Eq. (3.23) is repeated to calculate $\eta_{min}^{(n+1)}$. The iterations continue until the convergence criteria are satisfied and the minimum of $W_s(\eta)$ is found.

After η_{min} is found, the new position vector is then determined as

$$\mathbf{x}_{k+1} = \mathbf{x}_k + \eta_{min}\mathbf{C}_k \tag{3.24}$$

The iterative procedure continues until the negative gradient $\|\mathbf{g}_k\| < \epsilon_g$, where ϵ_g is the global convergence tolerance. The CNT potential energy minimization procedure is summarized in Algorithm 1.

3.3 Radial breathing mode frequency

As described in Section 1, the equilibrium configuration of a CNT is directly related to its radial breathing mode (RBM) frequency. The latter can be measured experimentally and used to identify the size and type of CNTs. Several phenomenological relations have been proposed in the literature [69] . The simplest one is the inverse relation: $\omega = A/R$, where A is a fitting parameter. It was reported from different studies that the value of A is in the range of 218-248 cm^{-1} [27]. Popov et al [62] proposed a more sophisticated analytical model fitted to ab initio results to include the effect of chiral angle: $\omega_{RBM} = \frac{a_2}{R^{n_2}} + \frac{a_3}{R^{n_3}} \cos 3\theta$, where R is the tube radius, θ is the chiral angle, and a_2, n_2, a_3, n_3 are all fitting parameters. While the phenomenological relations are simple, their effectiveness

Algorithm 1 Algorithm for CNT potential energy minimization

Set the maximum global iterations Md and the global convergence tolerance ϵ_g;
Set the line search stop tolerance ϵ_f and ϵ_η;
Set the number of variables K = 5;
Calculate α_1^0, α_2^0 and α_3^0 by using Eq. (3.9);
Initialize $\mathbf{x}_0 = [r_0, r_0, \alpha_1^0, \alpha_2^0, \alpha_3^0]$;
for i = 1,2,..., Md **do**
  for k = 0,1,2,..., $K-1$ **do**
    Calculate $\mathbf{g}_k$ at $\mathbf{x}_0$ by using Eq. (3.17) along with Eqs. (3.10) to (3.15) and Eqs. (14) to (16).
    if k = 0 **then**
      $\mathbf{C}_k = \mathbf{g}_k$;
    else
      if $\|\mathbf{g}_k\| < \epsilon_g$ **then** stop;
      Calculate $\mathbf{C}_k$ from Eqs. (3.16) to (3.18);
    end if
    Initialize $n = 0$, $\boldsymbol{\eta}^{(0)} = \left[\eta_0^{(0)}, \eta_1^{(0)}, \eta_2^{(0)}\right]$
    Set $\eta_{min}^{(0)} = \eta_i^{(0)}$, $i = 0, 1,$ or 2, whichever gives the smallest W_s;
    Initialize $\eta_{new}^{(0)}$ by using Eqs. (3.22) and (3.23);
    while $\left|W_s(\eta_{new}^{(n)}) - W_s(\eta_{min}^{(n)})\right| > \epsilon_f$ or $\left|\eta_{new}^{(n)} - \eta_{min}^{(n)}\right| > \epsilon_\eta$ **do**
      if $W_s(\eta_{new}^{(n)}) < W_s(\eta_{min}^{(n)})$ **then** $\eta_{min}^{(n)} = \eta_{new}^{(n)}$;
      Set $\boldsymbol{\eta}^{(n+1)}$ from $\left\{\boldsymbol{\eta}^{(n)}, \eta_{new}^{(n)}\right\}$ such that $\boldsymbol{\eta}^{(n+1)}$ consists of $\eta_{min}^{(n)}$ and two η points closest to $\eta_{min}^{(n)}$;
      Sort η points in $\boldsymbol{\eta}^{(n+1)}$ such that $\eta_0^{(n+1)} < \eta_1^{(n+1)} < \eta_2^{(n+1)}$;
      Calculate $\eta_{new}^{(n+1)}$ by using Eqs. (3.22) and (3.23);
      n=n+1;
    end while
    Calculate new $\mathbf{x}_k$ by Eq. (3.24);
  end for
end for

depends on the form of the expression and accuracy of fitting parameters.

In this work, having obtained the equilibrium structural configurations of CNTs as described in Section 2, the RBM frequencies are further calculated using the multi-body interatomic potential energy of the carbon atoms. The primary assumption is that, when a CNT vibrates in RBM, all atoms move only in radial direction and remain on a cylindrical surface as shown in Fig. 3.3. That is, the mode coupling effect is negligible [39, 38]. Based on this assumption, the relation between bond lengths, bond angles and tube radius

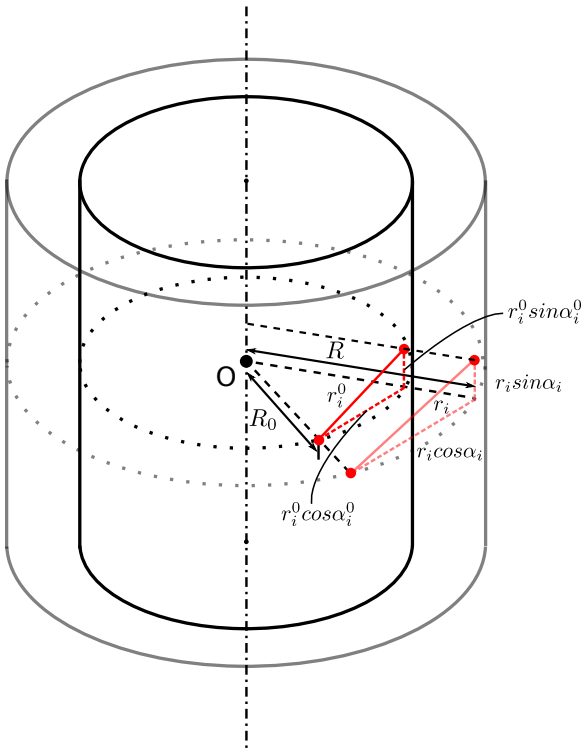

Figure 3.3: Radial breathing mode vibration of carbon nanotubes.

in RBM can be established as:

$$\frac{r_i \cos\alpha_i}{R} = \frac{l_i}{R} = \frac{l_i^0}{R} = \frac{r_i^0 \cos\alpha_i^0}{R^0} \qquad i = 1, 2, 3 \tag{3.25}$$
$$r_i \sin\alpha_i = h_i = h_i^0 = r_i^0 \sin\alpha_i^0$$

where r_i, α_i, l_i and h_i, $i = 1, 2, 3$, are defined in Section 3.1. The superscript 0 denotes the equilibrium configuration. r_i can be explicitly expressed as

$$r_i = \sqrt{(r_i^0 \cos\alpha^0)^2 \frac{R^2}{(R^0)^2} + (r_i^0 \sin\alpha^0)^2} \tag{3.26}$$

By using Eq. (3.26), Eq. (3.6) can be rewritten as

$$\begin{aligned} \cos\theta_{jk} &= \frac{R^2}{r_j r_k}\left(\frac{r_j cos\alpha_j r_k cos\alpha_k}{R^2} T_j T_k + \frac{r_j^2 r_k^2}{4R^4}\cos^2\alpha_j \cos^2\alpha_k\right) + \frac{1}{r_j r_k} r_j r_k \sin\alpha_j \sin\alpha_k \\ &= \frac{1}{r_j r_k}\left[R^2\left(S_j S_k T_j T_k + S_j^2 S_k^2/4\right) + H_j H_k\right] \end{aligned} \tag{3.27}$$

where $S_q = r_q \cos\alpha_q / R = r_q^0 \cos\alpha_q^0 / R^0$, $H_q = r_q \sin\alpha_q = r_q^0 \sin\alpha_q^0$, and

$$T_q = \sqrt{1 - \frac{r_q^2}{4R^2}\cos^2\alpha_q} = \sqrt{1 - \frac{C_q^2}{4}} \qquad q = j \ \ or \ \ k \tag{3.28}$$

Note that, S, H and T are all independent of R. Thus the 1st and 2nd order derivatives of r_i and $\cos\theta_{jk}$ with respect to R are derived as follows:

$$\begin{aligned} \frac{\partial r}{\partial R} &= \frac{1}{r}\left(\frac{r^0\cos\alpha^0}{R^0}\right)^2 R \\ \frac{\partial^2 r}{\partial R^2} &= \frac{1}{r}\left(\frac{r^0\cos\alpha^0}{R^0}\right)^2 - \frac{1}{r^3}\left(\frac{r^0\cos\alpha^0}{R^0}\right)^4 R^2 \\ \frac{\partial \cos\theta_{jk}}{\partial R} &= \frac{2RC_1}{r_j r_k} - \frac{R^2 C_1 + C_2}{r_j r_k}\left(\frac{1}{r_j}\frac{\partial r_j}{\partial R} + \frac{1}{r_k}\frac{\partial r_k}{\partial R}\right) \\ &= \frac{2RC_1}{r_j r_k} - \cos\theta_{jk}\left(\frac{1}{r_j}\frac{\partial r_j}{\partial R} + \frac{1}{r_k}\frac{\partial r_k}{\partial R}\right) \\ \frac{\partial^2 \cos\theta_{jk}}{\partial R^2} &= \frac{2C_1}{r_j r_k} - \frac{4RC_1}{r_j r_k}\left(\frac{1}{r_j}\frac{\partial r_j}{\partial R} + \frac{1}{r_k}\frac{\partial r_k}{\partial R}\right) + \cos\theta_{jk}\left(\frac{1}{r_j}\frac{\partial r_j}{\partial R} + \frac{1}{r_k}\frac{\partial r_k}{\partial R}\right)^2 \\ &\quad + \cos\theta_{jk}\left[\frac{1}{r_j^2}\left(\frac{\partial r_j}{\partial R}\right)^2 - \frac{1}{r_j}\frac{\partial^2 r_j}{\partial R^2} + \frac{1}{r_k^2}\left(\frac{\partial r_k}{\partial R}\right)^2 - \frac{1}{r_k}\frac{\partial^2 r_k}{\partial R^2}\right] \end{aligned} \tag{3.29}$$

where $C_1 = S_j S_k T_j T_k + S_j^2 S_k^2/4$ and $C_2 = H_j H_k$ both remain constant during the vibration. The 2nd order derivatives of the potential function can be obtained from the chain rule as

$$\begin{aligned}\frac{\partial^2 w_0}{\partial R^2} = &\sum_i \frac{\partial w_0}{\partial r_i}\frac{\partial^2 r_i}{\partial R^2} + \sum_{i,j}\frac{\partial^2 w_0}{\partial r_i \partial r_j}\frac{\partial r_i}{\partial R}\frac{\partial r_j}{\partial R} + 2\sum_{i,j,k}^{j\neq k}\frac{\partial^2 w_0}{\partial r_i \partial \cos\theta_{jk}}\frac{\partial r_i}{\partial R}\frac{\partial \cos\theta_{jk}}{\partial R} \\ &+ \sum_{i,j}^{i\neq j}\frac{\partial w_0}{\partial \cos\theta_{ij}}\frac{\partial^2 \cos\theta_{jk}}{\partial R^2} + \sum_{i,j,k,l}^{i\neq j;k\neq l}\frac{\partial^2 w_0}{\partial \cos\theta_{ij}\partial \cos\theta_{kl}}\frac{\partial \cos\theta_{ij}}{\partial R}\frac{\partial \cos\theta_{kl}}{\partial R}\end{aligned} \tag{3.30}$$

where w_0 is the potential energy per unit cell, and i, j, k, l =1,2 or 3. The RBM frequency is given by:

$$f_{RBM} = \frac{\omega_{RBM}}{2\pi c} = \frac{1}{2\pi c}\sqrt{\frac{k}{m}} \tag{3.31}$$

where m is the mass of carbon atom, $k = \dfrac{\partial^2 w_o}{\partial R^2}|_{R=R_0}$, and c is the speed of light.

3.4 Results and Discussion

To demonstrate the performance of the model, the semi-analytical approach is applied to the reactive empirical bond order (REBO) potential [11] to calculate the equilibrium configuration and RBM frequency of various CNTs. The REBO potential has been widely used in molecular dynamics (MD) and lattice dynamics (LD) simulations of CNTs. It should be noted that, while the detailed formulation for the REBO potential is presented in Appendix B, the application of the method to other C-C interatomic potentials is straightforward by using the approach and following the steps listed in Algorithm 1.

3.4.1 Radius of CNTs

In this section, the radii of a set of CNTs with different chiralities are computed by using the semi-analytical model. For the purpose of model validation, the computed results are compared with those obtained from MD simulations. The MD simulations are preformed using the LAMMPS package. The REBO potential with the parameters given in Table 5 (Appendix B) is adopted in the semi-analytical calculation and MD simulations. In the test cases, the CNT chiralities varies from (4,0) to (8,4). In MD simulations, the length of the CNTs is set to be around 20 nm. It is verified that further increasing the length does not change the results. The MD simulation box size is set to be 20 nm $\times$ 20 nm in the transverse (cross-sectional) directions and 40 nm in the longitudinal direction with free boundary conditions applied. The total linear momentum and angular momentum are fixed to be zero. With a time step of 0.2 fs, the system is initialized at 5 K and then the temperature is reduced to 0.01 K under the NVT ensemble within 300 k time steps. A drag value of 0.5 is applied to increase damping. The purpose of this drag value is to damp unwanted pressure oscillation when applying a Nose/Hoover thermostat. The tube radius is calculated as the average distance between carbon atoms and the tube axis. Bond angles, bond lengths and the radii are averaged on atoms within 20% length at the tube center to reduce influence of the free ends.

Bond length, bond angle and radius results of the CNTs obtained by using the semi-analytical method and MD simulations are compared in Tables 3.1-3.3. It is clear that the results obtained from the two methods match very well. The maximum difference is less than 0.2%. Results show that the C-C bond lengths increase as the radius decreases, and the difference between the bond lengths r_1, r_2 and r_3 increases as well. For the smallest (4,0) nanotube, the largest bond length is 1.451 Å, which is 2% larger than the bond length in graphene, 1.420 Å. The variation of bond lengths is due to the change of bond angles.

Rolling a graphene sheet into a tube makes the angles between bonds smaller than $2\pi/3$, which increases the potential energy. This excess energy is then partially relaxed by an expansion of the atomic lattice structure, leading to elongation of the bonds. Therefore, the smaller the radius, the smaller the angles, and the larger the expansion. This conclusion is consistent with previous observations reported in the literature [70].

Table 4 further compares the radius results with those obtained from the simple rolling model and two different ab initio calculations. It is shown that the semi-analytical model with REBO potential gives nearly identical results to the MD simulations, but with much less computational cost. The error of the simple rolling model is obvious. As shown on Fig. 3.4, the relative difference between the relaxed radius and the simple rolling radius R_0 increases as the radius decreases. The results indicate that the simple rolling model is inappropriate in determining the equilibrium configuration of CNTs, especially for nanotubes with small radius. For example, for the (4,0) nanotube, we obtain a radius that is 9% greater than R_0. Furthermore, it is shown that the chirality play an important role on the results. The armchair CNTs show smaller relative errors than the zigzag CNTs. For other chiral nanotubes, the radius error resides within the zone between the zigzag and armchair CNTs. It is observed that the orientation of the unit cells determines how the bond angles are affected by rolling, which results in different radius expansion for different chiralities. It should be noted that there is a small difference between the semi-analytical model and ab initio results. This is due to the difference between the REBO potential employed in the semi-analytical model and the electron density functionals used in the ab initio calculations.

Table 3.1: Bond lengths, bond angles and radius of zigzag CNTs

Zigzag (N,0)	Method	Bond lengths(Å)			Bond Angles(degree)			Radius(Å)
		r_1	r_2	r_3	θ_{i12}	θ_{i13}	θ_{i23}	
(4,0)	This work	1.451	1.439	1.451	115.970	112.316	115.975	1.705
	MD	1.450	1.440	1.450	115.934	112.418	115.934	1.705
(5,0)	This work	1.438	1.432	1.438	117.398	115.209	117.400	2.065
	MD	1.437	1.432	1.437	117.360	115.326	117.360	2.066
(6,0)	This work	1.432	1.428	1.432	118.228	116.650	118.231	2.437
	MD	1.431	1.428	1.431	118.187	116.788	118.186	2.438
(7,0)	This work	1.429	1.426	1.429	118.735	117.486	118.739	2.815
	MD	1.428	1.426	1.428	118.692	117.638	118.692	2.816
(8,0)	This work	1.427	1.424	1.427	119.062	118.026	119.066	3.196
	MD	1.426	1.425	1.426	119.017	118.186	119.017	3.197

Table 3.2: Bond lengths, bond angles and radius of armchair CNTs

Armchair (N,N)	Method	Bond lengths(Å)			Bond Angles(degree)			Radius(Å)
		r_1	r_2	r_3	θ_{i12}	θ_{i13}	θ_{i23}	
(3,3)	This work	1.437	1.432	1.432	116.314	116.315	118.421	2.104
	MD	1.437	1.432	1.432	116.350	116.350	118.389	2.105
(4,4)	This work	1.430	1.427	1.427	117.852	117.852	119.247	2.762
	MD	1.429	1.427	1.427	117.896	117.895	119.206	2.764
(5,5)	This work	1.426	1.424	1.424	118.572	118.573	119.618	3.429
	MD	1.426	1.424	1.424	118.619	118.619	119.574	3.431
(6,6)	This work	1.425	1.423	1.423	118.975	118.975	119.799	4.099
	MD	1.424	1.423	1.423	119.025	119.025	119.751	4.102
(7,7)	This work	1.424	1.422	1.422	119.226	119.228	119.891	4.772
	MD	1.423	1.422	1.422	119.278	119.278	119.841	4.775

3.4.2 RBM frequency of CNTs

Having obtained the equilibrium structure of the CNTs, the RBM frequencies are calculated as described in Section 3. Figure 3.5 shows the RBM frequencies of a variety of CNTs calculated by using the semi-analytical, simple rolling, ab intio approaches as well as a fitted analytical model [62]. For the sake of clarity, the calculated data points for narrow

Table 3.3: Bond lengths, bond angles and radius of Chiral CNTs

Chirality (N,M)	Method	Bond lengths(Å)			Bond Angles(degree)			Radius(Å)
		r_1	r_2	r_3	θ_{i12}	θ_{i13}	θ_{i23}	
(3,2)	This work	1.446	1.438	1.439	115.304	114.348	117.611	1.798
	MD	1.445	1.437	1.439	115.345	114.391	117.585	1.799
(4,1)	This work	1.443	1.435	1.439	116.425	114.396	117.358	1.903
	MD	1.443	1.435	1.439	116.446	114.461	117.346	1.906
(4,2)	This work	1.437	1.431	1.433	116.946	116.011	118.323	2.150
	MD	1.436	1.431	1.433	116.973	116.082	118.297	2.153
(5,1)	This work	1.435	1.430	1.433	117.634	116.182	118.201	2.270
	MD	1.434	1.429	1.433	117.626	116.271	118.197	2.274
(4,3)	This work	1.432	1.428	1.429	117.433	117.109	118.904	2.442
	MD	1.432	1.428	1.429	117.462	117.171	118.870	2.444
(5,2)	This work	1.432	1.428	1.429	117.881	117.037	118.804	2.514
	MD	1.431	1.428	1.429	117.887	117.132	118.781	2.517
(6,1)	This work	1.430	1.427	1.429	118.325	117.191	118.747	2.643
	MD	1.430	1.427	1.429	118.326	117.288	118.721	2.646

Table 3.4: Comparison of radius results obtained from different methods

(N,M)	Simple rolling R_0 (Eq.(3.1))	This work	MD	ab initio 1 [38]	ab initio 2 [70]
(4,0)	1.566	1.705	1.705	1.671	
(3,2)	1.706	1.798	1.799	1.766	
(3,3)	2.034	2.104	2.105	2.088	
(6,1)	2.567	2.643	2.646	2.608	
(4,4)	2.712	2.762	2.764	2.745	2.794
(5,5)	3.390	3.429	3.431	3.411	3.463
(10,0)	3.914	3.965	3.967	3.926	3.979
(8,4)	4.143	4.178	4.182		4.211

CNTs are enlarged and displayed on the right side of Fig. 3.5. The REBO potential with the parameters given in Appendix B is used in the semi-analytical approach. As shown in Fig. 3.5, significant differences in the results are observed for narrow CNTs with radius smaller than 2.6 Å. The difference between the semi-analytical and simple rolling approaches is largely due to the inaccurate geometry properties (radius, bond lengths and angles) given

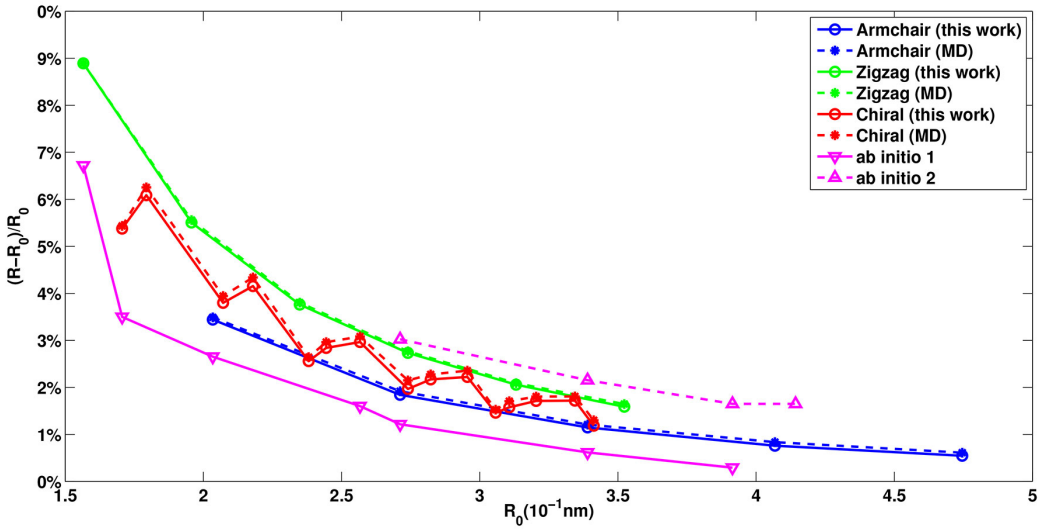

Figure 3.4: Percentage difference between the simple rolling radius R_0 and the radii calculated from the semi-analytical, MD and ab initio models.

by the simple rolling model. The error in these geometry properties is further enlarged in the RBM frequency results due to the high sensitivity of the force constants (second derivatives of the interatomic potential) to the tube geometry. Figure 3.5 (right) shows that such error in the simple rolling model results is more than 20% for the (4,0) CNT. The difference between the semi-analytical and ab initio results stems from the difference in their physical description of the interatomic interactions (i.e., interatomic potentials vs electron density functionals). It should be noted that the results from "ab initio 3" [39] are based on tube geometries obtained from the simple rolling model. Finally, Fig. 3.5 shows that the differences in the results from the different models become negligible for tubes with radius larger than 4 Å.

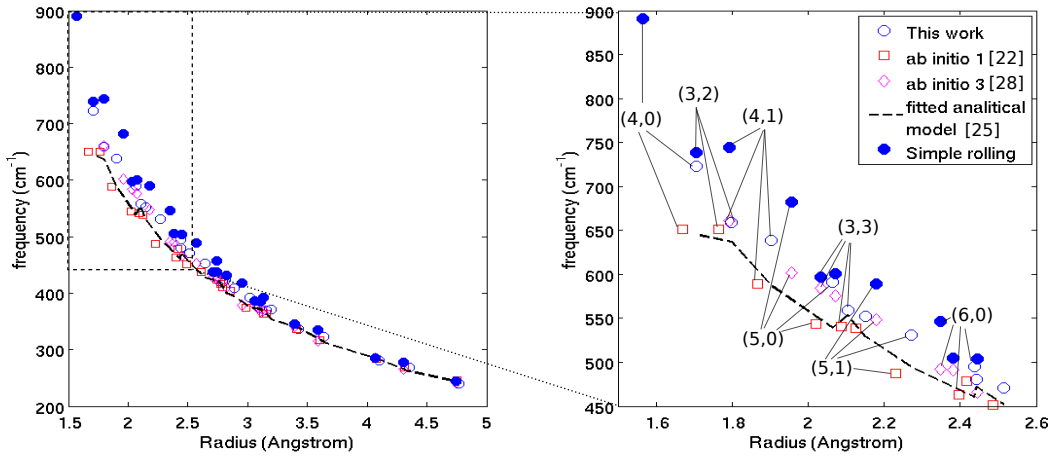

Figure 3.5: RBM frequencies of CNTs. The two ab initio results (ab initio 1 [38] and 3 [39]) are obtained from the literature.

3.5 Summary

In this chapter, a semi-analytical unconstrained energy optimization model with 5 independent variables for determining the equilibrium configuration of single wall CNTs is presented. For demonstration purpose, the semi-analytical model is applied to the REBO potential for the calculation of the radii of various CNTs. It is shown that, with a negligible computational cost, the semi-analytical model is able to reproduce the results obtained from MD simulations and match well with the results obtained from ab initio calculations. Furthermore, the semi-analytical approach is extended for the calculation of the RBM frequencies of CNTs. From the radius and RBM frequency results, it is shown that the simple rolling model is inappropriate in determining the equilibrium configuration of CNTs, especially for nanotubes with small radius. While the RBM frequency results obtained from the semi-analytical approach match reasonably well the ab inito results, differences are observed for CNTs with radius smaller than 2.6 Å. The discrepancy is due to the different underlying physical models of the two approaches. As the semi-analytical approach is independent of the potential energy functions, more accurate results may be obtained with

other improved potential energy functions.

Chapter 4

The potential-based non-local and local linear plate models of single layer graphene structures

In this chapter, we investigate the performance of the local and non-local Kirchoff plate for static and modal analysis of SLGS. For error estimate, an atomic lattice model based the 2nd generation REBO potential is implemented and used for all calculations and the results are used as reference results. To avoid plate thickness problem, we use the interatomic potential to calculate the bending rigidity in the plate models. In our analysis, it is found that the boundary location and boundary conditions are important for the accuracy of the results. This is especially true for small SLGS. Based on extensive numerical experiments, we propose a simple correction of the boundary location and show that the error is largely reduced in all cases. Next, we investigate the choice of e_0a values in the modal analysis of SLGS. The modal frequency spectrum of the first 50 modes are calculated using the local plate model and the non-local plate model with a set of different e_0a. The effect of e_0a is studied and the effectiveness of the non-local model is discussed. Conclusions are

given at the end.

4.1 Mechanics of Single Layer Graphene

In a relaxed perfect graphene lattice, each unit cell contains two carbon atoms, as shown in Fig. 4.1. The unit cells are labeled by L and the two carbon atoms in a unit cell are indexed by $\kappa = 1, 2$. Therefore, the notation of atom $L\kappa$ denotes the atom κ in unit cell L.

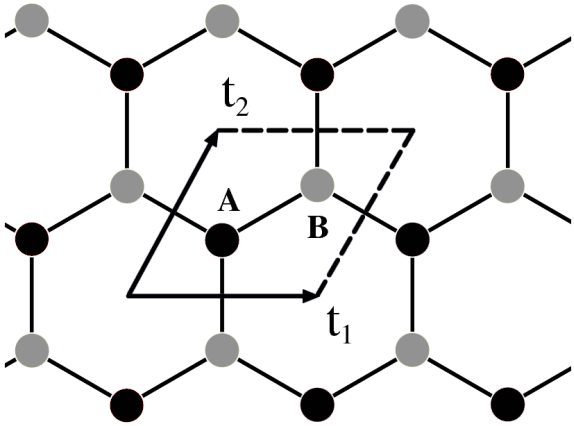

Figure 4.1: Unit cell of graphene lattice. Black and gray circles indicate the atoms of two Bravais lattices. t_1 and t_2 are basis vectors.

Under the harmonic approximation, the total potential energy W of a pristine graphene sheet close to its equilibrium configuration can be written as

$$W = W_0 + \tfrac{1}{2} \sum_{\substack{L,\kappa,\alpha \\ L',\kappa',\beta}} \phi_{\alpha\beta}(L\kappa, L'\kappa') u_\alpha(L\kappa) u_\beta(L'\kappa'), \qquad \alpha, \beta = 1, 2, 3 \quad (4.1)$$

where W_0 is the equilibrium potential energy, α and β denote the axial directions in the Cartesian coordinate system, $u_\alpha(L\kappa)$ is the displacement of atom $L\kappa$ along direction α from its equilibrium position, and $\phi_{\alpha\beta}(L\kappa, L'\kappa')$ is a force constant between atoms $L\kappa$ and

$L'\kappa'$, which is defined as

$$\phi_{\alpha\beta}(L\kappa, L'\kappa') = \left.\frac{\partial^2 W}{\partial u_\alpha(L\kappa)\partial u_\beta(L'\kappa')}\right|_{u_\alpha(L\kappa)=u_\beta(L'\kappa')=0}, \qquad \alpha,\beta = 1,2,3 \tag{4.2}$$

From Eqs. (4.1,4.2), the force acting on atom $L\kappa$ along direction α can be expressed as

$$f_\alpha(L\kappa) = -\frac{\partial W}{\partial u_\alpha(L\kappa)} = -\sum_{L',\kappa',\beta} \phi_{\alpha\beta}(L\kappa, L'\kappa')u_\beta(L'\kappa') \tag{4.3}$$

For any pair of atoms $L\kappa$ and $L'\kappa'$, $\phi_{\alpha\beta}(L\kappa, L'\kappa')$ forms a 3-by-3 matrix. For a graphene lattice of N atoms, Eq. (4.3) can be assembled and written in matrix form as

$$\mathbf{f}_{3N\times 1} = \mathbf{\Phi}_{3N\times 3N}\mathbf{u}_{3N\times 1} \tag{4.4}$$

where $\mathbf{\Phi}$ is the force constant matrix, $\mathbf{f}$ is the force vector and $\mathbf{u}$ is the atom displacement vector. For the graphene lattice, Eq. (4.4) is the linear equation of equilibrium based on the harmonic approximation. The corresponding equation of motion can be written as

$$\mathbf{M\ddot{u}} + \mathbf{\Phi u} = \mathbf{f} \tag{4.5}$$

where $\mathbf{M} = m_c\mathbf{I}_{3N\times 3N}$, m_c is the mass of carbon atom and $\mathbf{I}$ is an identity matrix. In this work, we employ a modified REBO potential for graphene. The modified REBO potential is given by [11]

$$W = \frac{1}{2}\sum_{i,j,i\neq j} V_{ij} = \frac{1}{2}\sum_{i,j,i\neq j}\left[V_R(r_{ij}) - \bar{b}_{ij}V_A(r_{ij})\right] \tag{4.6}$$

where

$$
\begin{aligned}
V_R(r) &= \left(1+\frac{Q}{r}\right) Ae^{-\alpha r} f_c(r) \\
V_A(r) &= \sum_{n=1}^{3} B_n e^{-\beta_n r} f_c(r) \\
b_{ij} &= \left[1+\sum_{k}^{k\neq j} G(\cos\theta_{ijk}) f_c(r_{ik})\right]^{-\frac{1}{2}} \\
\bar{b}_{ij} &= \frac{1}{2}(b_{ij}+b_{ji})
\end{aligned}
\tag{4.7}
$$

and

$$
f_c(r) = \begin{cases} 1 & r < R_1, \\ \frac{1}{2}\left\{1+\cos\left[\frac{\pi(r-R_1)}{R_2-R_1}\right]\right\} & R_1 \le r \le R_2, \\ 0 & r > R_2, \end{cases}
$$

$$
G = \begin{cases} 0.27186 - 0.48922\cos\theta - 0.43286\cos^2\theta - 0.56140\cos^3\theta \\ \qquad + 1.2711\cos^4\theta - 0.037931\cos^5\theta & \theta < 109.47^\circ, \\ 0.69669 + 5.5444\cos\theta + 23.432\cos^2\theta + 55.948\cos^3\theta \\ \qquad + 69.876\cos^4\theta + 35.312\cos^5\theta & 109.47^\circ \le \theta \le 120^\circ, \\ 0.00260 - 1.0980\cos\theta - 4.3460\cos^2\theta \\ \qquad - 6.8300\cos^3\theta - 4.9280\cos^4\theta - 1.3424\cos^5\theta & \theta > 120^\circ, \end{cases}
\tag{4.8}
$$

Note that, in the REBO potential, for simplicity, instead of lattice atom notation $L\kappa, L'\kappa', ...$, single labels $i, j, k...$ are used as atom indices. V_{ij} and r_{ij} are the bond energy and distance between atoms i and j, respectively. θ_{ijk} is the angle between the bond of atoms i and j and the bond of atoms i and k. Differentiating the bond energy with respect to the atomic

displacements, we have

$$
\begin{aligned}
\frac{\partial V_{ij}}{\partial u_{m\alpha}} &= \frac{dV_R}{dr_{ij}}\frac{\partial r_{ij}}{\partial u_{m\alpha}} - \bar{b}_{ij}\frac{dV_A}{dr_{ij}}\frac{\partial r_{ij}}{\partial u_{m\alpha}} - V_A\sum_{k}^{k\neq j}\left(\frac{\partial \bar{b}_{ij}}{\partial r_{ik}}\frac{\partial r_{ik}}{\partial u_{m\alpha}} - \frac{\partial \bar{b}_{ij}}{\partial \cos_{ijk}}\frac{\partial \cos_{ijk}}{\partial u_{m\alpha}}\right) \\
\frac{\partial^2 V_{ij}}{\partial u_{m\alpha}\partial u_{n\beta}} &= \frac{dV_R}{dr_{ij}}\frac{\partial^2 r_{ij}}{\partial u_{m\alpha}\partial u_{n\beta}} + \frac{d^2V_R}{dr_{ij}^2}\frac{\partial r_{ij}}{\partial u_{m\alpha}}\frac{\partial r_{ij}}{\partial u_{n\beta}} - \bar{b}_{ij}\frac{dV_A}{dr_{ij}}\frac{\partial^2 r_{ij}}{\partial u_{m\alpha}\partial u_{n\beta}} \\
&\quad - \bar{b}_{ij}\frac{d^2V_A}{dr_{ij}^2}\frac{\partial r_{ij}}{\partial u_{m\alpha}}\frac{\partial r_{ij}}{\partial u_{n\beta}} - \frac{dV_A}{dr_{ij}}\frac{\partial r_{ij}}{\partial u_{m\alpha}}\sum_{k}^{k\neq j}\left(\frac{\partial \bar{b}_{ij}}{\partial r_{ik}}\frac{\partial r_{ik}}{\partial u_{n\beta}} - \frac{\partial \bar{b}_{ij}}{\partial \cos_{ijk}}\frac{\partial \cos_{ijk}}{\partial u_{n\beta}}\right) \\
&\quad - \sum_{k}^{k\neq j}\left(\frac{\partial \bar{b}_{ij}}{\partial r_{ik}}\frac{\partial r_{ik}}{\partial u_{m\alpha}} - \frac{\partial \bar{b}_{ij}}{\partial \cos_{ijk}}\frac{\partial \cos_{ijk}}{\partial u_{m\alpha}}\right)\frac{dV_A}{dr_{ij}}\frac{\partial r_{ij}}{\partial u_{n\beta}} \\
&\quad - V_A\sum_{k}^{k\neq j}\left(\frac{\partial \bar{b}_{ij}}{\partial r_{ik}}\frac{\partial^2 r_{ik}}{\partial u_{m\alpha}\partial u_{n\beta}} - \frac{\partial \bar{b}_{ij}}{\partial \cos_{ijk}}\frac{\partial^2 \cos_{ijk}}{\partial u_{m\alpha}\partial u_{n\beta}}\right) \\
&\quad - V_A\sum_{k,k'}^{k,k'\neq j}\left(\frac{\partial^2 \bar{b}_{ij}}{\partial r_{ik}\partial r_{ik'}}\frac{\partial r_{ik}}{\partial u_{m\alpha}}\frac{\partial r_{ik'}}{\partial u_{n\beta}} - \frac{\partial^2 \bar{b}_{ij}}{\partial r_{ik}\partial \cos_{ijk'}}\frac{\partial r_{ik}}{\partial u_{m\alpha}}\frac{\partial \cos_{ijk'}}{\partial u_{n\beta}}\right. \\
&\quad \left. - \frac{\partial^2 \bar{b}_{ij}}{\partial r_{ik}\partial \cos_{ijk'}}\frac{\partial \cos_{ijk'}}{\partial u_{m\alpha}}\frac{\partial r_{ik}}{\partial u_{n\beta}} - \frac{\partial^2 \bar{b}_{ij}}{\partial \cos_{ijk}\partial \cos_{ijk'}}\frac{\partial \cos_{ijk}}{\partial u_{m\alpha}}\frac{\partial \cos_{ijk'}}{\partial u_{n\beta}}\right)
\end{aligned}
\tag{4.9}
$$

Here the subscripts m and n are atom indices, α and β are the axial directions as defined in Eq. (4.1). The force constants can be obtained from:

$$
\phi_{\alpha\beta}(m,n) = \frac{\partial^2 W}{\partial u_{m\alpha}\partial u_{n\beta}} = \frac{1}{2}\sum_{i,j}\frac{\partial^2 V_{ij}}{\partial u_{m\alpha}\partial u_{n\beta}} \tag{4.10}
$$

For the REBO potential without dihedral angle terms, each atom only interacts with its 1st and 2nd neighbors. For any atom i, $\phi_{\alpha\beta}(i,j)$ is zero if atom j is beyond the 2nd neighbors of atom i. Since there are only 2 Bravais lattices in a perfect SLGS, force constants for the two types of atoms in a unit cell represent the force constants of all atoms in the lattice. Considering the out-of-plane deformation, it can be shown form Eq. (4.10) that $\phi_{\alpha 3}(i,j) = \phi_{3\alpha}(i,j) = 0$, $\alpha = 1, 2$, which means the in-plane deformation is independent from the out-of-plane deformation. In addition, $\phi_{33}(i,j) = \phi_1 = -473.63$ eV/nm^2 for $\{j \,|j \in$ first

neighbors of i } and $\phi_{33}(i,j) = \phi_2 = 78.938$ eV/nm^2 for $\{j \,|j \in$ second neighbors of i }. This is true for both types of atom i. It can then be shown that $\phi_{33}(i,i) = -3\phi_1 - 6\phi_2 = 947.262$ eV/nm^2. This characteristics of the interactomic potential is also discussed in Ref. [95]. The details of the calculation of the force constants are presented in the Appendix.

4.2 Local and Non-local Plate Models for SLGS

4.2.1 Kirchhoff-Love (local) plate model for SLGS

The well-known Kirchhoff-Love model for isotropic homogeneous plates is summarized here for the sake of completeness. Consider a thin plate lies in the xy-plane and is subjected to out-of-plane displacement w only. That is, the deformation of the plate is pure bending. From the Kirchhoff-Love plate theory, the equilibrium equation of bending moments is [79]:

$$\frac{\partial^2 M_x}{\partial x^2} + \frac{\partial^2 M_y}{\partial y^2} - 2\frac{\partial^2 M_{xy}}{\partial x \partial y} = -q + \rho h \frac{\partial^2 w}{\partial t^2} \tag{4.11}$$

where M_x, M_y and M_{xy} are bending moments, q is the intensity of distributed transverse shear loading, and h is the plate thickness. For pure bending, the moment-curvature relations can be expressed as [79]:

$$\begin{aligned} M_x &= -D(\frac{\partial^2 w}{\partial x^2} + \nu \frac{\partial^2 w}{\partial y^2}) = D(\kappa_{xx} + \nu \kappa_{yy}) \\ M_y &= -D(\frac{\partial^2 w}{\partial y^2} + \nu \frac{\partial^2 w}{\partial x^2}) = D(\kappa_{yy} + \nu \kappa_{xx}) \\ M_{xy} &= -\frac{(1-\nu)}{2} D \frac{\partial^2 w}{\partial x \partial y} = \frac{(1-\nu)}{2} D \kappa_{xy} \end{aligned} \tag{4.12}$$

where D is the bending rigidity, κ_{xx} and κ_{yy} are the curvatures in the x- and y-directions, respectively, and κ_{xy} is the twist. For isotropic thin plates, the bending rigidity can be written as

$$D = \frac{Eh^3}{12(1-\nu^2)} \tag{4.13}$$

where E is Young's modulus and ν is Poisson's ratio. Substituting Eq. (4.12) into Eq. (4.11), we obtain the governing equation for plate bending as

$$-D\left(\frac{\partial^4 w}{\partial x^4} + 2\frac{\partial^4 w}{\partial x^2 \partial y^2} + \frac{\partial^4 w}{\partial y^4}\right) + q - \rho h \frac{\partial^2 w}{\partial t^2} = 0 \tag{4.14}$$

It is shown in Eq. (4.14) that, for a given material, the bending rigidity D must be determined in order to solve the plate bending equation. Following the conventional definition, Eq. (4.13), Young's modulus, Poisson's ratio and plate thickness are required. However, unlike traditional continuous materials, graphene is a single layer atom lattice structure with no intuitive thickness. In addition, the out-of-plane bending moments of graphene come from the interatomic forces arise from position variation of the atoms, not the integral of stresses along the plate thickness in the classical plate theory. For this reason, we adopt the moment-curvature relations proposed by Belytschko [7] and Huang [31] which were derived based on the assumption that the mechanical behavior of graphene lattice is governed by a multibody interatomic potential. The relations are given by [31]

$$\begin{aligned} M_x + M_y &= \frac{\sqrt{3}}{2}\left(\frac{\partial V_{ij}}{\partial \cos\theta_{ijk}}\right)_0 (\kappa_{xx} + \kappa_{yy}) \\ M_x - M_y &= 0, \qquad\qquad M_{xy} = 0 \end{aligned} \tag{4.15}$$

where $V_{ij} = V(r_{ij}, \sum_k (\cos\theta_{ijk}))$ is the potential energy of the atomic bond connecting atoms i and j as shown in Eq. (4.6). Here atoms i and j can be any pair of neighboring

atoms and atom k can be any neighboring atoms of atom j other than atom i. The subscript 0 denotes the equilibrium state. Substituting Eq. (4.15) into Eq. (4.11) and then comparing to Eq. (4.14), we obtain the bending rigidity of SLGS as

$$D = \frac{\sqrt{3}}{4}\left(\frac{\partial V_{ij}}{\partial \cos\theta_{ijk}}\right)_0 \tag{4.16}$$

4.2.1.1 Non-local plate model for SLGS

Eringen first proposed the non-local elasticity theory to solve lattice surface wave problems [18]. As stated in Chapter 2, the mathematical expression of non-local stress-strain relation is given by [18]

$$\boldsymbol{\sigma}(\mathbf{x}) = \int_\Omega \alpha(|\mathbf{x}' - \mathbf{x}|, \tau)\mathbf{C} : \boldsymbol{\epsilon}(\mathbf{x}')d\Omega(\mathbf{x}') \tag{4.17}$$

When $\alpha(|\mathbf{x}' - \mathbf{x}|, \tau)$ is chosen to be the Green's function of a linear operator $\mathscr{L}$, it can be shown that Eq. (4.17) can be rewritten as

$$\mathscr{L}\boldsymbol{\sigma} = \mathbf{C} : \boldsymbol{\epsilon} \tag{4.18}$$

In this work, we pick α to be

$$\alpha(|\mathbf{x}|, \tau) = (2\pi l^2\tau^2)^{-1}K_0(\mathbf{x}\cdot\mathbf{x}/l\tau) \tag{4.19}$$

where K_0 is the zeroth order modified Bessel function. Then we have $\mathscr{L} = 1 - \tau^2 l^2\nabla^2 = 1 - (e_0 a)^2\nabla^2$ where ∇^2 is the Laplacian operator. Substituting $\mathscr{L}$ into Eq. (4.18), we have [18]

$$\left(1 - (e_0 a)^2\nabla^2\right)\boldsymbol{\sigma} = \mathbf{C} : \boldsymbol{\epsilon} \tag{4.20}$$

By using Eq. (4.20), we can obtain the non-local moment-curvature relations as

$$\begin{aligned}\left(1-(e_0a)^2\nabla^2\right)M_x &= D(\kappa_{xx}+\nu\kappa_{yy})\\ \left(1-(e_0a)^2\nabla^2\right)M_y &= D(\kappa_{yy}+\nu\kappa_{xx})\\ \left(1-(e_0a)^2\nabla^2\right)M_{xy} &= \frac{(1-\nu)}{2}D\kappa_{xy}\end{aligned} \tag{4.21}$$

Replacing Eq. (4.12) with Eq. (4.21), the governing equation of non-local pure bending plate model is obtained as [5]

$$-D\left(\frac{\partial^4 w}{\partial x^4}+2\frac{\partial^4 w}{\partial x^2\partial y^2}+\frac{\partial^4 w}{\partial y^4}\right)+(1-(e_0a)^2\nabla^2)(q-\rho h\frac{\partial^2 w}{\partial t^2})=0 \tag{4.22}$$

Note that, if $q=0$ or q is a function such that $\nabla^2 q=0$, the only difference between the original (local) and non-local plate equations, Eq. (4.22) and Eq. (4.14), respectively, is the non-local correction of the inertia term $\rho h\frac{\partial^2 w}{\partial t^2}$, which implies that there is no non-local correction in predicting the static behavior in this case. In addition, when $e_0a=0$, Eq. (4.22) reduces to Eq. (4.14), the local model is recovered. It also worth noting that, in comparison to Arash's equation [5], the h^2 inertia terms are removed and the h term is kept for SLGS. This is natural, since ρh is still important in graphene as the averaged mass density per unit area. However, there is no rotational inertia along graphene's thickness due to its single atom layer structure.

4.2.1.2 Finite element formulation

By using the Galerkin weighted residual method, finite element formulation of the non-local Kirchoff plate model can be obtained straightforwardly [5]. The weak form of

Eq. (4.22) is obtained as

$$\int_{\Omega}\left[-D\left(\frac{\partial^4 w}{\partial x^4}+2\frac{\partial^4 w}{\partial x^2\partial y^2}+\frac{\partial^4 w}{\partial y^4}\right)+(1-(e_0a)^2\nabla^2)(q-\rho h\frac{\partial^2 w}{\partial t^2})\right]\delta w d\Omega=0 \quad (4.23)$$

Note that, the non-local finite element model reduces to the local one when $e_0a=0$. As the Kirchhoff plate model requires C_1 continuity of the displacement w and its variation δw across the elements, a 4-node Bogner-Fox-Schmidt quadrilateral element is employed. Each node of the element has 4 degrees of freedom: w, $\frac{\partial w}{\partial x}$, $\frac{\partial w}{\partial y}$, and $\frac{\partial^2 w}{\partial x\partial y}$. The Hermit-type shape functions of the master element are given by:

$$\begin{aligned}
w: &\quad N_a(\xi,\eta)=1/16(\xi+\xi_a)^2(\xi\xi_a-2)(\eta+\eta_a)^2(\eta\eta_a-2) &\quad a=1,2,3,4\\
\frac{\partial w}{\partial \xi}: &\quad \hat{N}_a(\xi,\eta)=-1/16\xi_a(\xi+\xi_a)^2(\xi\xi_a-1)(\eta+\eta_a)^2(\eta\eta_a-2) &\quad a=1,2,3,4\\
\frac{\partial w}{\partial \eta}: &\quad \tilde{N}_a(\xi,\eta)=-1/16\eta_a(\xi+\xi_a)^2(\xi\xi_a-2)(\eta+\eta_a)^2(\eta\eta_a-1) &\quad a=1,2,3,4\\
\frac{\partial^2 w}{\partial \xi\partial \eta}: &\quad \overline{N}_a(\xi,\eta)=1/16\xi_a\eta_a(\xi+\xi_a)^2(\xi\xi_a-1)(\eta+\eta_a)^2(\eta\eta_a-1) &\quad a=1,2,3,4
\end{aligned} \quad (4.24)$$

where ξ_a, η_a are coordinates of node a in the master element. The element stiffness and mass matrices can be written as

$$\mathbf{K^e} = \int_{\Omega_e}\mathbf{B^e}^T\mathbf{D}\mathbf{B^e}d\Omega_e \quad (4.25)$$

$$\mathbf{M^e} = \int_{\Omega_e}\left(\mathbf{N^e}^T\rho h\mathbf{N^e}+(e_0a)^2\mathbf{N_x^e}^T\mathbf{I_0}\mathbf{N_x^e}\right)d\Omega_e \quad (4.26)$$

where$\mathbf{N^e} = \begin{bmatrix} \mathbf{N} & \hat{\mathbf{N}} & \tilde{\mathbf{N}} & \overline{\mathbf{N}} \end{bmatrix}$ is a 1×16 shape function vector with $\mathbf{N} = \begin{bmatrix} N_1 & N_2 & N_3 & N_4 \end{bmatrix}$, $\hat{\mathbf{N}} = \begin{bmatrix} \hat{N}_1 & \hat{N}_2 & \hat{N}_3 & \hat{N}_4 \end{bmatrix}$ and so on, and

$$\mathbf{N_x^e} = \begin{bmatrix} \dfrac{\partial \mathbf{N^e}}{\partial x} \\ \dfrac{\partial \mathbf{N^e}}{\partial y} \end{bmatrix}, \qquad \mathbf{B^e} = \begin{bmatrix} \dfrac{\partial^2 \mathbf{N^e}}{\partial x^2} \\ \dfrac{\partial^2 \mathbf{N^e}}{\partial x \partial y} \\ \dfrac{\partial^2 \mathbf{N^e}}{\partial y^2} \end{bmatrix}, \tag{4.27}$$

$$\mathbf{D} = \begin{bmatrix} D & 0 & 0 \\ 0 & 2D & 0 \\ 0 & 0 & D \end{bmatrix}, \qquad \mathbf{I_0} = \begin{bmatrix} \rho h & 0 \\ 0 & \rho h \end{bmatrix} \tag{4.28}$$

4.2.1.3 Boundary and boundary condition corrections for SLGS

In addition to the constitutive relations, the definition of graphene plate's geometry has a significant effect on the accuracy of the numerical results. Many numerical calculations in the literature use integers to define graphene sizes, e.g., "a 10 nm by 10 nm graphene sheet". Given the lattice nature of graphene, however, this integer size usually serves as a cut-off limit in atomic models (referred to as "cut-off size"), which means only the atoms residing within this limit are free to move. Due to the discrete atomic spacing, an integer value such as 10 nm is not sufficiently accurate to be applied in plate models of graphene. For example, a 10.2 nm $\times$ 10.2 nm square cuts out the same group of atoms as a 10 nm$\times$10 nm square does. Yet, a 10.2 nm $\times$ 10.2 nm plate is appreciably more flexible than a 10 nm$\times$10 nm one. This effect becomes more significant when the graphene sheet becomes smaller. In order to be consistent with the atomic lattice model, we define the "real" geometry of a graphene plate using "boundary atoms". For a clamped edge, an atom is defined as

a boundary atom when itself is fixed, but at least one of its first neighboring atoms is movable. For a free edge, an atom is defined as a boundary atom when it has at most two bonds. Based on this definition of the boundary atoms, the geometry of a graphene plate can be obtained by using the following procedure: (1) identify the movable atoms by using the cut-off size; (2) identify the boundary atoms by using their definition as described above; and (3) make a least-squares fit to the boundary atoms by scaling and shifting the cut-off geometry. We refer to the graphene's geometric dimension obtained using such procedure as "standard size", as shown in Fig. 4.2.

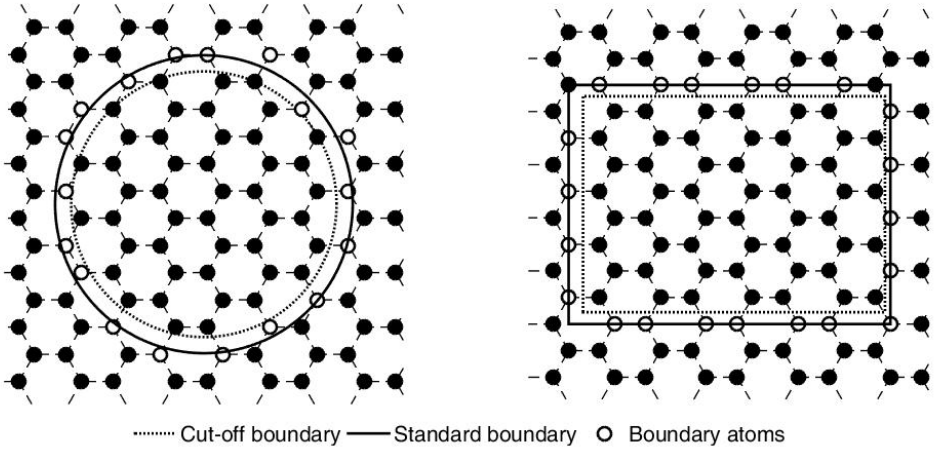

Figure 4.2: Illustration of cut-off size, standard size and boundary atoms.

Another factor that affects the performance of the plate models is the clamped boundary condition. It is an approximation to the actual case in which the boundary atoms and their exterior neighbors are all fixed. In the classical plate model, clamped boundary condition means no rotation of the plate's cross section ($dw/d\mathbf{n} = 0$, where $\mathbf{n}$ is the boundary normal vector). However, graphene has no obvious thickness and there is no cross section in the lattice. In fact, it is found that $dw/d\mathbf{n} = 0$ is too strong a boundary constraint for

graphene with fixed boundary atoms and their exterior neighbors. Figure 4.3 (a) and (b) show the boundary conditions of a continuous plate and a single-layer graphene lattice, both subjected to bending deformation. The red circles in Fig. 4.3 (b) represent fixed atoms and black ones are free atoms. It is clear that, in the bending graphene lattice, there is a finite angle between the bond attached to a fixed boundary atom and the horizontal axis, while $dw/d\mathbf{n} = 0$ of the continuous plate implies zero angle of rotation of the plate at the fixed boundary. Comparing the deflection obtained from atomic lattice mechanics calculation (black dashed line) and that calculated from the plate model described in Section 3.1 (blue solid line), the over-constraining boundary condition $dw/d\mathbf{n} = 0$ leads to an obvious discrepancy in the results, as shown in Fig. 4.3 (c). This effect tends to be more severe when the size of graphene becomes smaller. To address this inconsistency of the clamped boundary condition in the lattice and plates models, we suggest a simple yet effective zeroth order correction: increase the plate dimensions along the directions perpendicular to the clamped boundaries by a constant value, L_m. While more results demonstrating the effectiveness of L_m will be discussed in the results section, an example is shown in Fig. 4.3 (c) and (d). The red solid lines in both figures are the deflection curves of the plate with the dimension correction. It is shown that the zeroth order correction provides a compensation for the nonzero slope of the graphene lattice at the clamped boundary and the accuracy of the result is improved significantly.

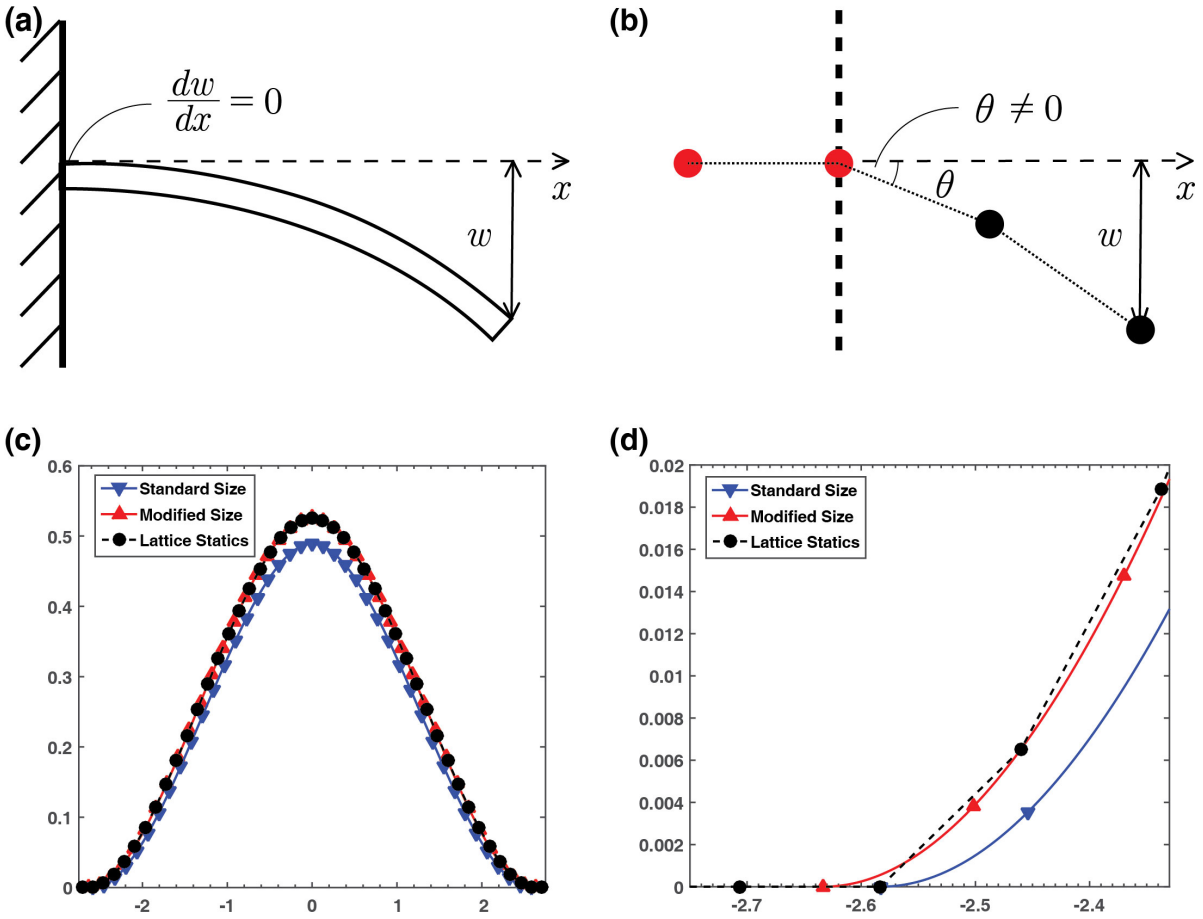

Figure 4.3: (a) and (b): deformation of a continuous plate and a single-layer graphene lattice near their clamped boundaries; (c): deflection of the graphene lattice and plates with standard and modified sizes; (d): enlarged boundary region of (c).

4.2.2 Results and Discussion

4.2.2.1 Static deformation

In this section, suspended SLGS subjected to a point load at center are investigated to test the proposed boundary corrections. Square and circular SLGS of different sizes are tested. All boundaries of the SLGS are clamped and a range of L_m are used in the calculations. By using the interatomic potential parameters given in Appendix A, D is

calculated to be 0.6896 eV. Figure (4.4) shows the relative error of center deflections of the SLGS with boundary corrections compared with the results obtained from the atomic lattice model. Results shown in Fig. (4.4) indicate that the using standard size instead of the integer cut-off size in the plate model reduces the error by about 50%. The introduction of size correction L_m further reduces the error significantly. Tables 4.1 and 4.2 show the corrected (standard) sizes and corresponding best L_ms for given integer cut-off sizes of square and circular SLGS. Note that the standard sizes are the sizes of the best fitting rectangles or circles to the fixed boundary atoms, as shown in Fig. 4.2. As shown in the tables, the best fitting L_m is clearly a function of the type and size of the SLGS. However, since the boundary condition induced error diminishes when the size of SLGS becomes larger, in this work, a zeroth order correction (i.e. a constant L_m) is considered sufficient. As shown in the later sections, from the static and modal analysis results of SLGS with different shapes and sizes, the value of $L_m = 0.03$ nm gives the best overall performance. Figure (4.4) shows that, with the standard size and $L_m = 0.03$ nm corrections, the largest error is less than 5% for square SLGS with edge length of 3 nm and above. Note that, since there is no distributed load, the non-local correction is only on the inertia term and it has no effect on the static analysis.

Table 4.1: Corrected size and the best fitting L_m of square SLGS (armchair in x-direction and zigzag in y-direction)

Cut-off size (nm)		3	5	10	15	20
Standard size	x	3.1958	5.1133	10.1556	15.1269	20.0271
(nm)	y	3.1982	5.1663	10.0866	15.0069	20.1732
Best fitting L_m (nm)		0.0710	0.0677	0.0559	0.0631	0.0623
Cut-off size (nm)		25	30	35		
Standard size	x	25.1405	30.1828	35.1541		
(nm)	y	25.0935	30.0138	35.1801		
Best fitting L_m (nm)		0.0619	0.0531	0.0616		

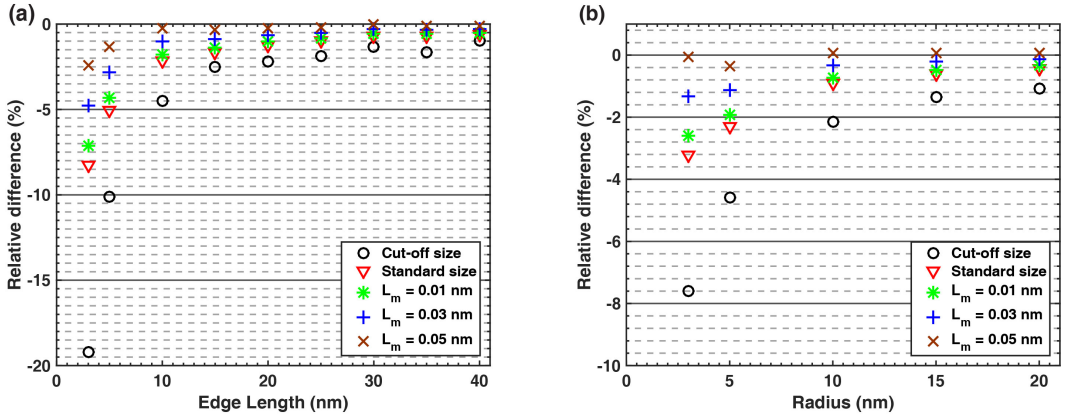

Figure 4.4: Relative error of the SLGS' center deflection in comparison with the results obtained from the atomic lattice model: (a) square SLGS and (b) circular SLGS. y-axis is the relative error of center deflection and x-axis is the size of SLGS.

Table 4.2: Corrected size and the best fitting L_m of circular SLGS.

Cut-off radius (nm)	3	5	10	15	20
Standard radius (nm)	3.0700	5.0593	10.0625	15.0567	20.0641
Best fitting L_m (nm)	0.0510	0.0595	0.0464	0.0455	0.0440

4.2.2.2 Modal frequencies of SLGS

To investigate the performance of the non-local plate model of SLGS, modal frequency analysis is used as the benchmark problem in this section. The modal frequency spectrum is a fundamental property of SLGS directly related to their dynamic behavior. In this calculation, the lowest 50 modal frequencies are calculated for SLGS with different sizes or shapes. Once again, the atomic lattice model results are used as the reference results. Size corrections is employed in both local and non-local models. Relative errors are calculated for results obtained from the local and non-local plate models.

We first test the behavior of the non-local plate model on square SLGS using different values of L_m and e_0a. Figure 4.5 shows the corresponding relative error of the first 50 modal frequencies of 5 nm $\times$ 5 nm (cut-off size) square SLGS. The results from the

classical local model, which are indicated by the black circles in Figure 4.5 (a), give a relative error of 4.3% for the first modal frequency, and then the error increases linearly as the mode number increases. Since higher frequency modes have smaller wave lengths, this result confirms Wu [92] and Peng [58]'s findings: the classic plate/shell model becomes inaccurate when the characteristic length of deformation pattern is small enough to be comparable to the atomic spacing. To reduce this error, as discussed above, two correction methods are available. The first is the size correction for error induced by the approximated boundary position and condition, as described in Sections 3.4 and 4.1. The second is the non-local correction of the stress tensor as described in Section 3.2. However, it is not clear what the right combination of the two corrections is for consistently reducing the error for all cases. Here, to understand the effect of L_m and e_0a on the accuracy of the plate model results, L_m and e_0a are varied independently and the relative error of the calculated modal frequencies are obtained and plotted in Figure 4.5. The results shown in Figure 4.5 reveal the relationship between the relative error of the results and the two correction parameters, L_m and e_0a. Based on the relationship, the optimal values of L_m and e_0a can be obtained. Figure 4.5 (a) shows the relative error variation as a function of mode number as well as the boundary correction factor L_m, while the non-local parameter e_0a is held to be zero. It is shown that, the error has an approximately linear relation with the mode number and changing L_m cuts down the y-intercept of the linear function. However, varying L_m does not change the slope of the linear error functions of the mode number. In comparison, Fig. 4.5 (b) shows effect of the non-local parameter. Note that, there is no boundary correction ($L_m = 0$) for all the results shown in Fig. 4.5 (b). The results show that, when e_0a increases, the slope of the linear error function of mode number reduces while the error of the first several modes is barely changed. That is, varying e_0a reduces the slope but not the y-intercept of the linear error function. At this point, it is clear that L_m and e_0a control the y-intercept and the slope of the linear error function, respectively. For a given SLGS, there

should be a combination of L_m and e_0a such that both the y-intercept and slope are close to zero. For example, for the 5 nm $\times$ 5 nm (cut-off size) SLGS, the best fitting values are $L_m = 0.0546nm$ and $e_0a \approx 0.05nm$.

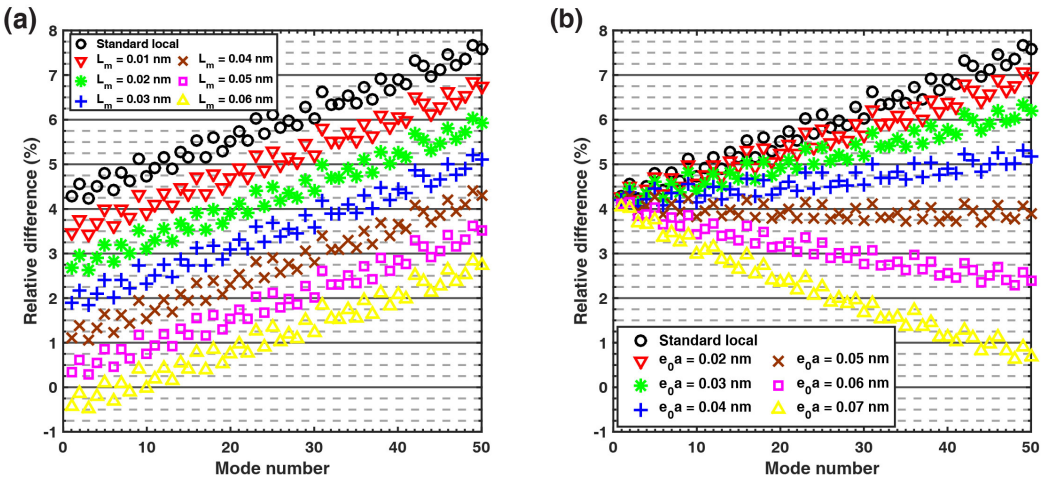

Figure 4.5: First 50 modal frequencies of 5 nm $\times$ 5 nm square SLGS with different values of (a) boundary correction factor L_m and (b) non-local parameter e_0a.

To test the conclusion obtained above, the modal frequency problem is solved for SLGS of various shapes and sizes. Figures 4.6, 4.7 and 4.8 show the results of square SLGS with different edge lengths, rectangular SLGS with different aspect ratios and sizes, and circular SLGS with different radii, respectively. Results obtained from the local plate model (e_0a=0) with standard size ($L_m = 0$) are also shown in the figures for comparison. The numerical results indicate that, similar to the static deformation cases, the best fitting L_m is a function of the type and size of the SLGS. As a trade-off between simplisity and accuracy, we set $L_m = 0.03$ nm as a zeroth order approximation. The results shown in Figs. 4.5-4.8 indicate that, however, the best fitting non-local parameter e_0a is largely independent from shape and size of the SLGS. With $e_0a = 0.05nm$, the slope of error is nearly zero for all cases. It is imporant to point out that, while this result is against most recent studies on graphene's non-local plate models, it is consistent with Eringen's original

work, in which $e_0 \approx 0.39$ was obtained [18]. If we consider $a = 0.142$ nm which is the carbon bond length in graphene, the result of this work $e_0 a = 0.05nm$ gives $e_0 = 0.352$. Indeed, the non-local plate model is only meaningful if a consistent non-local parameter can be used for plates of different shapes and sizes. Our results show that, with $e_0 a = 0.05$ nm and $L_m = 0.03$ nm, the relative errors are greatly reduced for all sizes, shapes and mode numbers. The remaining error is the result of the constant L_m which is a zeroth order approximation. It is worth noting that the results of the rectangular SLGS exhibit more variance due to their different sizes in different directions.

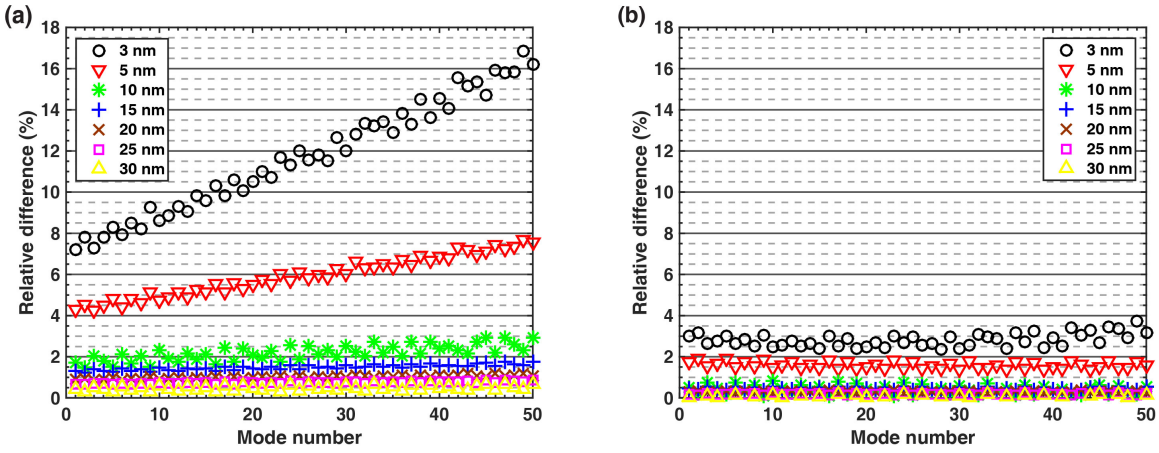

Figure 4.6: Relative error of the first 50 modal frequencies of square SLGS of various sizes: (a) local model with standard size ($e_0 a = 0$ and $L_m = 0$); (b) non-local model with $e_0 a = 0.05$ nm and $L_m = 0.03$ nm.

4.3 Summary

There are three major issues in the existing continuum plate models of SLGS. First, the conventional moment-curvature relation requires a structural property - plate thickness, which is not well defined due to the single layer lattice structure of SLGS. Therefore, the plate thickness becomes a fitting parameter in these plate models. Depending on the appli-

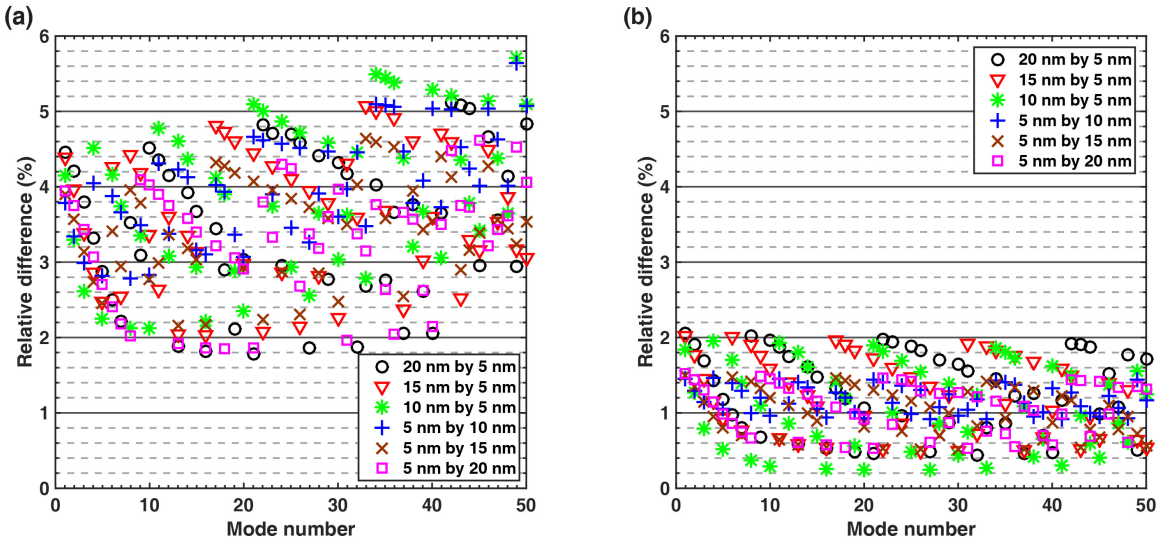

Figure 4.7: Relative difference of the first 50 modal frequencies of rectangular SLGS: (a) local model with standard size ($e_0a = 0$ and $L_m = 0$); (b) non-local model with $e_0a = 0.05$ nm and $L_m = 0.03$ nm.

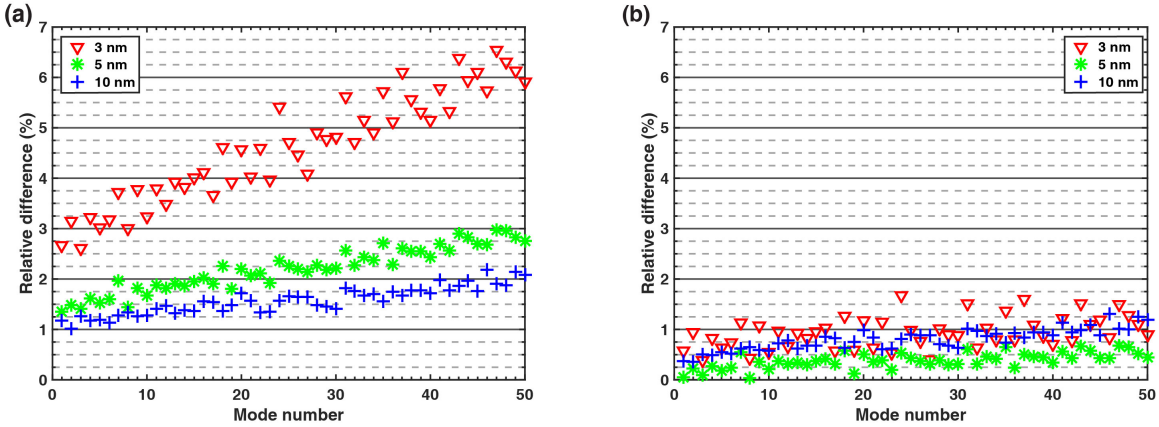

Figure 4.8: Relative difference of the first 50 modal frequencies of circular SLGS: (a) local model with standard size ($e_0a = 0$ and $L_m = 0$); (b) non-local model with $e_0a = 0.05$ nm and $L_m = 0.03$ nm.

cation, different values of plate thickness were used to fit experimental results or atomistic calculations. The second issue is the inconsistency in the definition of the boundary and boundary conditions between the continuum plate models and atomic lattice models. The third issue is that the classical continuum plate theory becomes inapplicable when the cha-

racteristic length of deformation pattern reduces to a level that is comparable to the atomic spacing.

In this work we show that, within the framework of a non-local plate model, these issues can be addressed to ensure the accuracy and consistency of the model. First, the plate thickness problem can be overcome by calculating the bending rigidity in the moment-curvature relation directly from the interatomic potential of graphene. In addition, the effect of boundary and boundary condition inconsistency on the static and dynamic behavior of SLGS can be alleviated by extending SLGS's dimensions at the clamped boundaries by a small amount L_m. It is demonstrated in the numerical results that L_m controls the constant component of the error and the non-local parameter e_0a controls the error proportionality with respect to the wavelength of deformation. Contrary to the case dependent non-local parameter values used in the literature, we show that, when the sources of error in the classical plate model are properly identified, the optimal non-local parameter e_0a is independent of size, shape and vibration pattern of the SLGS. Finally, by using potential-based bending rigidity, we found that a combination of $L_m = 0.03$ nm and $e_0a = 0.05$ nm gives accurate results for static and dynamic behavior of SLGS with different shapes and sizes.

Chapter 5

Potential-based non-local shell model of carbon nanotubes

As discussed in Chapter 2, many studies have been done on the shell modeling of carbon nanotubes. The rediscovery of non-local elasticity offered a capability to consider the atomic spacing in continuum models. However, from the author's best knowledge, most current non-local shell theories proposed for CNT are still based on continumm constitution relations, which has already been proved to be inappropriate [7, 31, 92]. In this chapter, a potential-oriented non-local Mindlin-Reissner shell theory for CNT is developed. The in-plane stiffness matrix and bending stiffness matrix are calculated based on Wu's derivation [92]. Penalty method is applied to suppress the shear deformation. To test the performance of this model, the spectral frequencies and wave propagation dispersion relations are calculated and compared with atomistic models.

5.1 Finite element formulation of non-local Mindlin-Reissner shell theory for single-walled carbon nanotubes

Currently the most successful plate or shell models of graphene and CNT are using pure-bending Kirchhoff-Love assumptions. However, pure-bending models require C_1 continuity, which is very difficult to satisfy in finite element analysis on 3D curved surfaces. For this reason, the Mindlin-Reissner theory based finite element models are far more popular in literature. For traditional continuum materials, this works well in most situations except for shear locking problems when the shell or plate is thin [32]. For graphene and CNT, however, there is no meaningful thickness and shear modulus, which causes troubles in determining the out-of-plane shear stiffness matrix defined in Eq. (2.10). To avoid requiring higher order continuity as well as to retain the pure-bending assumption, the Mindlin-Reissner hypothesis is still employed while a penalty method is used to suppress the out-of-plane shear deformation.

5.1.1 Governing equatiosn of thin shallow doubly-curved shell

The equation of motion of doubly-curved shell model is already shown in Eq. (5.1). For the sake of clearness, we rewrite it here:

$$\begin{aligned}
&\frac{\partial N_{11}}{\partial x_1}+\frac{\partial (N_{12}+C_0M_{12})}{\partial x_2}+\frac{Q_1}{R_1}-I_0\frac{\partial^2 u}{\partial t^2}-I_1\frac{\partial^2 \theta_x}{\partial t^2}=0\\
&\frac{\partial (N_{12}-C_0M_{12})}{\partial x_1}+\frac{\partial N_{22}}{\partial x_2}+\frac{Q_2}{R_2}-I_0\frac{\partial^2 v}{\partial t^2}-I_1\frac{\partial^2 \theta_y}{\partial t^2}=0\\
&\frac{\partial Q_1}{\partial x_1}+\frac{\partial Q_2}{\partial x_2}-\left(\frac{N_{11}}{R_1}+\frac{N_{22}}{R_2}\right)-q-I_0\frac{\partial^2 w}{\partial t^2}=0\\
&\frac{\partial M_{11}}{\partial x_1}+\frac{\partial M_{12}}{\partial x_2}-Q_1-I_1\frac{\partial^2 u}{\partial t^2}-I_2\frac{\partial^2 \theta_x}{\partial t^2}=0\\
&\frac{\partial M_{12}}{\partial x_1}+\frac{\partial M_{22}}{\partial x_2}-Q_2-I_1\frac{\partial^2 v}{\partial t^2}-I_2\frac{\partial^2 \theta_y}{\partial t^2}=0
\end{aligned} \tag{5.1}$$

where

$$C_0 = \frac{1}{R_1} - \frac{1}{R_2} \tag{5.2}$$

Eq. (5.1) can be simplified. Like any 2-D carbon nano-materials, CNT has no meaningful thickness due to its one atom layer structure. Therefore, $I_1 \propto \rho h^2$ and $I_2 \propto \rho h^3$ are considered to be 0 where h is the thickness, and $I_0 = \rho h$ equals to the averaged mass density per unit area of carbon atoms. Also for cylindrical surface shown in Fig. (5.1), R_1 is the radius of the cylinder and $R_2 = \infty$. If the radius is much greater than the element size, $\frac{1}{R_1}$ term can also be ignored. Moreover, similar to graphene, CNT has very small stiffness against twisting curvature, which means $C_0 M_{12}$ is negligible compared to N_{12}. Thus, Eq. (5.1) can be simplified as:

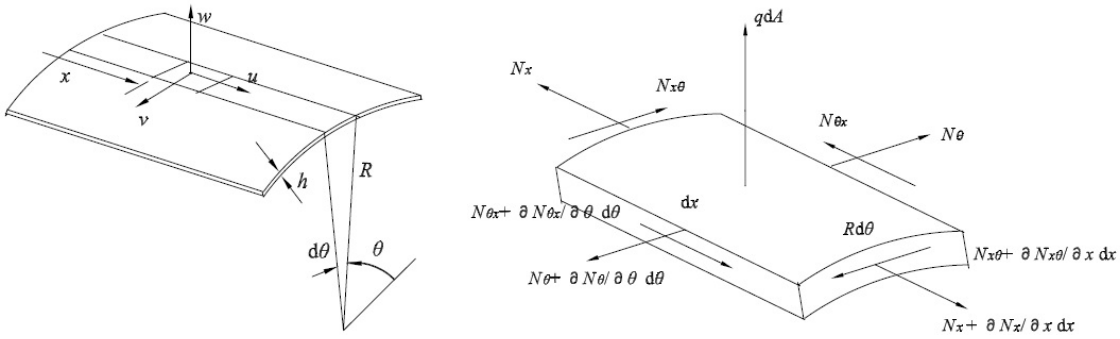

Figure 5.1: Demonstration of the cylindrical shell geometry and kinematics [85].

$$
\begin{aligned}
&\frac{\partial N_{11}}{\partial x_1} + \frac{\partial N_{12}}{\partial x_2} - I_0 \frac{\partial^2 u}{\partial t^2} = 0 \\
&\frac{\partial N_{12}}{\partial x_1} + \frac{\partial N_{22}}{\partial x_2} - I_0 \frac{\partial^2 v}{\partial t^2} = 0 \\
&\frac{\partial Q_1}{\partial x_1} + \frac{\partial Q_2}{\partial x_2} - q - I_0 \frac{\partial^2 w}{\partial t^2} = 0 \\
&\frac{\partial M_{11}}{\partial x_1} + \frac{\partial M_{12}}{\partial x_2} - Q_1 = 0 \\
&\frac{\partial M_{12}}{\partial x_1} + \frac{\partial M_{22}}{\partial x_2} - Q_2 = 0
\end{aligned}
\tag{5.3}
$$

which is the same as the equation of motion of a flat plate [85].

5.1.2 Non-local elasticity and non-local shell theory

The non-local elasticity theory was introduced in Chapter 2. Here it is described briefly for the sake of completeness. In the non-local theory, the mathematical expression of the stress-strain relation is given by [19]

$$
\boldsymbol{\sigma}(\mathbf{x}) = \int_{\Omega} \alpha(|\mathbf{x}' - \mathbf{x}|, \tau) \mathbf{C} : \boldsymbol{\epsilon}(\mathbf{x}') d\Omega(\mathbf{x}') \tag{5.4}
$$

When $\alpha(|\mathbf{x}' - \mathbf{x}|, \tau)$ is chosen to be the Green's function of a linear operator $\mathscr{L}$, Eq. (5.4) can be rewritten in the differential form:

$$
\mathscr{L}\boldsymbol{\sigma} = \mathbf{C} : \boldsymbol{\epsilon} \tag{5.5}
$$

In this work, $\mathscr{L}$ is chosen to be $1-(e_0a)^2$. Together with the resultant forces and moments defined in Eq. (2.9), we can easily obtain the non-local constitutive relations of shell [3, 6]:

$$\mathscr{L}\begin{bmatrix} N_{11} \\ N_{22} \\ N_{12} \\ Q_1 \\ Q_2 \\ M_{11} \\ M_{22} \\ M_{12} \end{bmatrix} = \begin{bmatrix} \mathbf{A}_{3\times3} & & \\ & \mathbf{C}_{2\times2} & \\ & & \mathbf{D}_{3\times3} \end{bmatrix} \begin{bmatrix} \epsilon_{11} \\ \epsilon_{22} \\ \gamma_{12} \\ \gamma_{13} \\ \gamma_{23} \\ \kappa_{11} \\ \kappa_{22} \\ \kappa_{12} \end{bmatrix} \tag{5.6}$$

(5.7)

where the in-plane strain-displacement relations are:

$$\begin{bmatrix} \epsilon_{11} \\ \epsilon_{22} \\ \gamma_{12} \end{bmatrix} = \begin{bmatrix} \dfrac{\partial}{\partial x_1} & \\ & \dfrac{\partial}{\partial x_2} \\ \dfrac{\partial}{\partial x_2} & \dfrac{\partial}{\partial x_1} \end{bmatrix} \begin{bmatrix} u \\ v \end{bmatrix}, \quad \begin{bmatrix} \gamma_{13} \\ \gamma_{23} \end{bmatrix} = \begin{bmatrix} \dfrac{\partial}{\partial x_1} & -1 & \\ \dfrac{\partial}{\partial x_2} & & -1 \end{bmatrix} \begin{bmatrix} w \\ \theta_1 \\ \theta_2 \end{bmatrix} \tag{5.8}$$

and the curvatures can be expressed as:

$$\begin{bmatrix} \kappa_{11} \\ \kappa_{22} \\ \kappa_{12} \end{bmatrix} = \begin{bmatrix} \dfrac{\partial}{\partial x_1} & \\ & \dfrac{\partial}{\partial x_2} \\ \dfrac{\partial}{\partial x_2} & \dfrac{\partial}{\partial x_1} \end{bmatrix} \begin{bmatrix} \theta_1 \\ \theta_2 \end{bmatrix} \tag{5.9}$$

Matrix $\mathbf{A}$, $\mathbf{C}$ and $\mathbf{D}$ are in-plane stiffness, out-of-plane shear stiffness and bending stiffness matrix, respectively. u, v, w, θ_1, θ_2 are displacements in local x_1, x_2, x_3 directions and rotations of x_1 x_3 and x_2 x_3 cross-sections. Note that the x_3 axis is perpendicular to the tangent of the shell surface at point (x_1, x_2, x_3).

If we apply $\mathscr{L}$ on both sides of Eq. (5.3), we can obtain the non-local equation of motion:

$$\begin{aligned}
&\frac{\partial \mathscr{L} N_{11}}{\partial x_1} + \frac{\partial \mathscr{L} N_{12}}{\partial x_2} - I_0 \mathscr{L} \frac{\partial^2 u}{\partial t^2} = 0 \\
&\frac{\partial \mathscr{L} N_{12}}{\partial x_1} + \frac{\partial \mathscr{L} N_{22}}{\partial x_2} - I_0 \mathscr{L} \frac{\partial^2 v}{\partial t^2} = 0 \\
&\frac{\partial \mathscr{L} Q_1}{\partial x_1} + \frac{\partial \mathscr{L} Q_2}{\partial x_2} - \mathscr{L} q - I_0 \mathscr{L} \frac{\partial^2 w}{\partial t^2} = 0 \\
&\frac{\partial \mathscr{L} M_{11}}{\partial x_1} + \frac{\partial \mathscr{L} M_{12}}{\partial x_2} + \mathscr{L} Q_1 = 0 \\
&\frac{\partial \mathscr{L} M_{12}}{\partial x_1} + \frac{\partial \mathscr{L} M_{22}}{\partial x_2} + \mathscr{L} Q_2 = 0
\end{aligned} \tag{5.10}$$

The corresponding weak form is:

$$\begin{aligned}
\int_\Omega \Bigg[&\left(\frac{\partial \delta u}{\partial x_1} \mathscr{L} N_{11} + \frac{\partial \delta u}{\partial x_2} \mathscr{L} N_{12} - \delta u I_0 \mathscr{L} \frac{\partial^2 u}{\partial t^2} \right) \\
&+ \left(\frac{\partial \delta v}{\partial x_1} \mathscr{L} N_{12} + \frac{\partial \delta v}{\partial x_2} \mathscr{L} N_{22} - \delta v I_0 \mathscr{L} \frac{\partial^2 v}{\partial t^2} \right) \\
&+ \left(\frac{\partial \delta w}{\partial x_1} \mathscr{L} Q_1 + \frac{\partial \delta w}{\partial x_2} \mathscr{L} Q_2 - \delta w \mathscr{L} q - \delta w I_0 \mathscr{L} \frac{\partial^2 w}{\partial t^2} \right) \\
&+ \left(\frac{\partial \delta \theta_1}{\partial x_1} \mathscr{L} M_{11} + \frac{\partial \delta \theta_1}{\partial x_2} \mathscr{L} M_{12} - \delta \theta_1 \mathscr{L} Q_1 \right) \\
&+ \left(\frac{\partial \delta \theta_2}{\partial x_1} \mathscr{L} M_{12} + \frac{\partial \delta \theta_2}{\partial x_2} \mathscr{L} M_{22} - \delta \theta_2 \mathscr{L} Q_2 \right) \Bigg] d\Omega \\
- \int_\Gamma &\left(\delta u P_1 + \delta v P_2 + \delta w Q_n + \delta \theta_1 T_1 + \delta \theta_2 T_2 \right) d\Gamma = 0
\end{aligned} \tag{5.11}$$

where the boundary forces and moments are defined as:

$$\begin{aligned} P_1 &= \mathscr{L}N_{11}n_1 + \mathscr{L}N_{12}n_2; \qquad & P_2 &= \mathscr{L}N_{12}n_1 + \mathscr{L}N_{22}n_2; \\ T_1 &= \mathscr{L}M_{11}n_1 + \mathscr{L}M_{12}n_2; \qquad & T_2 &= \mathscr{L}M_{12}n_1 + \mathscr{L}M_{22}n_2; \\ Q_n &= \mathscr{L}Q_1n_1 + \mathscr{L}Q_2n_2 \end{aligned} \tag{5.12}$$

n_1 and n_2 are components of the vector normal to the boundary.

5.1.3 Penalty method and the formulation of element matrices

The pure-bending conditions are equivalent to two constraints on the out-of-plane shear deformations, γ_{13} and γ_{23}, written as follows:

$$\gamma_{13} = \frac{\partial w}{\partial x_1} - \theta_1 = 0; \qquad \gamma_{23} = \frac{\partial w}{\partial x_2} - \theta_2 = 0; \tag{5.13}$$

Using Lagrange multiplier method, these constrains can be added to the weak form:

$$\begin{aligned} \int_\Omega \Bigg\{ & \left[\frac{\partial \delta u}{\partial x_1}\mathscr{L}N_{11} + \left(\frac{\partial \delta u}{\partial x_2} + \frac{\partial \delta v}{\partial x_1} \right)\mathscr{L}N_{12} + \frac{\partial \delta v}{\partial x_2}\mathscr{L}N_{22} \right] \\ & + \left[\frac{\partial \delta \theta_1}{\partial x_1}\mathscr{L}M_{11} + \left(\frac{\partial \delta \theta_1}{\partial x_2} + \frac{\partial \delta \theta_2}{\partial x_1} \right)\mathscr{L}M_{12} + \frac{\partial \delta \theta_2}{\partial x_2}\mathscr{L}M_{22} \right] \\ & - \delta w \mathscr{L}q - I_0 \left(\delta u \mathscr{L}\frac{\partial^2 u}{\partial t^2} + \delta v \mathscr{L}\frac{\partial^2 v}{\partial t^2} + \delta w \mathscr{L}\frac{\partial^2 w}{\partial t^2} \right) \\ & + \left[\phi_1 \delta \left(\frac{\partial w}{\partial x_1} - \theta_1 \right)^2 + \phi_2 \delta \left(\frac{\partial w}{\partial x_2} - \theta_2 \right)^2 \right] \Bigg\} d\Omega \\ - \int_\Gamma & \left(\delta u P_1 + \delta v P_2 + \delta w Q_n + \delta \theta_1 T_1 + \delta \theta_2 T_2 \right) d\Gamma = 0 \end{aligned} \tag{5.14}$$

where ϕ_1, ϕ_2 are Lagrange multipliers. It's obvious that ϕ_1, ϕ_2 are equivalent with the out-of-plane shear modulus in traditional shell or plate models. To apply constraints, we assign them with relatively large numbers, which are called penalty parameters [67].

Substitute the constitutive relations in Eq. (5.6) into Eq. (5.14), we can obtain the weak form governing equation in terms of displacements:

$$\begin{aligned}\int_\Omega \Bigg\{ &\left(\mathbf{b_1} \begin{bmatrix} \delta u \\ \delta v \end{bmatrix} \right)^T \cdot \mathbf{A} \cdot \left(\mathbf{b_1} \begin{bmatrix} u \\ v \end{bmatrix} \right) + \left(\mathbf{b_1} \begin{bmatrix} \delta\theta_1 \\ \delta\theta_2 \end{bmatrix} \right)^T \cdot \mathbf{D} \cdot \left(\mathbf{b_1} \begin{bmatrix} \theta_1 \\ \theta_2 \end{bmatrix} \right) \\ &+ \left(\mathbf{b_2} \begin{bmatrix} \delta w \\ \delta\theta_1 \\ \theta_2 \end{bmatrix} \right)^T \cdot \begin{bmatrix} \phi_1 & \\ & \phi_2 \end{bmatrix} \cdot \left(\mathbf{b_2} \begin{bmatrix} \delta w \\ \delta\theta_1 \\ \theta_2 \end{bmatrix} \right) \\ &- \delta w \mathscr{L} q - I_0 \left(\delta u \mathscr{L} \frac{\partial^2 u}{\partial t^2} + \delta v \mathscr{L} \frac{\partial^2 v}{\partial t^2} + \delta w \mathscr{L} \frac{\partial^2 w}{\partial t^2} \right) \Bigg\} d\Omega \\ - \int_\Gamma &\left(\delta u P_1 + \delta v P_2 + \delta w Q_n + \delta\theta_1 T_1 + \delta\theta_2 T_2 \right) d\Gamma = 0 \end{aligned} \tag{5.15}$$

where

$$\mathbf{b_1} = \begin{bmatrix} \dfrac{\partial}{\partial x_1} & \\ & \dfrac{\partial}{\partial x_2} \\ \dfrac{\partial}{\partial x_2} & \dfrac{\partial}{\partial x_1} \end{bmatrix}, \ \mathbf{b_2} = \begin{bmatrix} \dfrac{\partial}{\partial x_1} & -1 & \\ \dfrac{\partial}{\partial x_2} & & -1 \end{bmatrix} \tag{5.16}$$

Note that except for the boundary terms, the non-local operator only affects the inertia forces. We can do integration by parts on the inertia terms to reduce its continuity requirement. The inertia term in x_1 direction can be rewritten as:

$$\begin{aligned} \delta u \mathscr{L} \frac{\partial^2 u}{\partial t^2} &= \delta u \frac{\partial^2 u}{\partial t^2} - (e_0 a)^2 \delta u \nabla^2 \frac{\partial^2 u}{\partial t^2} \\ &= \delta u \frac{\partial^2 u}{\partial t^2} - (e_0 a)^2 \left[\nabla \cdot \left(\delta u \nabla \frac{\partial^2 u}{\partial t^2} \right) - \nabla \delta u \cdot \nabla \frac{\partial^2 u}{\partial t^2} \right] \end{aligned} \tag{5.17}$$

Thus, the corresponding integration form is equal to:

$$\begin{aligned}\int_{\Omega} I_0 \delta u \mathscr{L} \frac{\partial^2 u}{\partial t^2} d\Omega = \int_{\Omega} I_0 \left(\delta u \frac{\partial^2 u}{\partial t^2} + (e_0 a)^2 \nabla \delta u \cdot \nabla \frac{\partial^2 u}{\partial t^2} \right) d\Omega \\ - \int_{\Gamma} I_0 (e_0 a)^2 \delta u \left(\frac{\partial}{\partial x_1} \frac{\partial^2 u}{\partial t^2} n_1 + \frac{\partial}{\partial x_2} \frac{\partial^2 u}{\partial t^2} n_2 \right) d\Gamma\end{aligned} \tag{5.18}$$

Similarly, the same process can be done on $\mathscr{L} \dfrac{\partial^2 u}{\partial t^2}$ and $\mathscr{L} \dfrac{\partial^2 u}{\partial t^2}$ terms. The element stiffness and mass matrix can be written as:

$$\begin{aligned}\mathbf{K^e}_{5n\times 5n} &= \begin{bmatrix} \mathbf{K^e_d}_{2n\times 2n} & \\ & \mathbf{K^e_s}_{3n\times 3n} \end{bmatrix} + \begin{bmatrix} \mathbf{0}_{3n\times 3n} & \\ & \mathbf{K^e_r}_{2n\times 2n} \end{bmatrix} \\ \mathbf{M^e}_{5n\times 5n} &= \begin{bmatrix} \mathbf{M^e_b}_{n\times n} & & & & \\ & \mathbf{M^e_b}_{n\times n} & & & \\ & & \mathbf{M^e_b}_{n\times n} & & \\ & & & \mathbf{0}_{n\times n} & \\ & & & & \mathbf{0}_{n\times n} \end{bmatrix}\end{aligned} \tag{5.19}$$

where

$$\begin{aligned}\mathbf{K^e_d} &= \int_{\Omega^e} \mathbf{B_d}^T \cdot \mathbf{A} \cdot \mathbf{B_d} \, d\Omega^e \\ \mathbf{K^e_s} &= \phi_1 \int_{\Omega^e} \mathbf{B_s}^T \cdot \mathbf{B_s} \, d\Omega^e \\ \mathbf{K^e_r} &= \int_{\Omega^e} \mathbf{B_d}^T \cdot \mathbf{D} \cdot \mathbf{B_d} \, d\Omega^e \\ \mathbf{M^e_b} &= I_0 \int_{\Omega^e} \left(\mathbf{N_d}^T \cdot \mathbf{N_d} + (e_0 a)^2 \mathbf{N_x}^T \cdot \mathbf{N_x} \right) \, d\Omega^e\end{aligned} \tag{5.20}$$

and

$$\mathbf{B_d} = \begin{bmatrix} \dfrac{\partial \mathbf{N_d}}{\partial x_1} & \\ & \dfrac{\partial \mathbf{N_d}}{\partial x_2} \\ \dfrac{\partial \mathbf{N_d}}{\partial x_2} & \dfrac{\partial \mathbf{N_d}}{\partial x_1} \end{bmatrix}, \ \mathbf{B_s} = \begin{bmatrix} \dfrac{\partial \mathbf{N_d}}{\partial x_1} & -\mathbf{N_d} & \\ \dfrac{\partial \mathbf{N_d}}{\partial x_2} & & -\mathbf{N_d} \end{bmatrix}, \ \mathbf{N_x} = \begin{bmatrix} \dfrac{\partial \mathbf{N_d}}{\partial x_1} \\ \dfrac{\partial \mathbf{N_d}}{\partial x_2} \end{bmatrix} \tag{5.21}$$

The vector $\mathbf{N_d}$ is the $1 \times n$ shape functions vector, and n is the number of element nodes.

5.1.4 Coordinate systems and matrix assembly

In shell elements the element matrices and force vector are evaluated at each Gauss point, under the local coordinate system. So the element matrices and vector should be transferred into global coordinate system in order to assemble into the global matrices and global vector. The position at any point in a shell elements can be expressed in global coordinates:

$$\mathbf{x} = \sum_k N_k(\xi, \eta)\mathbf{x^{(k)}}, \qquad i = 1, 2, 3 \tag{5.22}$$

k is the element node index, and $\mathbf{x^{(k)}} = [x_1^{(k)},\ x_2^{(k)},\ x_3^{(k)}]$ represents the global Cartesian coordinates of node k in this element. ξ and η are coordinates of the mapping of this point in the master element. The base vectors of the local coordinate system at this point can be defined as: [32]

$$\begin{aligned} \mathbf{e}_1^l &= \frac{\sqrt{2}}{2}(\mathbf{e}_\alpha - \mathbf{e}_\beta) \\ \mathbf{e}_2^l &= \frac{\sqrt{2}}{2}(\mathbf{e}_\alpha + \mathbf{e}_\beta) \\ \mathbf{e}_3^l &= \frac{\mathbf{e}_\xi \times \mathbf{e}_\eta}{|\mathbf{e}_\xi \times \mathbf{e}_\eta|} \end{aligned} \quad with \quad \begin{aligned} \mathbf{e}_\alpha &= \frac{(\mathbf{e}_\xi + \mathbf{e}_\eta)}{|\mathbf{e}_\xi + \mathbf{e}_\eta|} \\ \mathbf{e}_\beta &= \frac{\mathbf{e}_3^l \times \mathbf{e}_\alpha}{|\mathbf{e}_3^l \times \mathbf{e}_\alpha|} \end{aligned} \quad and \quad \begin{aligned} \mathbf{e}_\xi &= \frac{\mathbf{x}_{,\xi}}{|\mathbf{x}_{,\xi}|} \\ \mathbf{e}_\eta &= \frac{\mathbf{x}_{,\eta}}{|\mathbf{x}_{,\eta}|} \end{aligned} \tag{5.23}$$

where

$$\begin{aligned}\mathbf{x}_{,\xi} &= \frac{\partial \mathbf{x}}{\partial \xi} = \sum_k \frac{\partial N_k(\xi,\eta)}{\partial \xi}\mathbf{x}^{(\mathbf{k})} \\ \mathbf{x}_{,\eta} &= \frac{\partial \mathbf{x}}{\partial \eta} = \sum_k \frac{\partial N_k(\xi,\eta)}{\partial \eta}\mathbf{x}^{(\mathbf{k})}\end{aligned} \tag{5.24}$$

The displacements can be transferred from global coordinates into local coordinates by:

$$\begin{bmatrix} u^l \\ v^l \\ w^l \end{bmatrix} = \mathbf{Q}\cdot\begin{bmatrix} u^g \\ v^g \\ w^g \end{bmatrix} \quad , \quad \begin{bmatrix} \theta_1^l \\ \theta_2^l \\ \theta_3^l \end{bmatrix} = \mathbf{Q}\cdot\begin{bmatrix} \theta_1^g \\ \theta_2^g \\ \theta_3^g \end{bmatrix} \quad , \quad \mathbf{Q} = \begin{bmatrix} \mathbf{e}_1^l & \mathbf{e}_2^l & \mathbf{e}_3^l \end{bmatrix} \tag{5.25}$$

From the previous section, the equation of motion for each element can be written as:

$$\mathbf{K^e}\cdot\mathbf{d^e} + \mathbf{M^e}\cdot\ddot{\mathbf{d}}^{\mathbf{e}} = \mathbf{F^e} \tag{5.26}$$

$\mathbf{d^e}$ and $\mathbf{F^e}$ are element displacement and force vectors. Note that there are only 5 degrees of freedom (DOF) appeared in the weak form (u, v, w, θ_1, θ_2). However, after coordinate transfer there will be 6 DOF. So we add one more rotational DOF, θ_3, which represents the rotation around $\mathbf{e}_3^l$ axis. It is also called the drilling degree of freedom [32]. It worth to mention that there is neither stiffness nor inertia associated with this DOF, which can cause singular problems at some flat node. There are several methods to add the drilling stiffness and mass inertia [1, 33], but it is unnecessary in this work since we currently only deal with cylindrical geometries.

As a general finite element approach, integration in Eq. (5.20) is done by Gaussian quadrature. Selective reduced integration method is applied to reduce the shear locking and

membrane locking. That is, $\mathbf{K_r^e}$ and $\mathbf{M_b^e}$ are calculated using the number of Gauss points that fits the order of shape functions, while $\mathbf{K_d^e}$ and $\mathbf{K_s^e}$ are using one less Gauss points in each direction. In this work, 8-node quadrilateral serendipity element is selected. Meshes are generated by ANSYS Mehcanical APDL (ANSYS Academic Research Mechanical, Release 16.0). The number of Gauss points is set to be 3×3 for DOF with regular integration and 2×2 for DOF with reduced integration. The out-of-plane shear penalty parameters ϕ_1, ϕ_2 are set to be 10 times of the in-plane shear stiffness (A_{33}) of CNTs.

5.2 Potential based constitutive relations of CNT

As stated in the introduction chapter, it is hard to define CNT's material properties, such as the Young's modulus, the Poisson's ratio and the plate thickness, as those of traditional continuum materials. To solve this issue, Wu [92] has derived a inter-atomic potential based method in which $\mathbf{A}$ and $\mathbf{D}$ are directly calculated based on CNT's radius and chirality.

From the knowledge of differential geometry, a point P on a curved surface can be given by a vector function with two parameters (coordinates) $\mathbf{P}(\xi_1, \xi_2)$, which can define the curved surface. The first fundamental form, which represents the arc length on the curved surface, is given by:

$$A_{\alpha\beta} = \frac{\partial \mathbf{P}}{\partial \xi_\alpha} \cdot \frac{\partial \mathbf{P}}{\partial \xi_\beta} \tag{5.27}$$

And the second fundamental term that represents the curvature at point $\mathbf{P}$ is:

$$B_{\alpha\beta} = \mathbf{N} \cdot \frac{\partial^2 \mathbf{P}}{\partial \xi_\alpha \partial \xi_\beta} \tag{5.28}$$

where $\mathbf{N}$ is the unit vector that is normal to the surface at point $\mathbf{P}$, which can be obtained

from:

$$\mathbf{N} = \frac{\partial \mathbf{P}}{\partial \xi_\alpha} \times \frac{\partial \mathbf{P}}{\partial \xi_\beta} \Big/ \left| \frac{\partial \mathbf{P}}{\partial \xi_\alpha} \times \frac{\partial \mathbf{P}}{\partial \xi_\beta} \right| \tag{5.29}$$

Let $\mathbf{P}_i(\xi_1^i, \xi_2^i)$, $\mathbf{P}_j(\xi_1^j, \xi_2^j)$ and $\mathbf{P}_k(\xi_1^k, \xi_2^k)$ represent the positions of three different carbon atoms. Then the distance r_{ij} between atoms i, j and the angle θ_{ijk} between vectors i-j and i-k can be approximated by [92]

$$r_{ij}^2 = \Delta\mathbf{P}_{ij} \cdot \Delta\mathbf{P}_{ij} = (A_{\alpha\beta} + 2E_{\alpha\beta})\, \Delta\bar{\xi}_\alpha^{ij} \Delta\bar{\xi}_\beta^{ij} - \frac{1}{12}\left[(B_{\alpha\beta} + K_{\alpha\beta})\, \Delta\bar{\xi}_\alpha^{ij} \Delta\bar{\xi}_\beta^{ij}\right]^2$$

$$\begin{aligned} \cos\theta_{ijk} &= \frac{\Delta\mathbf{P}_{ij} \cdot \Delta\mathbf{P}_{ik}}{r_{ij} r_{ik}}, \\ \Delta\mathbf{P}_{ij} \cdot \Delta\mathbf{P}_{ik} =\ & (A_{\alpha\beta} + 2E_{\alpha\beta})\, \Delta\bar{\xi}_\alpha^{ij} \Delta\bar{\xi}_\beta^{ik} + \frac{1}{12}(B_{\alpha\beta} + K_{\alpha\beta})(B_{\gamma\lambda} + K_{\gamma\lambda}) \\ & \Delta\bar{\xi}_\alpha^{ij} \Delta\bar{\xi}_\lambda^{ik} \left(3\Delta\bar{\xi}_\beta^{ij} \Delta\bar{\xi}_\gamma^{ik} - 2\Delta\bar{\xi}_\beta^{ij} \Delta\bar{\xi}_\gamma^{ij} - 2\Delta\bar{\xi}_\beta^{ik} \Delta\bar{\xi}_\gamma^{ik}\right) \end{aligned} \tag{5.30}$$

where the same Greek subscript implies summation. $\Delta\mathbf{P}_{ij} = \mathbf{P}_j - \mathbf{P}_i$ means the vector from atom i to atom j. $\Delta\bar{\xi}_\alpha^{ij} = \Delta\xi_\alpha^{ij} + \eta_\alpha$ with $\Delta\xi_\alpha^{ij} = \xi_\alpha^j - \xi_\alpha^i$ is the coordinate difference between atoms i and j, and η^α represents the shift vector $\boldsymbol{\eta}$ between two sub-lattice in CNT. Here $A_{\alpha\beta}$ and $B_{\alpha\beta}$ are evaluated at point $\mathbf{P}_i$. $E_{\alpha\beta}$ and $K_{\alpha\beta}$ are components of the Green's strain tensor $\mathbf{E}$ and the curvature tensor $\mathbf{K}$, respectively.

If we equalize the strain energy density with atomic potential energy density, then the strain energy can be expressed as a function of strain/curvature tensors of CNT. In this work, we employed the 2nd generation REBO potential to simulate the interactions between carbon atoms [11]. The potential energy between atoms i and j can be written as a function of bond lengths and angles: $V_{ij}(r_{ij}, \theta_{ijk}, k \neq i, j)$. The strain energy density W

at atom i equals to:

$$W(\mathbf{E},\mathbf{K},\boldsymbol{\eta}) = \frac{1}{2}\frac{\sum_{j\neq i}^{j} V_{ij}(r_{ij},\theta_{ijk},k\neq i,j)}{S_0} \tag{5.31}$$

where $S_0 = \int\int \sqrt{A_{11}A_{22}-A_{12}^2}\, d\xi_1 d\xi_2$ is the average area per atom. Shift vector $\boldsymbol{\eta}$ can be obtained from an implicit non-linear function:

$$\frac{\partial W}{\partial \boldsymbol{\eta}} = 0 \tag{5.32}$$

Thus, the strain energy W is expressed as a function of $\mathbf{E}$ and $\mathbf{K}$: $W(\mathbf{E},\mathbf{K},\boldsymbol{\eta}(\mathbf{E},\mathbf{K})) = \widetilde{W}(\mathbf{E},\mathbf{K})$. Under small strain condition, $\mathbf{E}$ and $\mathbf{K}$ are equal to $\boldsymbol{\epsilon}$ and $\boldsymbol{\kappa}$ defined in Eq. (2.3). The stiffness matrix $\mathbf{A}$ and $\mathbf{D}$ can be obtained by:

$$\mathbf{A} = \begin{bmatrix} \dfrac{\partial^2\widetilde{W}}{\partial {E_{11}}^2} & \dfrac{\partial^2\widetilde{W}}{\partial E_{11}\partial E_{22}} & \dfrac{1}{2}\left(\dfrac{\partial^2\widetilde{W}}{\partial E_{11}\partial E_{12}}+\dfrac{\partial^2\widetilde{W}}{\partial E_{11}\partial E_{21}}\right) \\ & \dfrac{\partial^2\widetilde{W}}{\partial {E_{22}}^2} & \dfrac{1}{2}\left(\dfrac{\partial^2\widetilde{W}}{\partial E_{22}\partial E_{12}}+\dfrac{\partial^2\widetilde{W}}{\partial E_{22}\partial E_{21}}\right) \\ & & \dfrac{1}{4}\left(\dfrac{\partial^2\widetilde{W}}{\partial {E_{12}}^2}+2\dfrac{\partial^2\widetilde{W}}{\partial E_{12}\partial E_{21}}+\dfrac{\partial^2\widetilde{W}}{\partial {E_{21}}^2}\right) \end{bmatrix}_{Symm}$$

$$\mathbf{D} = \begin{bmatrix} \dfrac{\partial^2\widetilde{W}}{\partial {K_{11}}^2} & \dfrac{\partial^2\widetilde{W}}{\partial K_{11}\partial K_{22}} & \dfrac{1}{2}\left(\dfrac{\partial^2\widetilde{W}}{\partial K_{11}\partial K_{12}}+\dfrac{\partial^2\widetilde{W}}{\partial K_{11}\partial K_{21}}\right) \\ & \dfrac{\partial^2\widetilde{W}}{\partial {K_{22}}^2} & \dfrac{1}{2}\left(\dfrac{\partial^2\widetilde{W}}{\partial K_{22}\partial K_{12}}+\dfrac{\partial^2\widetilde{W}}{\partial K_{22}\partial K_{21}}\right) \\ & & \dfrac{1}{4}\left(\dfrac{\partial^2\widetilde{W}}{\partial {K_{12}}^2}+2\dfrac{\partial^2\widetilde{W}}{\partial K_{12}\partial K_{21}}+\dfrac{\partial^2\widetilde{W}}{\partial {K_{21}}^2}\right) \end{bmatrix}_{Symm} \tag{5.33}$$

where [92]

$$\begin{aligned}
\frac{\partial^2 \widetilde{W}}{\partial E_{\alpha\beta}\partial E_{\gamma\lambda}} &= \frac{\partial^2 W}{\partial E_{\alpha\beta}\partial E_{\gamma\lambda}} - \frac{\partial^2 W}{\partial E_{\alpha\beta}\partial \eta_{\nu}} \cdot \left(\frac{\partial^2 W}{\partial \boldsymbol{\eta}\partial \boldsymbol{\eta}}\right)^{-1}_{\nu\mu} \cdot \frac{\partial^2 W}{\partial \eta_{\mu}\partial E_{\gamma\lambda}} \\
\frac{\partial^2 \widetilde{W}}{\partial K_{\alpha\beta}\partial K_{\gamma\lambda}} &= \frac{\partial^2 W}{\partial K_{\alpha\beta}\partial K_{\gamma\lambda}} - \frac{\partial^2 W}{\partial K_{\alpha\beta}\partial \eta_{\nu}} \cdot \left(\frac{\partial^2 W}{\partial \boldsymbol{\eta}\partial \boldsymbol{\eta}}\right)^{-1}_{\nu\mu} \cdot \frac{\partial^2 W}{\partial \eta_{\mu}\partial K_{\gamma\lambda}}
\end{aligned} \tag{5.34}$$

$$\alpha, \beta, \gamma, \lambda, \nu, \mu = 1, 2$$

For detailed potential function and its derivatives, please see Appendices C and D.

It is worth to mention that the elastic constants calculated from Eq. (5.33) are approximations. The expressions of r_{ij} and $\cos\theta_{ijk}$ in Eq. (5.30) neglect higher order terms of $\Delta\xi$. Wu deduced a brief error analysis and the error of this method is on the order of $(a/R)^3$ and a/L, where a is the atomic spacing of CNT, R and L are tube radius and length. For (5,5) armchair CNT, $R = 0.35nm$ and the error is on the order of 6.4% if $L > 2.19nm$. It seems reasonable for such a narrow tube. However, this only represents the order of the magnitude. The actual error can be several times of this number, which is not acceptable. Therefore, in this work we only deal with relative large CNTs with $R > 0.5nm$ and $L > 9nm$.

5.3 Results and Discussions

The 2nd generation REBO (Brenner) potential is used for all elastic constants derivations, lattice static force constants calculations, and molecular dynamic simulations. The elastic constants are directly obtained from Eq. (5.33), with equilibrium geometry obtained from the optimization method implemented in Chapter 3. Since the atomic spacing in CNT is similar to graphene, the non-local parameter is selected to be $e_0 a = 0.05nm$ as well. The performance of this non-local shell model is tested by modal spectral analysis and wave

propagation of CNTs. The natural frequencies are calculated by computing the eigenvalues of the finite element stiffness matrix with respect to the mass matrix. Lattice static models are used as frequency references, with the force constant matrix obtained from Eq. (4.1) to Eq. (4.4) in Chapter 4. And molecular dynamics simulations are also presented to compare with the dynamics wave propagation simulations in the shell model.

5.3.1 Natural frequencies of carbon nanotubes

The natural frequencies are calculated for two armchair nanotubes (10,10), (15,15) and two zigzag nanotubes (15,0), (25,0) with clamped boundary conditions. Each CNT is tested with two different lengths. As we already discussed about the size of graphene in Chapter 4, the accurate length of CNT is defined as the distance between boundary atoms at both ends. And to relax the clamped boundary condition, a boundary correction factor $L_m = 0.03nm$ is applied. All relative differences are compared with lattice statics results.

Results show that the modified non-local model can reduce the frequency error significantly. It's effect varies with the vibration pattern, but on average the error is reduced by around one percent. It's easy to see that the boundary correction is more effective on short tubes. Note that there are several modes that are almost not effected by the boundary correction. These modes are vibrations primarily move along either the longitudinal axis or the radial direction, which involves little out-of-plane movements. This is in agreement with our analysis in Chapter 4 on why clamped boundary conditions are over constrained. Modes with less out-of-plane bending deformation are less affected by the over-constrained boundary.

It's also been observed that the non-local parameter has more influence on modes with more "fluctuations", which means the modes with smaller characteristic length. This is in consent with our observation in Chapter 4 on graphene. The remaining error may

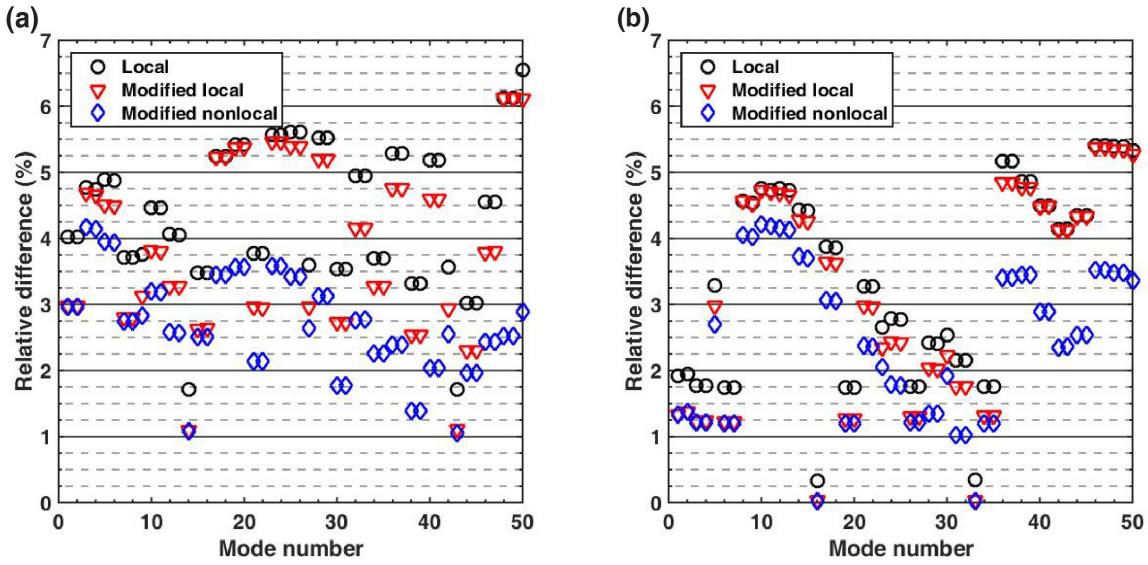

Figure 5.2: The relative difference of the first 50 natural frequencies of (10,10) carbon nanotubes, compared with lattice mechanics results. The tube lengths are (a) 9.84 nm and (b) 19.93 nm for the original local model and (a) 9.9 nm and (b) 19.99 nm for modified local and non-local models.

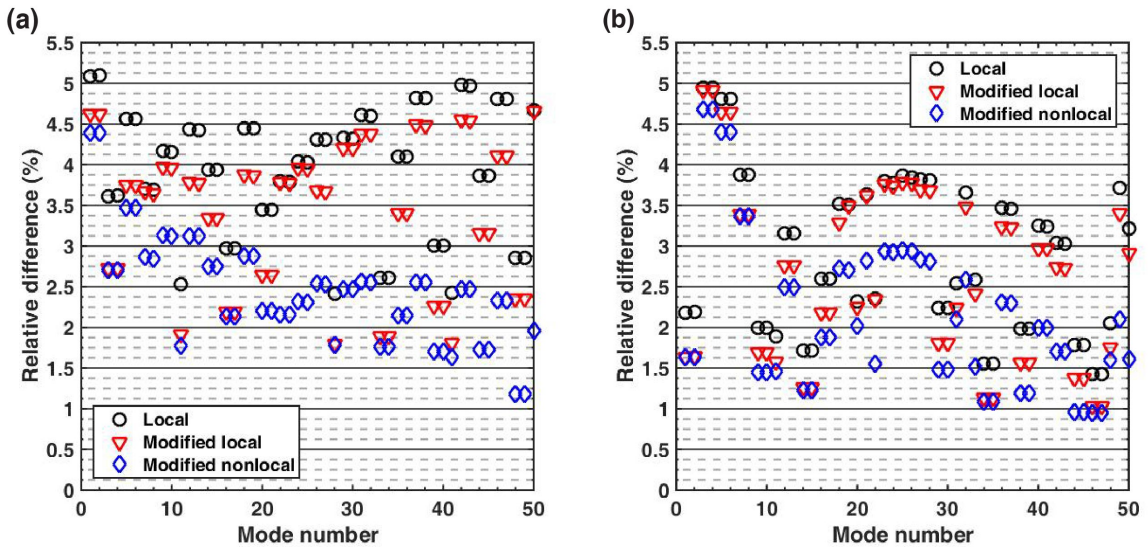

Figure 5.3: The relative difference of the first 50 natural frequencies of (15,15) carbon nanotubes, compared with lattice mechanics results. The tube lengths are (a) 9.84 nm and (b) 19.93 nm for the original local model and (a) 9.9 nm and (b) 19.99 nm for modified local and non-local models.

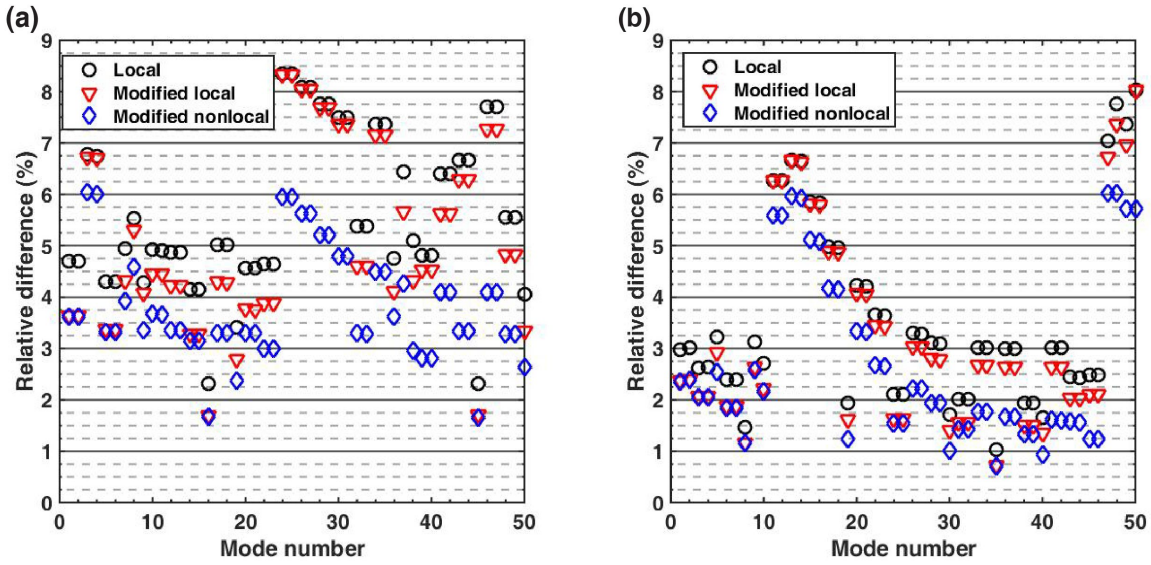

Figure 5.4: The relative difference of the first 50 natural frequencies of (15,0) carbon nanotubes, compared with lattice mechanics results. The tube lengths are (a) 9.86 nm and (b) 19.86 nm for the original local model and (a) 9.92 nm and (b) 19.92 nm for modified local and non-local models.

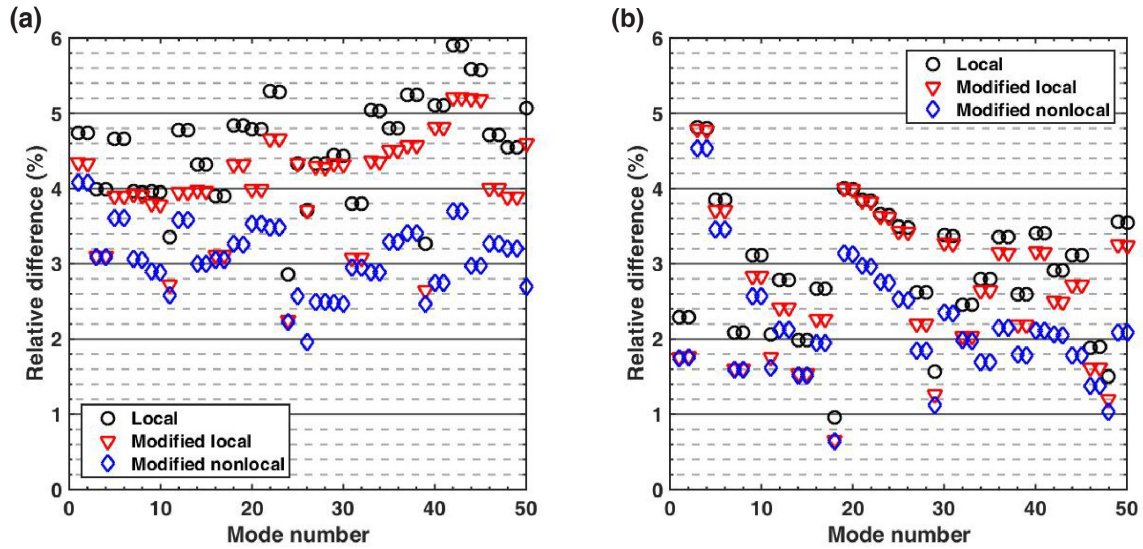

Figure 5.5: The relative difference of the first 50 natural frequencies of (25,0) carbon nanotubes, compared with lattice mechanics results. The tube lengths are (a) 9.86 nm and (b) 19.86 nm for the original local model and (a) 9.92 nm and (b) 19.92 nm for modified local and non-local models.

come from the stiffness matrix which is mentioned in Section 5.2.

5.3.2 Wave propagation in carbon nanotubes

To investigate the wave propagation problems, we test CNTs with 20 nm in length, which is subjected to sinusoidal excitation at one end while the other end is free. Two different excitation modes, namely flexural and longitudinal, are both investigated. As shown in Fig. (5.6), the wave travel time between two different cross-sections at $x = x_1$ and $x = x_2$ along the tube axis is calculated by [29]:

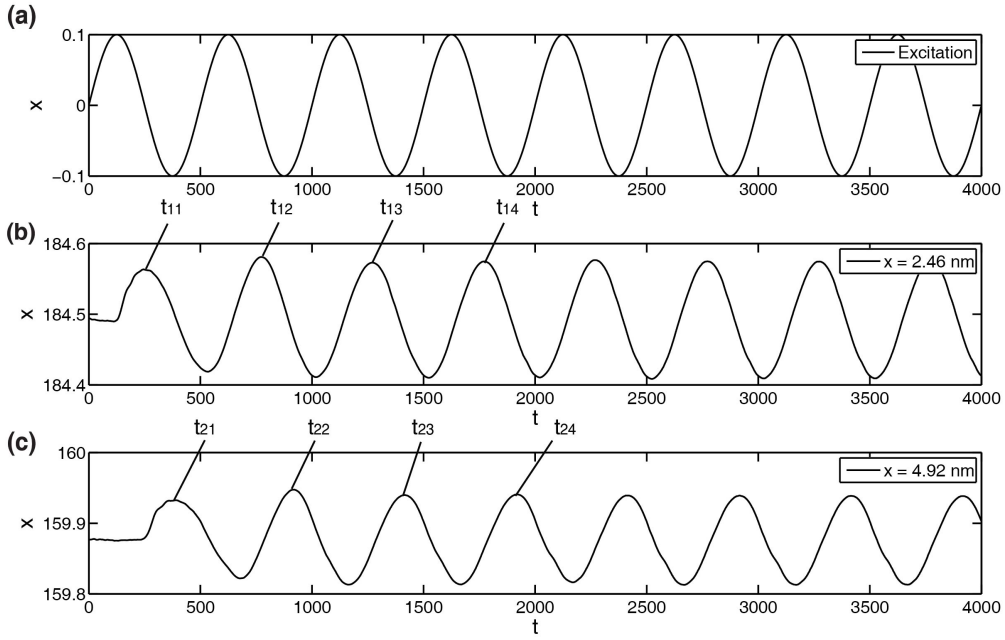

Figure 5.6: Vibrations of different cross-sections in a (15,15) armchair CNT under T = 500 fs longitudinal excitation. Result is from MD simulation. (a) shows the excitation wave, (b) and (c) are the corresponding responses at $x_1 = 2.46nm$ and $x_2 = 4.92nm$

$$\Delta t = \frac{(t_{21} - t_{11}) + (t_{22} - t_{12}) + (t_{23} - t_{13}) + \cdots + (t_{2n} - t_{1n})}{n} \tag{5.35}$$

Thus, the group velocity and wave number can be obtained as [29]:

$$c = \frac{x_2 - x_1}{\Delta t} , \qquad k = \frac{2\pi}{T}\frac{1}{c} \tag{5.36}$$

In the shell model, the Newmark method is employed for dynamic analysis. In the Newmark scheme, at each time step i the new displacement for next time step is given by

$$\begin{aligned} \mathbf{u}_{i+1} &= \mathbf{u}_i + \Delta t \dot{\mathbf{u}}_i + \frac{1}{2}\Delta t^2 \ddot{\mathbf{u}}_\beta \\ \dot{\mathbf{u}}_{i+1} &= \dot{\mathbf{u}}_i + \Delta t \ddot{\mathbf{u}}_\gamma \end{aligned} \tag{5.37}$$

where $\mathbf{u}_i$ is the displacement vector at time step i, $\dot{\mathbf{u}}_i$ is the velocity vector at time step i, and Δt is the time step size. The acceleration terms $\ddot{\mathbf{u}}_\beta$ and $\ddot{\mathbf{u}}_\gamma$ are given by:

$$\begin{aligned} \ddot{\mathbf{u}}_\beta &= (1-2\beta)\ddot{\mathbf{u}}_i + 2\beta\ddot{\mathbf{u}}_{i+1} , \qquad 0 \le 2\beta \le 1 \\ \ddot{\mathbf{u}}_\gamma &= (1-\gamma)\ddot{\mathbf{u}}_i + \gamma\ddot{\mathbf{u}}_{i+1} , \qquad 0 \le \gamma \le 1 \end{aligned} \tag{5.38}$$

where $\ddot{\mathbf{u}}_i$ is the acceleration vector at time step i. In this work we used $\gamma = 0.5$ and $\beta = 0.25$. The time step size is chosen differently for different period of sinusoidal excitation, but it is no greater than 1/50 of the corresponding period.

In MD simulations, Nose-Hoover style time integration is used. The initial atoms position is given by the bond length and angles obtained from Chapter 3, and the initial velocity is set randomly at the temperature 40K following the normal distribution. Before running the wave propagation test the whole system is relaxed and cooled down to $T = 1K$ by 150000 time steps with 0.2 fs step size. Then the temperature is controled to 1K, and atoms at one end are forced to move in a sinusoidal way with 0.01 nm magnitude. The simulation is proceeded by the open-source MD software LAMMPS [59].

It can be seen that the phase velocities from the non-local model are close to their lo-

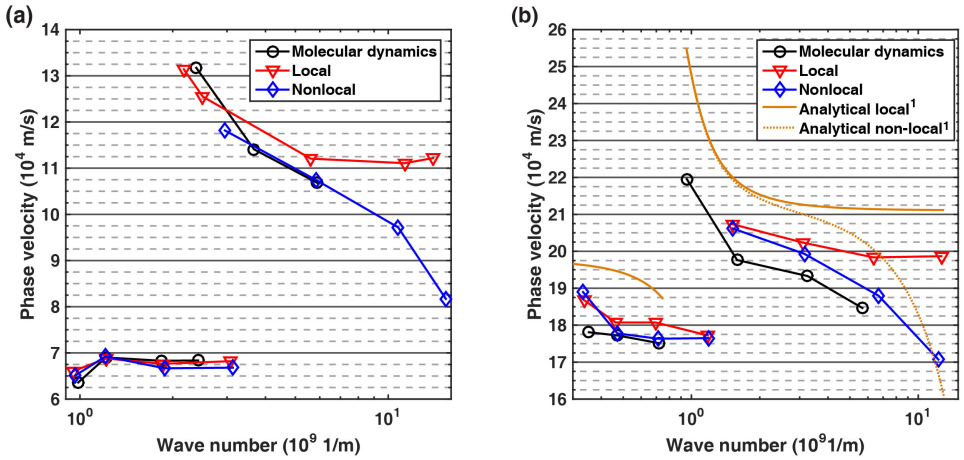

Figure 5.7: The dispersion relations of (a) flexural wave (b) longitudinal wave for (25,0) zigzag carbon nanotube.

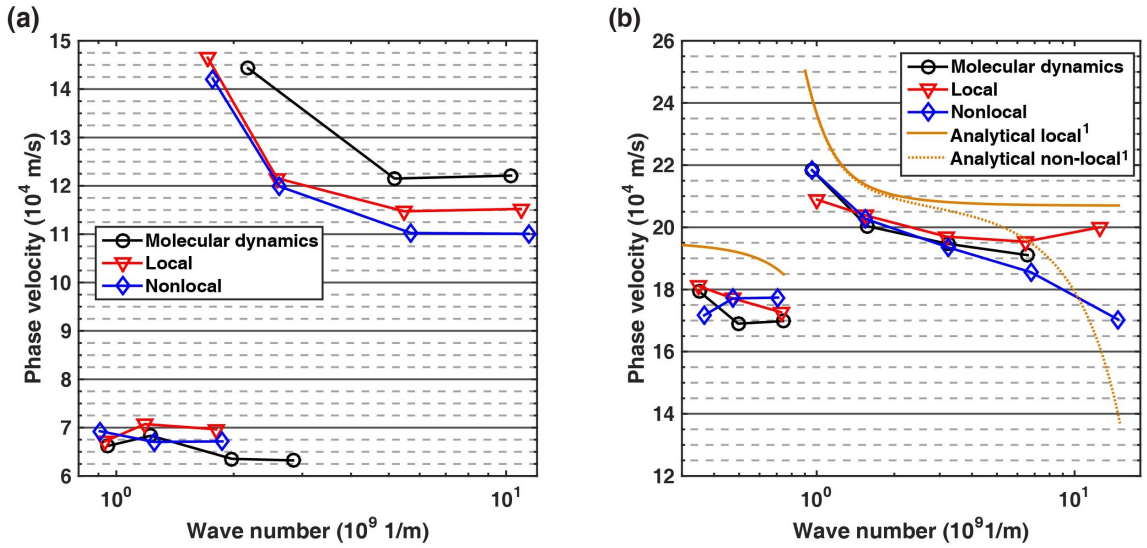

Figure 5.8: The dispersion relations of (a) flexural wave (b) longitudinal wave for (15,15) armchair carbon nanotube.

cal counter-parts. Most of the disagreements appear at the large wave number region, which indicates that the non-local effect makes more obvious difference on waves with smaller wave lengths. And by compare with MD simulation results, for (25,0) zigzag tube the non-local model has a better performance. The local model tends to over-estimate the phase

velocities, which can be compensated by the non-local effect. But the armchair (15,15) CNT shows no significant improvement. Most results from both longitudinal and flexural waves are close with each other. For flexural wave with large wave numbers, it seems that the local model's results are better. However, both models are still very close with MD simulations, and the small difference can be attribute to the computational errors. We also compare our longitudinal results with analytical solutions given by Wang [85]. Overall, the non-local model shows some advantage on wave propagation problems in (25,0) zigzag tube, but it requires further verification.

5.4 Summary

In this chapter, a potential-oriented non-local finite element shell model is established specially for CNTs. Based on the same methodology as the previous chapter, the elastic constants of CNT are directly calculated from the inter-atomic potential. Again the natural frequencies of various CNTs are calculated by both local and non-local models. The effects of the boundary correction and the non-local elasticity are also discussed. Moreover, the wave propagation dispersion relations of are simulated. With the same non-local parameter we used for graphene in Chapter 4, results show that the non-local shell model has a better dynamic performance than the local one under some circumstances, but further investigation is required.

Chapter 6

Conclusions

Through the efforts of the author, non-local plate and shell solutions for CNT and graphene are established. Firstly, a semi-analytical optimization model for calculations about the equilibrium configuration of SWCNT is derived. It is shown that this model can reproduce the results from corresponding atomic simulations and the computational cost in negligible. Furthermore, the semi-analytical approach is extended for the calculation of the RBM frequencies of CNTs. Secondly, the non-local plate model of single-layer graphene sheet is developed. The effect of boundary and boundary condition inconsistency on the static and dynamic behavior of SLGS can be alleviated by extending SLGS's dimensions at the clamped boundaries by a small amount L_m. It is also demonstrated that L_m controls the constant component of the error and the non-local parameter e_0a controls the error proportionality with respect to the wavelength of deformation. Contrary to the case dependent non-local parameter values used in the literature, the optimal non-local parameter e_0a is independent of size, shape and vibration pattern of the SLGS. Finally, by using potential-based bending rigidity, we found that a combination of $L_m = 0.03$ nm and $e_0a = 0.05$ nm gives accurate results for static and dynamic behavior of SLGS. And in the end, a non-local shell model is built for continuum simulations of SWCNT.

6.1 Answers to the research questions

1. Why are there so many non-local parameters employed in literature? What factors can affect this number?

   The reason is because in most of these studies, their local models are not accurate. The non-local parameter should only be affected by the characteristic length of the lattice. However, a lot of other factors can contribute to the error of the continuum model. Because these factors are case-dependent, people can obtain completely different non-local parameters when they try to fit their results.

2. So far, most non-local parameters are obtained by fitting with atomic simulations. If these affecting factors are determined, is there a way to predict the non-local parameter without running atomic simulations?

   There is no need to predict the non-local parameter. For the same lattice, there should be only one non-local parameter. From our simulation results, this number should be around 0.05 nm for graphene and CNT.

3. It is shown that the non-local parameter can reduce the error of dynamic simulations on graphene and CNT. But where are these errors from? A lot of non-local models employed constitutive relations of traditional continuum materials, which has already been proven to be wrong. Is it a robust way that using the non-local model to fix errors which may caused by improper constitutive relations?

   Basically there are three major sources of errors. The first one is the constitutive relations. But with potential-oriented elastic constants, this error can be significantly reduced. The second type is improper boundary conditions. For the clamped boundary condition, a small boundary correction factor can greatly reduce the error. The last one is from the discrete atom lattice which can be improved by the non-local

model. Different types of errors require different strategies to deal with.

6.2 Future work

Future researches can focus on analytical solutions of both potential-oriented non-local plate and shell models of graphene and CNT. The finite element models still contain some errors, and with analytical solutions the non-local parameter can be accurately calibrated. Also the boundary conditions of graphene and CNT need more researches. The boundary correction factor is a simple but not accurate method to reduce the current error. And this factor is dependent on size and shape, which is not ideal. A well-defined boundary should be size and shape independent, which can also mimic the deformation of atomic lattice near the boundary.

To the application point of view, this shell model can be applied to any 2D carbon allotropes. The major methodology of this dissertation is not limited to flat and cylindrical surfaces. Examples are like carbon nano-cone, carbon nano-scrolls, rebar graphene (shown in Fig. (6.1)) [72], graphene-CNT hybrid materials, etc. Those structure can all benefit from our continuum shell model.

Figure 6.1: Structure of rebar graphene [72]

Appendices

Appendix A Bond angle calculation

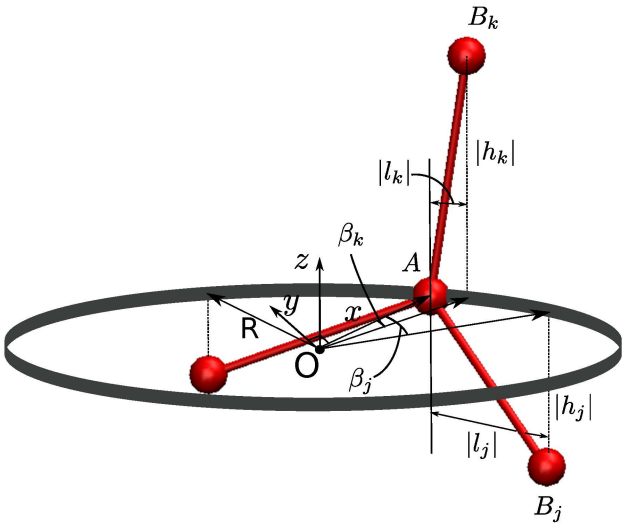

Figure 2: Bond angle calculation

A Cartesian coordinate system with the origin at the center of the circular cross-section is defined as shown in Fig. 2. Since the points A, B_j, B_k are all on the same cylindrical surface, $\overrightarrow{OA}$, $\overrightarrow{OB_j}$ and $\overrightarrow{OB_k}$ can be expressed as:

$$\begin{aligned} &\overrightarrow{OA} = \{R, 0, 0\} \\ &\overrightarrow{OB_j} = \{R\cos\beta_j, R\sin\beta_j, h_j\} \qquad \begin{matrix} j \neq k \\ j,k = 1,2,3 \end{matrix} \\ &\overrightarrow{OB_k} = \{R\cos\beta_k, R\sin\beta_k, h_k\} \end{aligned} \tag{1}$$

Therefore,

$$\begin{aligned} &\overrightarrow{AB_j} = \{R(\cos\beta_j - 1), R\sin\beta_j, h_j\} \\ &\overrightarrow{AB_k} = \{R(\cos\beta_k - 1), R\sin\beta_k, h_k\} \end{aligned} \tag{2}$$

We obtain

$$\begin{aligned}\cos \angle B_j A B_k &= \frac{\overrightarrow{AB_j} \cdot \overrightarrow{AB_k}}{|\overrightarrow{AB_j}||\overrightarrow{AB_k}|} \\ &= \frac{R^2(\cos\beta_j - 1)(\cos\beta_k - 1) + R^2 \sin\beta_j \sin\beta_k + h_j h_k}{r_j r_k}\end{aligned} \tag{3}$$

Recalling Eq. (3.2), we have

$$\begin{aligned}1 - \cos\beta_j &= 2sin^2(\frac{\beta_j}{2}) = 2\frac{l_j^2}{4R^2} \\ \sin\beta_j &= 2sin(\frac{\beta_j}{2})\cos(\frac{\beta_j}{2}) = 2\frac{l_j}{2R}\sqrt{1 - \frac{l_j^2}{4R^2}}\end{aligned} \tag{4}$$

Substituting Eq. (4) with $h_j = r_j|\sin(\alpha_j)|$ and $l_j = r_j|\cos(\alpha_j)|$ into Eq. (3), we have

$$\begin{aligned}\cos \angle B_j A B_k &= \frac{1}{r_j r_k}\left\{4R^2\frac{l_j^2}{4R^2}\frac{l_k^2}{4R^2} + 4R^2\left(\frac{l_j}{2R}\sqrt{1 - \frac{l_j^2}{4R^2}}\right)\left(\frac{l_k}{2R}\sqrt{1 - \frac{l_k^2}{4R^2}}\right) + h_j h_k\right\} \\ &= \frac{r_j r_k}{4R^2}\cos^2\alpha_j \cos^2\alpha_k + \cos\alpha_j \cos\alpha_k \sqrt{1 - \frac{r_j^2\cos^2\alpha_j}{4R^2}}\sqrt{1 - \frac{r_k^2\cos^2\alpha_k}{4R^2}} \\ &\quad + \sin\alpha_j \sin\alpha_k\end{aligned} \tag{5}$$

Appendix B Geometry differentiation in 2D carbon lattice with respect to atom coordinates

Denote $x_{m\alpha},\ \alpha = 1, 2, 3$ to represent the coordinate of atom m in x, y or z direction. Then the distance between atoms i and j, r_{ij}, and the angle between bond $i - j$ and bond $i - k$ can be expressed as:

$$\begin{aligned} r_{ij} &= \left[\sum_{\alpha=1}^{3}(x_{j\alpha} - x_{i\alpha})^2\right]^{\frac{1}{2}} \\ \cos_{ijk} &= \frac{1}{r_{ij}r_{ik}}\left[\sum_{\alpha=1}^{3}(x_{j\alpha} - x_{i\alpha})(x_{k\alpha} - x_{i\alpha})\right] \end{aligned} \tag{6}$$

And it's obvious that $\frac{\partial}{\partial x_{m\alpha}} = \frac{\partial}{\partial u_{m\alpha}}$, then we have

$$\begin{aligned} &\frac{\partial r_{ij}}{\partial u_{i\alpha}} = -\frac{1}{r_{ij}}(x_{j\alpha} - x_{i\alpha}) \\ &\frac{\partial r_{ij}}{\partial u_{j\alpha}} = \frac{1}{r_{ij}}(x_{j\alpha} - x_{i\alpha}) \\ &\frac{\partial \cos_{ijk}}{\partial u_{j\alpha}} = \frac{x_{k\alpha} - x_{i\alpha}}{r_{ij}r_{ik}} - \frac{\cos_{ijk}}{r_{ij}}\frac{\partial r_{ij}}{\partial u_{j\alpha}} \\ &\frac{\partial \cos_{ijk}}{\partial u_{i\alpha}} = -\frac{(x_{j\alpha} - x_{i\alpha}) + (x_{k\alpha} - x_{i\alpha})}{r_{ij}r_{ik}} - \cos_{ijk}\left(\frac{1}{r_{ij}}\frac{\partial r_{ij}}{\partial u_{i\alpha}} + \frac{1}{r_{ik}}\frac{\partial r_{ik}}{\partial u_{i\alpha}}\right) \end{aligned} \tag{7}$$

$\frac{\partial \cos_{ijk}}{\partial u_{k\alpha}}$ can be obtained from $\frac{\partial \cos_{ijk}}{\partial u_{j\alpha}}$ by exchanging j and k. Then the 2nd order derivatives of r_{ij} is as follows:

$$\frac{\partial^2 r_{ij}}{\partial u_{m\alpha}\partial u_{n\beta}} = (-1)^{\delta_{mn}}\left[\delta_{\alpha\beta}\frac{1}{r_{ij}} - \frac{(x_{j\alpha} - x_{i\alpha})^2}{r_{ij}^3}\right] \tag{8}$$

Where m and n can be either i or j. δ represents the Kronecker delta. And the correspon-

ding derivatives of $\cos_{ijk}$ are:

$$\begin{aligned}
\frac{\partial^2 \cos_{ijk}}{\partial u_{i\alpha}\partial u_{i\beta}} &= -\cos_{ijk}\left[\frac{\partial^2 r_{ij}}{\partial u_{i\alpha}\partial u_{i\beta}}\frac{1}{r_{ij}} - \frac{\partial r_{ij}}{\partial u_{i\alpha}}\frac{\partial r_{ij}}{\partial u_{i\beta}}\frac{1}{r_{ij}^2} + \frac{\partial^2 r_{ik}}{\partial u_{i\alpha}\partial u_{i\beta}}\frac{1}{r_{ik}} - \frac{\partial r_{ik}}{\partial u_{i\alpha}}\frac{\partial r_{ik}}{\partial u_{i\beta}}\frac{1}{r_{ik}^2}\right] \\
&\quad + \frac{2\delta_{\alpha\beta}}{r_{ij}r_{ik}} + \frac{x_{j\alpha}+x_{k\alpha}-2x_{i\alpha}}{r_{ij}r_{ik}}A_{jk,\beta} - \frac{\partial \cos_{ijk}}{\partial u_{i\beta}}A_{jk,\alpha} \\
\frac{\partial^2 \cos_{ijk}}{\partial u_{i\alpha}\partial u_{j\beta}} &= \frac{x_{j\alpha}+x_{k\alpha}-2x_{i\alpha}}{r_{ij}^2 r_{ik}}\frac{\partial r_{ij}}{\partial u_{j\beta}} - \frac{\cos_{ijk}}{r_{ij}}\left[\frac{\partial^2 r_{ij}}{\partial u_{i\alpha}\partial u_{j\beta}} - \frac{1}{r_{ij}}\frac{\partial r_{ij}}{\partial u_{i\alpha}}\frac{\partial r_{ij}}{\partial u_{j\beta}}\right] \\
&\quad - \frac{\partial \cos_{ijk}}{\partial u_{j\beta}}A_{jk,\alpha} - \frac{\delta_{\alpha\beta}}{r_{ij}r_{ik}} \\
\frac{\partial^2 \cos_{ijk}}{\partial u_{j\alpha}\partial u_{j\beta}} &= -\frac{x_{k\alpha}-x_{i\alpha}}{r_{ij}^2 r_{ik}}\frac{\partial r_{ij}}{\partial u_{j\beta}} - \frac{1}{r_{ij}}\frac{\partial r_{ij}}{\partial u_{j\alpha}}\frac{\partial \cos_{ijk}}{\partial u_{j\beta}} - \frac{\cos_{ijk}}{r_{ij}}\left(\frac{\partial^2 r_{ij}}{\partial u_{j\alpha}\partial u_{j\beta}} - \frac{1}{r_{ij}}\frac{\partial r_{ij}}{\partial u_{j\alpha}}\frac{\partial r_{ij}}{\partial u_{j\beta}}\right) \\
\frac{\partial^2 \cos_{ijk}}{\partial u_{j\alpha}\partial u_{k\beta}} &= -\frac{x_{k\alpha}-x_{i\alpha}}{r_{ij}r_{ik}^2}\frac{\partial r_{ik}}{\partial u_{k\beta}} - \frac{1}{r_{ij}}\frac{\partial r_{ij}}{\partial u_{j\alpha}}\frac{\partial \cos_{ijk}}{\partial u_{k\beta}} - \frac{1}{r_{ij}r_{ik}}
\end{aligned} \tag{9}$$

Where

$$A_{jk,\alpha} = \frac{1}{r_{ij}}\frac{\partial r_{ij}}{\partial u_{i\alpha}} + \frac{1}{r_{ik}}\frac{\partial r_{ik}}{\partial u_{i\alpha}} \tag{10}$$

Appendix C Second generation Brenner (REBO) potential and differentiations

The expression of 2nd generation Brenner potential [11] is:

$$W = \frac{1}{2}\sum_{i,j,i\neq j} V_{ij} = \frac{1}{2}\sum_{i,j,i\neq j}\left[V_R(r_{ij}) - \bar{b}_{ij}V_A(r_{ij})\right] \tag{11}$$

where

$$\begin{aligned} V_R(r) &= \left(1+\frac{Q}{r}\right)Ae^{-\alpha r}f_c(r) \\ V_A(r) &= \sum_{n=1}^{3} B_n e^{-\beta_n r} f_c(r) \\ b_{ij} &= \left[1+\sum_{k}^{k\neq j} G(\cos\theta_{ijk}) f_c(r_{ik})\right]^{-\frac{1}{2}} \\ \bar{b}_{ij} &= \frac{1}{2}(b_{ij}+b_{ji}) \end{aligned} \tag{12}$$

and

$$f_c(r) = \begin{cases} 1 & r < R_1, \\ \frac{1}{2}\left\{1 + \cos\left[\frac{\pi(r-R_1)}{R_2-R_1}\right]\right\} & R_1 \le r \le R_2, \\ 0 & r > R_2, \end{cases}$$

$$G = \begin{cases} 0.27186 - 0.48922\cos\theta - 0.43286\cos^2\theta - 0.56140\cos^3\theta \\ \qquad + 1.2711\cos^4\theta - 0.037931\cos^5\theta & \theta < 109.47^\circ, \\ 0.69669 + 5.5444\cos\theta + 23.432\cos^2\theta + 55.948\cos^3\theta \\ \qquad + 69.876\cos^4\theta + 35.312\cos^5\theta & 109.47^\circ \le \theta \le 120^\circ, \\ 0.00260 - 1.0980\cos\theta - 4.3460\cos^2\theta \\ \qquad - 6.8300\cos^3\theta - 4.9280\cos^4\theta - 1.3424\cos^5\theta & \theta > 120^\circ, \end{cases} \tag{13}$$

Table 1: Parameters for V_R and V_A

A	10953.5 eV	α	4.74654 Å^{-1}	Q	0.313460 Å
B_1	12388.8 eV	β_1	4.72045 Å^{-1}	$R^{(1)}$	1.7 Å
B_2	17.5675 eV	β_2	1.43321 Å^{-1}	$R^{(2)}$	2.0 Å
B_3	30.7149 eV	β_3	1.38269 Å^{-1}		

Parameters are listed in table 1. The derivatives of V_R, V_A,b_{ij} and $f_c(r)$ in Eq. (4.9)

are:

$$
\begin{aligned}
\frac{dV_R}{dr} &= Ae^{-\alpha r}\left\{\left(1+\frac{Q}{r}\right)\frac{df_c}{dr}(r) - \left[\alpha\left(1+\frac{Q}{r}\right)+\frac{Q}{r^2}\right]f_c(r)\right\} \\
\frac{dV_A}{dr} &= \sum_{n=1}^{3} B_n e^{-\beta_n r}\left(\frac{df_c}{dr}(r) - \beta_n f_c(r)\right) \\
\frac{\partial b_{ij}}{\partial r_{ik}} &= -\frac{1}{2}\left[1+\sum_{l\neq k} G(\cos\theta_{ijl}) f_c(r_{il})\right]^{-\frac{3}{2}} G(\cos\theta_{ijk})\frac{df_c}{dr}(r_{ik}) \\
&= -\frac{1}{2} b_{ij}^3 G(\cos\theta_{ijk})\frac{df_c}{dr}(r_{ik}) \\
\frac{\partial b_{ij}}{\partial \cos\theta_{ijk}} &= -\frac{1}{2} b_{ij}^3 \frac{dG}{d\cos\theta}(\cos\theta_{ikj}) f_c(r_{ik})
\end{aligned}
\tag{14}
$$

Where

$$
\frac{df_c}{dr} = \begin{cases} 0 & r < R^{(1)}, \\ -\dfrac{\pi}{2(R^{(2)}-R^{(1)})}\sin\left[\dfrac{\pi(r-R^{(1)})}{R^{(2)}-R^{(1)}}\right] & R^{(1)} \le r \le R^{(2)}, \\ 0 & r > R^{(2)}, \end{cases} \tag{15}
$$

and

$$
\frac{dG(\cos\theta)}{d\cos\theta} = \begin{cases} 0.48922 - 0.86572\cos\theta - 1.68420\cos^2\theta & \\ \qquad + 5.0844\cos^3\theta - 0.189655\cos^4\theta & \theta < 109.47^\circ, \\ 5.5444 + 46.864\cos\theta + 167.844\cos^2\theta & \\ \qquad + 279.504\cos^3\theta + 176.560\cos^4\theta & 109.47^\circ \le \theta \le 120^\circ, \\ -1.0980 - 8.6920\cos\theta - 20.4900\cos^2\theta & \\ \qquad - 19.7120\cos^3\theta - 6.7120\cos^4\theta & \theta > 120^\circ, \end{cases} \tag{16}
$$

And the 2nd order derivatives are:

$$\begin{aligned}
\frac{d^2V_R}{dr^2} &= Ae^{-\alpha r}\left\{\frac{2Q}{r^2}\left[\left(\frac{1}{r}+\alpha\right)f_c(r) - \frac{df_c}{dr}(r)\right]\right. \\
&\quad \left. + \left(1+\frac{Q}{r}\right)\left(\alpha^2 f_c(r) - 2\alpha\frac{df_c}{dr}(r) + \frac{d^2f_c}{dr^2}(r)\right)\right\} \\
\frac{d^2V_A}{dr^2} &= \sum_{n=1}^{3} B_n e^{-\beta_n r}\left(\frac{d^2f_c}{dr^2}(r) - 2\beta_n\frac{df_c}{dr}(r) + \beta_n^2 f_c(r)\right) \\
\frac{\partial^2 b_{ij}}{\partial r_{im}\partial r_{in}} &= \frac{3}{4}G(\cos\theta_{ijm})G(\cos\theta_{ijn})\frac{df_c}{dr}(r_{im})\frac{df_c}{dr}(r_{in})b_{ij}^5 \\
&\quad - \frac{\delta_{mn}}{2}G(\cos\theta_{ijm})\frac{d^2f_c}{dr^2}(r_{im})b_{ij}^3 \\
\frac{\partial^2 b_{ij}}{\partial r_{im}\partial\cos\theta_{ijn}} &= \frac{3}{4}G(\cos\theta_{ijm})\frac{dG}{d\cos\theta}(\cos\theta_{ijn})\frac{df_c}{dr}(r_{im})f_c(r_{in})b_{ij}^5 \\
&\quad - \frac{\delta_{mn}}{2}\frac{df_c}{dr}(r_{im})\frac{dG}{d\cos\theta}(\cos\theta_{ijm})b_{ij}^3 \\
\frac{\partial^2 b_{ij}}{\partial\cos\theta_{ijm}\partial\cos\theta_{ijn}} &= \frac{3}{4}\frac{dG}{d\cos\theta}(\cos\theta_{ijm})\frac{dG}{d\cos\theta}(\cos\theta_{ijn})f_c(r_{im})f_c(r_{in})b_{ij}^5 \\
&\quad - \frac{\delta_{mn}}{2}\frac{d^2G}{d\cos\theta^2}(\cos\theta_{ijm})f_c(r_{im})b_{ij}^3
\end{aligned} \tag{17}$$

Where

$$\frac{d^2f_c}{dr^2} = \begin{cases} 0 & r < R^{(1)}, \\ -\dfrac{\pi^2}{2(R^{(2)}-R^{(1)})^2}\cos\left[\dfrac{\pi(r-R^{(1)})}{R^{(2)}-R^{(1)}}\right] & R^{(1)} \le r \le R^{(2)}, \\ 0 & r > R^{(2)}, \end{cases} \tag{18}$$

and

$$\frac{d^2G(\cos\theta)}{d\cos^2\theta} = \begin{cases} -0.86572 - 3.36840\cos\theta + 15.2532\cos^2\theta - .758620\cos^3\theta & \theta < 109.47^\circ, \\ 46.864 + 335.688\cos\theta + 838.512\cos^2\theta + 706.240\cos^3\theta & 109.47^\circ \le \theta \le 120^\circ, \\ -8.6920 - 40.9800\cos\theta - 59.1360\cos^2\theta - 26.8480\cos^3\theta & \theta > 120^\circ, \end{cases} \tag{19}$$

Appendix D Differentiation of r_{ij} and $\cos\theta_{ijk}$ with respect to strains and curvatures

From Eq. (5.30), we can deduce the derivatives of r_{ij} and $\cos\theta_{ijk}$. We define some terms to make our formulas less redundant.

Vectors:

$$
\begin{aligned}
v_\alpha &= (\Delta\xi_\gamma^{ij} B_{\gamma\lambda} \Delta\xi_\lambda^{ij})^2 \Delta\xi_\gamma^{ij} B_{\gamma\lambda} \\
C_\alpha^e &= \frac{1}{r_{ij}} \frac{\partial r_{ij}}{\partial \eta_\alpha} + \frac{1}{r_{ik}} \frac{\partial r_{ik}}{\partial \eta_\alpha} \\
C_\alpha^d &= \frac{1}{r_{ij} r_{ik}} A_{\alpha\beta} \left(\Delta\xi_\beta^{ij} + \Delta\xi_\beta^{ik} \right) + \frac{1}{12} \Big\{ B_{\alpha\beta} \widetilde{T}_{\beta\gamma} B_{\gamma\lambda} \left(\Delta\xi_\lambda^{ij} + \Delta\xi_\lambda^{ik} \right) \\
&\quad + \Delta\xi_\beta^{ij} \left[B_{\beta\alpha} \left(\Delta\xi_\gamma^{ik} - 2\Delta\xi_\gamma^{ij} \right) B_{\gamma\lambda} + B_{\beta\gamma} \left(\Delta\xi_\gamma^{ij} - 2\Delta\xi_\gamma^{ik} \right) B_{\alpha\lambda} \right] \Delta\xi_\lambda^{ik} \Big\}
\end{aligned}
\tag{20}
$$

Tensors:

$$
\begin{aligned}
T_{\alpha\beta}^{jk} &= \Delta\xi_\alpha^{ij} \Delta\xi_\beta^{ik} \\
\widetilde{T}_{\alpha\beta} &= 3T_{\alpha\beta}^{jk} - 2T_{\alpha\beta}^{jj} - 2T_{\alpha\beta}^{kk}\,, \qquad j \neq k \\
C_{\alpha\beta}^E &= \frac{1}{r_{ij}} \frac{\partial r_{ij}}{\partial E_{\alpha\beta}} + \frac{1}{r_{ik}} \frac{\partial r_{ik}}{\partial E_{\alpha\beta}} \\
C_{\alpha\beta}^K &= \frac{1}{r_{ij}} \frac{\partial r_{ij}}{\partial K_{\alpha\beta}} + \frac{1}{r_{ik}} \frac{\partial r_{ik}}{\partial K_{\alpha\beta}}
\end{aligned}
\tag{21}
$$

Note that all the following derivatives are evaluated at the equilibrium position ($E_{\alpha\beta} = 0$, $K_{\alpha\beta} = 0$ and $\eta_\alpha = 0$).

First order derivatives:

$$
\begin{aligned}
&\frac{\partial r_{ij}}{\partial E_{\alpha\beta}} = \frac{T^{jj}_{\alpha\beta}}{r_{ij}} \\
&\frac{\partial r_{ij}}{\partial K_{\alpha\beta}} = -\frac{1}{12}\frac{1}{r_{ij}} T^{jj}_{\gamma\lambda} B_{\gamma\lambda} T_{\alpha\beta} \\
&\frac{\partial r_{ij}}{\partial \eta_{\alpha}} = \frac{1}{r_{ij}} \left(A_{\alpha\beta}\Delta\xi^{ij}_{\beta} - \frac{1}{6} T^{jj}_{\gamma\lambda} B_{\gamma\lambda} B_{\alpha\beta} \Delta\xi^{ij}_{\beta} \right) \\
&\frac{\partial \cos\theta_{ijk}}{\partial E_{\alpha\beta}} = -C^{E}_{\alpha\beta}\cos\theta_{ijk} + \frac{2T^{jk}_{\alpha\beta}}{r_{ij}r_{ik}} \\
&\frac{\partial \cos\theta_{ijk}}{\partial K_{\alpha\beta}} = -C^{K}_{\alpha\beta}\cos\theta_{ijk} - \frac{1}{12}\frac{1}{r_{ij}r_{ik}} \left(\Delta\xi^{ij}_{\alpha} \widetilde{T}_{\beta\gamma} B_{\gamma\lambda} \Delta\xi^{ik}_{\lambda} + \Delta\xi^{ij}_{\gamma} B_{\gamma\lambda} \widetilde{T}_{\lambda\alpha} \Delta\xi^{ik}_{\beta} \right) \\
&\frac{\partial \cos\theta_{ijk}}{\partial \eta_{\alpha}} = -C^{e}_{\alpha}\cos\theta_{ijk} + C^{d}_{\alpha}
\end{aligned}
\tag{22}
$$

Second order derivatives of r_{ij}:

$$
\begin{aligned}
&\frac{\partial^2 r_{ij}}{\partial E_{\alpha\beta}\partial E_{\gamma\lambda}} = -\frac{T^{jj}_{\alpha\beta} T^{jj}_{\gamma\lambda}}{r^3_{ij}} \\
&\frac{\partial^2 r_{ij}}{\partial K_{\alpha\beta}\partial K_{\gamma\lambda}} = -\left[\frac{1}{144}\frac{1}{r^3_{ij}} \left(B_{\nu\mu} T^{jj}_{\nu\mu} \right)^2 + \frac{1}{12}\frac{1}{r_{ij}} \right] T^{jj}_{\alpha\beta} T^{jj}_{\gamma\lambda} \\
&\frac{\partial^2 r_{ij}}{\partial \eta_{\alpha}\partial \eta_{\beta}} = \frac{1}{r_{ij}} \left[\frac{\partial r_{ij}}{\partial \eta_{\alpha}} \frac{\partial r_{ij}}{\partial \eta_{\beta}} + A_{\alpha\beta} - \frac{1}{6} \left(2\Delta\xi^{ij}_{\gamma} B_{\gamma\alpha} B_{\beta\lambda} \Delta\xi^{ij}_{\lambda} + B_{\gamma\lambda} T^{jj}_{\gamma\lambda} B_{\alpha\beta} \right) \right] \\
&\frac{\partial^2 r_{ij}}{\partial E_{\alpha\beta}\partial \eta_{\gamma}} = \frac{1}{r_{ij}} \left(-\frac{\partial r}{\partial E_{\alpha\beta}} \frac{\partial r}{\partial \eta_{\gamma}} + \delta_{\alpha\gamma}\Delta\xi^{ij}_{\beta} + \delta_{\beta\gamma}\Delta\xi^{ij}_{\alpha} \right) \\
&\frac{\partial^2 r_{ij}}{\partial K_{\alpha\beta}\partial \eta_{\gamma}} = \frac{1}{r_{ij}} \left[-\frac{\partial r}{\partial K_{\alpha\beta}} \frac{\partial r}{\partial \eta_{\gamma}} - \frac{1}{6} T^{jj}_{\alpha\beta} B_{\gamma\lambda} \Delta\xi^{ij}_{\lambda} + \frac{1}{2} T^{jj}_{\lambda\nu} B_{\lambda\nu} \left(\delta_{\alpha\gamma}\Delta\xi^{ij}_{\beta} + \delta_{\beta\gamma}\Delta\xi^{ij}_{\alpha} \right) \right] \\
&\frac{\partial^2 r_{ij}}{\partial E_{\alpha\beta}\partial K_{\gamma\lambda}} = \frac{1}{12}\frac{1}{r^3_{ij}} T^{jj}_{\nu\mu} B_{\nu\mu} T^{jj}_{\alpha\beta} T^{jj}_{\gamma\lambda}
\end{aligned}
\tag{23}
$$

Second order derivatives of $\cos_{ijk}$:

$$
\begin{aligned}
&\frac{\partial^2 \cos\theta_{ijk}}{\partial E_{\alpha\beta}\partial E_{\gamma\lambda}} = r_{ij}r_{ik}\frac{\partial^2[1/(r_{ij}r_{ik})]}{\partial E_{\alpha\beta}\partial E_{\gamma\lambda}}\cos\theta_{ijk} - C^E_{\alpha\beta}\frac{\partial \cos\theta_{ijk}}{\partial E_{\gamma\lambda}} - \frac{2}{r_{ij}r_{ik}}T^{jk}_{\alpha\beta}C^E_{\gamma\lambda} \\
&\frac{\partial^2 \cos\theta_{ijk}}{\partial K_{\alpha\beta}\partial K_{\gamma\lambda}} = r_{ij}r_{ik}\frac{\partial^2[1/(r_{ij}r_{ik})]}{\partial K_{\alpha\beta}\partial K_{\gamma\lambda}}\cos\theta_{ijk} - C^K_{\alpha\beta}\frac{\partial \cos\theta_{ijk}}{\partial K_{\gamma\lambda}} + \frac{1}{12}\frac{1}{r_{ij}r_{ik}}\cdot \\
&\qquad \left[-\left(\Delta\xi^{ij}_{\alpha}\widetilde{T}_{\beta\nu}B_{\nu\mu}\Delta\xi^{ik}_{\mu} + \Delta\xi^{ij}_{\nu}B_{\nu\mu}\widetilde{T}_{\mu\alpha}\Delta\xi^{ik}_{\beta}\right)C^K_{\gamma\lambda} + \Delta\xi^{ij}_{\alpha}\widetilde{T}_{\beta\gamma}\Delta\xi^{ik}_{\lambda} + \Delta\xi^{ij}_{\gamma}\widetilde{T}_{\lambda\alpha}\Delta\xi^{ik}_{\beta}\right] \\
&\frac{\partial^2 \cos\theta_{ijk}}{\partial \eta_{\alpha}\partial \eta_{\beta}} = r_{ij}r_{ik}\frac{\partial^2[1/(r_{ij}r_{ik})]}{\partial \eta_{\alpha}\partial \eta_{\beta}}\cos\theta_{ijk} - \frac{\partial \cos\theta_{ijk}}{\partial \eta_{\alpha}}C^e_{\beta} - C^e_{\alpha}C^d_{\beta} \\
&\qquad + \frac{1}{r_{ij}r_{ik}}\left\{2A_{\alpha\beta} + \frac{1}{12}\left[2B_{\alpha\gamma}\widetilde{T}_{\beta\gamma}B_{\gamma\beta} + 2B_{\alpha\beta}\left(\Delta\xi^{ik}_{\gamma} - 2\Delta\xi^{ij}_{\gamma}\right)B_{\gamma\lambda}\Delta\xi^{ik}_{\lambda}\right.\right. \\
&\qquad + B_{\alpha\gamma}\left(\Delta\xi^{ij}_{\gamma} - 2\Delta\xi^{ik}_{\gamma}\right)B_{\beta\lambda}\left(\Delta\xi^{ij}_{\lambda} + \Delta\xi^{ik}_{\lambda}\right) + 2\Delta\xi^{ij}_{\gamma}B_{\gamma\lambda}\left(\Delta\xi^{ij}_{\lambda} - 2\Delta\xi^{ik}_{\lambda}\right)B_{\alpha\beta} \\
&\qquad \left.\left. + \left(\Delta\xi^{ij}_{\gamma} + \Delta\xi^{ik}_{\gamma}\right)B_{\gamma\alpha}\left(\Delta\xi^{ik}_{\lambda} - 2\Delta\xi^{ij}_{\lambda}\right)B_{\lambda\beta}\right]\right\} \\
&\frac{\partial^2 \cos\theta_{ijk}}{\partial E_{\alpha\beta}\partial \eta_{\gamma}} = r_{ij}r_{ik}\frac{\partial^2[1/(r_{ij}r_{ik})]}{\partial E_{\alpha\beta}\partial \eta_{\gamma}}\cos\theta_{ijk} - \frac{\partial \cos\theta_{ijk}}{\partial E_{\alpha\beta}}C^e_{\gamma} - C^E_{\alpha\beta}C^d_{\gamma} \\
&\qquad + \frac{2}{r_{ij}r_{ik}}\left(\delta_{\alpha\gamma}\Delta\xi^{ik}_{\beta} + \Delta\xi^{ij}_{\alpha}\delta_{\beta\gamma}\right) \\
&\frac{\partial^2 \cos\theta_{ijk}}{\partial K_{\alpha\beta}\partial \eta_{\gamma}} = r_{ij}r_{ik}\frac{\partial^2[1/(r_{ij}r_{ik})]}{\partial K_{\alpha\beta}\partial \eta_{\gamma}}\cos\theta_{ijk} - \frac{\partial \cos\theta_{ijk}}{\partial K_{\alpha\beta}}C^e_{\gamma} - C^K_{\alpha\beta}C^d_{\gamma} \\
&\qquad + \frac{1}{12}\frac{1}{r_{ij}r_{ik}}\left[\delta_{\alpha\gamma}\widetilde{T}_{\gamma\lambda}B_{\lambda\nu}\Delta\xi^{ik}_{\nu} + \Delta\xi^{ij}_{\lambda}B_{\lambda\nu}\widetilde{T}_{\nu\alpha}\delta_{\beta\gamma} + B_{\gamma\lambda}\widetilde{T}_{\lambda\alpha}\Delta\xi^{ik}_{\beta} + \Delta\xi^{ij}_{\alpha}\widetilde{T}_{\beta\lambda}B_{\lambda\gamma}\right. \\
&\qquad + \Delta\xi^{ij}_{\alpha}\delta_{\beta\gamma}\left(\Delta\xi^{ik}_{\lambda} - 2\Delta\xi^{ij}_{\lambda}\right)B_{\lambda\mu}\Delta\xi^{ik}_{\mu} + \Delta\xi^{ij}_{\alpha}\left(\Delta\xi^{ij}_{\beta} - 2\Delta\xi^{ik}_{\beta}\right)B_{\gamma\lambda}\Delta\xi^{ik}_{\lambda} \\
&\qquad \left. + \Delta\xi^{ik}_{\beta}B_{\alpha\lambda}\Delta\xi^{ij}_{\lambda}\left(\Delta\xi^{ik}_{\gamma} - 2\Delta\xi^{ij}_{\gamma}\right) + \Delta\xi^{ik}_{\beta}\delta_{\alpha\gamma}\Delta\xi^{ij}_{\lambda}B_{\lambda\mu}\left(\Delta\xi^{ij}_{\mu} - 2\Delta\xi^{ik}_{\mu}\right)\right] \\
&\frac{\partial^2 \cos\theta_{ijk}}{\partial E_{\alpha\beta}\partial K_{\gamma\lambda}} = r_{ij}r_{ik}\frac{\partial^2[1/(r_{ij}r_{ik})]}{\partial E_{\alpha\beta}\partial K_{\gamma\lambda}}\cos\theta_{ijk} - C^E_{\alpha\beta}\frac{\partial \cos\theta_{ijk}}{\partial K_{\gamma\lambda}} - \frac{2}{r_{ij}r_{ik}}T^{jk}_{\alpha\beta}C^K_{\gamma\lambda}
\end{aligned}
\tag{24}
$$

where

$$
r_{ij}r_{ik}\frac{\partial^2[1/(r_{ij}r_{ik})]}{\partial a \partial b} = -\frac{1}{r_{ij}}\frac{\partial^2 r_{ij}}{\partial a \partial b} + \frac{1}{r^2_{ij}}\frac{\partial r_{ij}}{\partial a}\frac{\partial r_{ij}}{\partial b} - \frac{1}{r_{ik}}\frac{\partial^2 r_{ik}}{\partial a \partial b} + \frac{1}{r^2_{ik}}\frac{\partial r_{ik}}{\partial a}\frac{\partial r_{ik}}{\partial b} \tag{25}
$$

a, b can be $E_{\alpha\beta}$, $K_{\alpha\beta}$ or η_{α}.

Bibliography

[1] DJ Allman. A compatible triangular element including vertex rotations for plane elasticity analysis. *Computers & Structures*, 19(1-2):1–8, 1984.

[2] R Ansari, R Rajabiehfard, and B Arash. Nonlocal finite element model for vibrations of embedded multi-layered graphene sheets. *Computational Materials Science*, 49(4):831–838, 2010.

[3] R Ansari, S Sahmani, and B Arash. Nonlocal plate model for free vibrations of single-layered graphene sheets. *Physics Letters A*, 375(1):53–62, 2010.

[4] B Arash and R Ansari. Evaluation of nonlocal parameter in the vibrations of single-walled carbon nanotubes with initial strain. *Physica E: Low-dimensional Systems and Nanostructures*, 42(8):2058–2064, 2010.

[5] B Arash, Q Wang, and Kim Meow Liew. Wave propagation in graphene sheets with nonlocal elastic theory via finite element formulation. *Computer Methods in Applied Mechanics and Engineering*, 223:1–9, 2012.

[6] Behrouz Arash and Quan Wang. Vibration of single-and double-layered graphene sheets. *Journal of Nanotechnology in Engineering and Medicine*, 2(1):011012, 2011.

[7] Marino Arroyo and Ted Belytschko. Finite crystal elasticity of carbon nanotubes based on the exponential cauchy-born rule. *Physical Review B*, 69(11):115415, 2004.

[8] Harm Askes, Andrei V Metrikine, Aleksey V Pichugin, and Terry Bennett. Four simplified gradient elasticity models for the simulation of dispersive wave propagation. *Philosophical magazine*, 88(28-29):3415–3443, 2008.

[9] T Belytschko, SP Xiao, GC Schatz, and RS Ruoff. Atomistic simulations of nanotube fracture. *Physical Review B*, 65(23):235430, 2002.

[10] Donald W Brenner. Empirical potential for hydrocarbons for use in simulating the chemical vapor deposition of diamond films. *Physical review B*, 42(15):9458, 1990.

[11] Donald W Brenner, Olga A Shenderova, Judith A Harrison, Steven J Stuart, Boris Ni, and Susan B Sinnott. A second-generation reactive empirical bond order (rebo) potential energy expression for hydrocarbons. *Journal of Physics: Condensed Matter*, 14(4):783, 2002.

[12] DW Brenner, OA Shenderova, JA Harrison, SJ Stuart, B Ni, and SB Sinnott. A second-generation reactive empirical bond order (rebo) potential energy expression for hydrocarbons. *Journal of Physics: Condensed Matter*, 14(4):783, 2002.

[13] T Chang. Explicit solution of the radial breathing mode frequency of single-walled carbon nanotubes. *Acta Mechanica Sinica*, 23(2):159–162, 2007.

[14] T Chang and H Gao. Size-dependent elastic properties of a single-walled carbon nanotube via a molecular mechanics model. *Journal of the Mechanics and Physics of Solids*, 51(6):1059–1074, 2003.

[15] HC Cheng, YL Liu, CH Wu, and WH Chen. On radial breathing vibration of carbon nanotubes. *Computer Methods in Applied Mechanics and Engineering*, 199(45):2820–2827, 2010.

[16] Mildred S Dresselhaus, Gene Dresselhaus, PC Eklund, and AM Rao. Carbon nanotubes. In *The Physics of Fullerene-Based and Fullerene-Related Materials*, pages 331–379. Springer, 2000.

[17] WH Duan, CM Wang, and YY Zhang. Calibration of nonlocal scaling effect parameter for free vibration of carbon nanotubes by molecular dynamics. *Journal of applied physics*, 101(2):024305, 2007.

[18] A Cemal Eringen. On differential equations of nonlocal elasticity and solutions of screw dislocation and surface waves. *Journal of applied physics*, 54(9):4703–4710, 1983.

[19] A Cemal Eringen and DGB Edelen. On nonlocal elasticity. *International Journal of Engineering Science*, 10(3):233–248, 1972.

[20] Ricardo Faccio, Pablo A Denis, Helena Pardo, Cecilia Goyenola, and Alvaro W Mombrú. Mechanical properties of graphene nanoribbons. *Journal of Physics: Condensed Matter*, 21(28):285304, 2009.

[21] Michael R Falvo, GJ Clary, RM Taylor, V Chi, FP Brooks, S Washburn, and R Superfine. Bending and buckling of carbon nanotubes under large strain. *Nature*, 389(6651):582–584, 1997.

[22] R Fletcher and CM Reeves. Function minimization by conjugate gradients. *The Computer Journal*, 7(2):149–154, 1964.

[23] IW Frank, David M Tanenbaum, Arend M van der Zande, and Paul L McEuen. Mechanical properties of suspended graphene sheets. *Journal of Vacuum Science & Technology B: Microelectronics and Nanometer Structures Processing, Measurement, and Phenomena*, 25(6):2558–2561, 2007.

[24] Otakar Frank, Georgia Tsoukleri, John Parthenios, Konstantinos Papagelis, Ibtsam Riaz, Rashid Jalil, Kostya S Novoselov, and Costas Galiotis. Compression behavior of single-layer graphenes. *ACS nano*, 4(6):3131–3138, 2010.

[25] Junfeng Gao, Qinghong Yuan, Hong Hu, Jijun Zhao, and Feng Ding. Formation of carbon clusters in the initial stage of chemical vapor deposition graphene growth on ni (111) surface. *The Journal of Physical Chemistry C*, 115(36):17695–17703, 2011.

[26] Andre K Geim and Konstantin S Novoselov. The rise of graphene. *Nature Materials*, 6(3):183–191, 2007.

[27] E Ghavanloo, S Ahmad Fazelzadeh, and H Rafii-Tabar. Analysis of radial breathing-mode of nanostructures with various morphologies: a critical review. *International Materials Reviews*, pages 1743280415Y–0000000002, 2015.

[28] J Gong, L Thompson, and G Li. A semi-analytical approach for calculating the equilibrium structure and radial breathing mode frequency of single-walled carbon nanotubes. *Acta Mechanica Sinica*, 32(6):1075–1087, 2016.

[29] Yan-Gao Hu, Kim Meow Liew, Q Wang, XQ He, and BI Yakobson. Nonlocal shell model for elastic wave propagation in single-and double-walled carbon nanotubes. *Journal of the Mechanics and Physics of Solids*, 56(12):3475–3485, 2008.

[30] Pinshane Y Huang, Carlos S Ruiz-Vargas, Arend M van der Zande, William S Whitney, Mark P Levendorf, Joshua W Kevek, Shivank Garg, Jonathan S Alden, Caleb J Hustedt, Ye Zhu, et al. Grains and grain boundaries in single-layer graphene atomic patchwork quilts. *Nature*, 469(7330):389, 2011.

[31] Yonggang Huang, J Wu, and Keh-Chih Hwang. Thickness of graphene and single-wall carbon nanotubes. *Physical Review B*, 74(24):245413, 2006.

[32] Thomas JR Hughes. *The finite element method: linear static and dynamic finite element analysis*. Courier Corporation, 2012.

[33] TJR Hughes, A Masud, and I Harari. Numerical assessment of some membrane elements with drilling degrees of freedom. *Computers & structures*, 55(2):297–314, 1995.

[34] Sumio Iijima. Helical microtubules of graphitic carbon. *Nature*, 354(6348):56–58, 1991.

[35] H Jiang, P Zhang, B Liu, Y Huang, PH Geubelle, H Gao, and KC Hwang. The effect of nanotube radius on the constitutive model for carbon nanotubes. *Computational Materials Science*, 28(3):429–442, 2003.

[36] Jin-Wu Jiang, Jian-Sheng Wang, and Baowen Li. Youngs modulus of graphene: a molecular dynamics study. *Physical Review B*, 80(11):113405, 2009.

[37] J Kürti, G Kresse, and H Kuzmany. First-principles calculations of the radial breathing mode of single-wall carbon nanotubes. *Physical Review B*, 58(14):R8869, 1998.

[38] J Kürti, V Zólyomi, M Kertesz, and G Sun. The geometry and the radial breathing mode of carbon nanotubes: beyond the ideal behaviour. *New Journal of Physics*, 5(1):125, 2003.

[39] HM Lawler, D Areshkin, JW Mintmire, and CT White. Radial-breathing mode frequencies for single-walled carbon nanotubes of arbitrary chirality: First-principles calculations. *Physical Review B*, 72(23):233403, 2005.

[40] Changgu Lee, Xiaoding Wei, Jeffrey W Kysar, and James Hone. Measurement of the elastic properties and intrinsic strength of monolayer graphene. *Science*, 321(5887):385–388, 2008.

[41] Chengjian Li, Gang Li, and Huijuan Zhao. Hydrogenation induced deformation mode and thermal conductivity variations in graphene sheets. *Carbon*, 72:185–191, 2014.

[42] Chengjian Li, Gang Li, and Huijuan Zhao. Thermal conductivity variation of graphene with patterned double-side hydrogen doping. *Journal of Applied Physics*, 118(7):075102, 2015.

[43] Chunyu Li and Tsu-Wei Chou. A structural mechanics approach for the analysis of carbon nanotubes. *International Journal of Solids and Structures*, 40(10):2487–2499, 2003.

[44] W Li, J Chen, H Zhao, and G Li. Heat flux induced coherent vibration of h-shaped single layer graphene structure. *Nanoscale*, 10(3):1432–1439, 2018.

[45] KM Liew, Yang Zhang, and LW Zhang. Nonlocal elasticity theory for graphene modeling and simulation: prospects and challenges. *Journal of Modeling in Mechanics and Materials*, 1(1), 2017.

[46] Pin Lu, HP Lee, C Lu, and PQ Zhang. Application of nonlocal beam models for carbon nanotubes. *International Journal of Solids and Structures*, 44(16):5289–5300, 2007.

[47] Pin Lu, PQ Zhang, HP Lee, CM Wang, and JN Reddy. Non-local elastic plate theories. In *Proceedings of the Royal Society of London A: Mathematical, Physical and Engineering Sciences*, volume 463, pages 3225–3240. The Royal Society, 2007.

[48] IG Masters and KE Evans. Models for the elastic deformation of honeycombs. *Composite Structures*, 35(4):403–422, 1996.

[49] M Mohammadi, M Ghayour, and A Farajpour. Free transverse vibration analysis of circular and annular graphene sheets with various boundary conditions using the nonlocal continuum plate model. *Composites Part B: Engineering*, 45(1):32–42, 2013.

[50] Marcel Mohr, Konstantinos Papagelis, Janina Maultzsch, and Christian Thomsen. Two-dimensional electronic and vibrational band structure of uniaxially strained graphene from ab initio calculations. *Physical Review B*, 80(20):205410, 2009.

[51] Philip M Morse. Diatomic molecules according to the wave mechanics. ii. vibrational levels. *Physical Review*, 34(1):57, 1929.

[52] Kostya S Novoselov, Andre K Geim, Sergei V Morozov, D Jiang, Y_ Zhang, Sergey V Dubonos, Irina V Grigorieva, and Alexandr A Firsov. Electric field effect in atomically thin carbon films. *Science*, 306(5696):666–669, 2004.

[53] Gregory M Odegard, Thomas S Gates, Lee M Nicholson, and Kristopher E Wise. Equivalent-continuum modeling of nano-structured materials. *Composites Science and Technology*, 62(14):1869–1880, 2002.

[54] G Overney, W Zhong, and D Tomanek. Structural rigidity and low frequency vibrational modes of long carbon tubules. *Zeitschrift für Physik D Atoms, Molecules and Clusters*, 27(1):93–96, 1993.

[55] AJ Page, F Ding, S Irle, and K Morokuma. Insights into carbon nanotube and graphene formation mechanisms from molecular simulations: a review. *Reports on Progress in Physics*, 78(3):036501, 2015.

[56] Antonio Pantano, David M Parks, and Mary C Boyce. Mechanics of deformation of single-and multi-wall carbon nanotubes. *Journal of the Mechanics and Physics of Solids*, 52(4):789–821, 2004.

[57] QX Pei, YW Zhang, and VB Shenoy. A molecular dynamics study of the mechanical properties of hydrogen functionalized graphene. *Carbon*, 48(3):898–904, 2010.

[58] J Peng, J Wu, KC Hwang, J Song, and Y Huang. Can a single-wall carbon nanotube be modeled as a thin shell? *Journal of the Mechanics and Physics of Solids*, 56(6):2213–2224, 2008.

[59] Steve Plimpton. Fast parallel algorithms for short-range molecular dynamics. *Journal of computational physics*, 117(1):1–19, 1995.

[60] Philippe Poncharal, ZL Wang, Daniel Ugarte, and Walt A De Heer. Electrostatic deflections and electromechanical resonances of carbon nanotubes. *Science*, 283(5407):1513–1516, 1999.

[61] VN Popov. Curvature effects on the structural, electronic and optical properties of isolated single-walled carbon nanotubes within a symmetry-adapted non-orthogonal tight-binding model. *New Journal of Physics*, 6(1):17, 2004.

[62] VN Popov and P Lambin. Radius and chirality dependence of the radial breathing mode and the g-band phonon modes of single-walled carbon nanotubes. *Physical Review B*, 73(8):085407, 2006.

[63] MJD Powell. An efficient method for finding the minimum of a function of several variables without calculating derivatives. *The computer journal*, 7(2):155–162, 1964.

[64] SC Pradhan and JK Phadikar. Nonlocal elasticity theory for vibration of nanoplates. *Journal of Sound and Vibration*, 325(1):206–223, 2009.

[65] John E Proctor, Eugene Gregoryanz, Konstantin S Novoselov, Mustafa Lotya, Jonathan N Coleman, and Matthew P Halsall. High-pressure raman spectroscopy of graphene. *Physical Review B*, 80(7):073408, 2009.

[66] Dong Qian, Gregory J Wagner, Wing Kam Liu, Min-Feng Yu, and Rodney S Ruoff. Mechanics of carbon nanotubes. *Applied mechanics reviews*, 55(6):495–533, 2002.

[67] Junuthula Narasimha Reddy. *Mechanics of laminated composite plates and shells: theory and analysis*. CRC press, 2004.

[68] R Saito, G Dresselhaus, MS Dresselhaus, et al. *Physical properties of carbon nanotubes*, volume 4. World Scientific, 1998.

[69] R Saito, M Hofmann, G Dresselhaus, A Jorio, and MS Dresselhaus. Raman spectroscopy of graphene and carbon nanotubes. *Advances in Physics*, 60(3):413–550, 2011.

[70] D Sánchez-Portal, E Artacho, JM Soler, A Rubio, and P Ordejón. Ab initio structural, elastic, and vibrational properties of carbon nanotubes. *Physical Review B*, 59(19):12678, 1999.

[71] F Scarpa, S Adhikari, and A Srikantha Phani. Effective elastic mechanical properties of single layer graphene sheets. *Nanotechnology*, 20(6):065709, 2009.

[72] Junwei Sha, Rodrigo V Salvatierra, Pei Dong, Yilun Li, Seoung-Ki Lee, Tuo Wang, Chenhao Zhang, Jibo Zhang, Yongsung Ji, Pulickel M Ajayan, et al. Three-dimensional rebar graphene. *ACS applied materials & interfaces*, 9(8):7376–7384, 2017.

[73] A Shakouri, TY Ng, and RM Lin. A new rebo potential based atomistic structural model for graphene sheets. *Nanotechnology*, 22(29):295711, 2011.

[74] LE Shen, Hui-Shen Shen, and Chen-Li Zhang. Nonlocal plate model for nonlinear vibration of single layer graphene sheets in thermal environments. *Computational Materials Science*, 48(3):680–685, 2010.

[75] MM Shokrieh and R Rafiee. A review of the mechanical properties of isolated carbon nanotubes and carbon nanotube composites. *Mechanics of Composite Materials*, 46(2):155–172, 2010.

[76] FH Stillinger and TA Weber. Computer simulation of local order in condensed phases of silicon. *Physical Review B*, 31(8):5262, 1985.

[77] Z Tang, H Zhao, G Li, and NR Aluru. Finite-temperature quasicontinuum method for multiscale analysis of silicon nanostructures. *Physical Review B*, 74(6):064110, 2006.

[78] J Tersoff. Empirical interatomic potential for carbon, with applications to amorphous carbon. *Physical Review Letters*, 61(25):2879, 1988.

[79] Stephen P Timoshenko and Sergius Woinowsky-Krieger. *Theory of plates and shells*. McGraw-hill, 1959.

[80] MM JEBBESSEN Treacy, TW Ebbesen, and JM Gibson. Exceptionally high young's modulus observed for individual carbon nanotubes. *Nature*, 381(6584):678–680, 1996.

[81] Georgia Tsoukleri, John Parthenios, Konstantinos Papagelis, Rashid Jalil, Andrea C Ferrari, Andre K Geim, Kostya S Novoselov, and Costas Galiotis. Subjecting a graphene monolayer to tension and compression. *Small*, 5(21):2397–2402, 2009.

[82] Laetitia Vaccarini, Christophe Goze, Luc Henrard, E Hernandez, Patrick Bernier, and Angel Rubio. Mechanical and electronic properties of carbon and boron–nitride nanotubes. *Carbon*, 38(11):1681–1690, 2000.

[83] Gregory Van Lier, Christian Van Alsenoy, Vic Van Doren, and Paul Geerlings. Ab initio study of the elastic properties of single-walled carbon nanotubes and graphene. *Chemical Physics Letters*, 326(1-2):181–185, 2000.

[84] Lifeng Wang and Haiyan Hu. Flexural wave propagation in single-walled carbon nanotubes. *Physical Review B*, 71(19):195412, 2005.

[85] Lifeng Wang, Haiyan Hu, and Wanlin Guo. Validation of the non-local elastic shell model for studying longitudinal waves in single-walled carbon nanotubes. *Nanotechnology*, 17(5):1408, 2006.

[86] Lifeng Wang, Quanshui Zheng, Jefferson Z Liu, and Qing Jiang. Size dependence of the thin-shell model for carbon nanotubes. *Physical Review Letters*, 95(10):105501, 2005.

[87] Q Wang. Effective in-plane stiffness and bending rigidity of armchair and zigzag carbon nanotubes. *International Journal of Solids and Structures*, 41(20):5451–5461, 2004.

[88] Q Wang. Wave propagation in carbon nanotubes via nonlocal continuum mechanics. *Journal of Applied physics*, 98(12):124301, 2005.

[89] Q Wang and VK Varadan. Application of nonlocal elastic shell theory in wave propagation analysis of carbon nanotubes. *Smart Materials and Structures*, 16(1):178, 2007.

[90] Q Wang and CM Wang. The constitutive relation and small scale parameter of nonlocal continuum mechanics for modelling carbon nanotubes. *Nanotechnology*, 18(7):075702, 2007.

[91] Eric W Wong, Paul E Sheehan, and Charles M Lieber. Nanobeam mechanics: elasticity, strength, and toughness of nanorods and nanotubes. *Science*, 277(5334):1971–1975, 1997.

[92] J Wu, KC Hwang, and Y Huang. An atomistic-based finite-deformation shell theory for single-wall carbon nanotubes. *Journal of the Mechanics and Physics of Solids*, 56(1):279–292, 2008.

[93] Y Xiao, ZM Li, XH Yan, Y Zhang, YL Mao, and YR Yang. Curvature effect on the radial breathing modes of single-walled carbon nanotubes. *Physical Review B*, 71(23):233405, 2005.

[94] Boris I Yakobson, CJ Brabec, and J Bernholc. Nanomechanics of carbon tubes: instabilities beyond linear response. *Physical Review Letters*, 76(14):2511, 1996.

[95] B Yang and Vinod K Tewary. Multiscale greens function for the deflection of graphene lattice. *Physical Review B*, 77(24):245442, 2008.

[96] Min-Feng Yu, Bradley S Files, Sivaram Arepalli, and Rodney S Ruoff. Tensile loading of ropes of single wall carbon nanotubes and their mechanical properties. *Physical Review Letters*, 84(24):5552, 2000.

[97] Min-Feng Yu, Oleg Lourie, Mark J Dyer, Katerina Moloni, Thomas F Kelly, and Rodney S Ruoff. Strength and breaking mechanism of multiwalled carbon nanotubes under tensile load. *Science*, 287(5453):637–640, 2000.

[98] Y Yu, H Zhao, and G Li. A quasi-continuum thermomechanical model for phonon damping analysis of single crystal silicon nano-resonators. *International Journal of Heat and Mass Transfer*, 106:491–502, 2017.

[99] YQ Zhang, GR Liu, and JS Wang. Small-scale effects on buckling of multiwalled carbon nanotubes under axial compression. *Physical review B*, 70(20):205430, 2004.

[100] J Zimmermann, P Pavone, and G Cuniberti. Vibrational modes and low-temperature thermal properties of graphene and carbon nanotubes: Minimal force-constant model. *Physical Review B*, 78(4):045410, 2008.